Observing and Quantifying Kinematic Properties and Lagrangian Coherent Structures of Ocean Flows using Drifter Experiments

By

Timothy Getscher

B.S., United States Naval Academy, 2019

Submitted to the Department of Earth, Atmospheric, and Planetary Sciences in partial fulfillment of the requirements for the degree of

Master of Science

at the

MASSACHUSETTS INSTITUTE OF TECHNOLOGY

and the

WOODS HOLE OCEANOGRPAHIC INSTITUTION

September 2021

Author .....

Joint Program in Oceanography
Massachusetts Institute of Technology
and Woods Hole Oceanographic Institution
August 31, 2021

Certified by .....

Irina Rypina
Associate Scientist
Woods Hole Oceanographic Institution
Thesis Supervisor

Accepted by .....

Glenn Flierl
Chair, Joint Committee for Physical Oceanography
Massachusetts Institute of Technology
and Woods Hole Oceanographic Institution

Observing and Quantifying Kinematic Properties and Lagrangian Coherent Structures of Ocean Flows using Drifter Experiments

by

Timothy Getscher

Submitted to the Department of Earth, Atmospheric, and Planetary Sciences
on August 31, 2021, in partial fulfillment of the
requirements for the degree of
Master of Science

Abstract

This thesis analyzes data from two types of unique drifter experiments in order to characterize two aspects of ocean flows that are often difficult to study. First, vertical velocities and their associated transport processes are often challenging to observe in the real ocean since vertical velocities are typically orders of magnitude smaller than horizontal velocities in mesoscale and submesoscale flows. Second, Lagrangian coherent structures (LCS) are features which categorize ocean flows into regimes of distinct behavior. These structures are also difficult to quantify in the real ocean, since sets of gridded trajectories from real ocean data (rather than model fields) are rarely available.

The first experiment uses drifters drogued at multiple depths in the Alboran Sea to observe and characterize the ocean's vertical structure, particularly near a strong front where vertical velocities are expected to be much stronger than other regions of the Ocean. The second experiment uses a roughly gridded pattern of surface drifters in the Gulf of Mexico to study LCSs as quantified by methods from dynamical systems such as finite-time Lyapunov exponents (FTLEs), trajectory arc-length, correlation dimension, dilation, Lagrangian-averaged vorticity deviation (LAVD), and spectral clustering. This thesis includes the first attempt to apply these dynamical systems techniques to real drifters for LCS detection.

Overall, these experiments and the methods used in this paper are shown to be promising new techniques for quantifying both the vertical structure of ocean flows and Lagrangian Coherent Structures of flows using real drifter data. Future work may involve modified versions of the experiments, with denser sets of ocean drifters in the horizontal and/or vertical directions.

Thesis Supervisor: Dr. Irina Rypina
Title: Associate Scientist
Woods Hole Oceanographic Institution

Acknowledgments

I am first and foremost grateful to my adviser, Irina Rypina, for all of her wisdom, rigor, and insight that have shaped this thesis. She helped me to think in new ways and guided me through these formative years in science and research. The MIT/WHOI Joint Program has been my introduction to the geophysical sciences, and Irina's trust and patience allowed me to learn effectively and stay focused in the process. I am also thankful to Larry Pratt, whose wisdom and expertise guided me throughout this thesis.

Thank you to Baptiste Mourre, who went to great lengths to provide our team with model fields. He was always prompt and thorough, even with our more obscure requests, and his help was essential to Chapter 1.

Thanks to Margaux Filippi for the guidance she offered on the topic of spectral clustering. Code designed by her and Alireza Hadjighasem helped clarify and inspire my own methods, so I am thankful to them both. This topic was particularly difficult to grasp, and became an important addition to Chapter 2.

Thank you to Tamay Ozgokmen, who provided us with data from the SPLASH experiment which became the foundation of Chapter 2. This unique dataset proved to be an excellent framework for the dynamical systems techniques applied in this thesis.

I am also incredibly grateful for the friends I've made in the Joint Program at MIT and WHOI. I was blessed with a cohort of enthusiastic and supportive classmates who have made me feel at home during these strange times. I will miss our late nights of work, games, and discussions.

Thank you to my undergraduate mentors Kevin McIlhany, Steve Wiggins, and Reza Malek-Madani. Though my work with them has long been complete, their continued support and interest has motivated me throughout my time with the Joint Program. They inspired my own interest in dynamical systems, and led me on a path to attend MIT and WHOI.

I am also thankful to my friends and family back home and in the Navy. Their love, kindness, and intellect has shaped me both as a person and researcher.

My Masters studies in the MIT/WHOI Joint Program were funded by the US Navy Civilian Institution Office.

Contents

1 Observing and Quantifying Vertical and Horizontal Ocean Flow Properties using Drifters Drogued at Different Depths 17

1.1 Introduction . . . 17

1.2 Methods . . . 18

1.2.1 Multi-layer drifter deployment . . . 18

1.2.2 Ancillary Datasets . . . 19

1.2.3 Estimation of velocity gradient, divergence and vorticity . . . 19

1.2.4 Estimation of vertical velocity . . . 22

1.2.5 Estimation of the aspect ratio of the drifter polygon . . . 23

1.2.6 Estimation of finite-time Lyapunov exponents . . . 24

1.2.7 Investigating the vertical vorticity balance following drifter trajectories 27

1.2.8 Investigating the evolution of horizontal divergence following trajectories . . . 27

1.2.9 Bootstrapping uncertainty analysis of divergence and vorticity . . . 28

1.2.10 Uncertainty in divergence and vorticity due to the GPS positioning errors . . . 28

1.2.11 Ekman analysis of real drifters using bulk flux algorithms . . . 30

1.2.12 High-resolution ocean circulation model and analysis of simulated drifters 32

1.3 Results . . . 34

1.3.1 Analysis of Real Drifters . . . 34

1.3.2 Analysis of Simulated Drifters . . . 41

1.3.3 Analysis of the concurrent u-CTD and ADCP measurements . . . 47

1.4 Discussion . . . 51

2 Applying Dynamical Systems Techniques to Real Drifters 55

2.1 Introduction . . . 55

2.2 Methods . . . 56

2.2.1 Finite-time Lyapunov Exponents . . . 56

2.2.2 Arc-Length . . . 57

2.2.3 Trajectory Complexity (Correlation Dimension) 58
2.2.4 Encounter Number 58
2.2.5 Vorticity and Divergence 59
2.2.6 Dilation 59
2.2.7 Lagrangian-Averaged Vorticity Deviation 60
2.2.8 Spectral Clustering of Trajectories 61
2.2.9 NCOM Forecasts during SPLASH 63
2.3 Analysis of Real Drifter Results 65
2.3.1 Finite-time Lyapunov Exponents 65
2.3.2 Trajectory Arc-Length 66
2.3.3 Trajectory Complexity (Correlation Dimension) 67
2.3.4 Encounter Number 68
2.3.5 Divergence and Vorticity 69
2.3.6 Dilation 72
2.3.7 Lagrangian-Averaged Vorticity Deviation 73
2.3.8 Spectral Clustering of Trajectories 75
2.4 Analysis of Simulated Drifter Results 76
2.4.1 Finite-time Lyapunov Exponents 76
2.4.2 Trajectory Arc-Length 78
2.4.3 Trajectory Complexity (Correlation Dimension) 80
2.4.4 Encounter Number 81
2.4.5 Divergence and Vorticity 83
2.4.6 Dilation 86
2.4.7 Lagrangian-Averaged Vorticity Deviation 88
2.4.8 Spectral Clustering of Trajectories 89
2.5 Discussion 91

List of Figures

1-1 Trajectories of drifters, color-coded by drogue depth. 25-hour trajectory segments are encompassed by the black box. Solid black area represents land. The left inset shows a zoomed-in view of the 25-hour trajectory segments. The right inset shows deployment station locations (asterisks) and drifter locations at the time when the last drifter was released (squares). 34

1-2 Drifter-based estimates of (a) separation between the center of mass of the drifter distribution at 1 m and at 50 m), (c) area of the polygon formed by the drifters, (e) aspect ratio of the polygon, (b) divergence, (d) vorticity, and (f) vertical velocity at 4 depths. In panels b and d colored stripes show the ± 1 standard deviation interval from bootstrapping method. The dashed black line shows ± 1 standard deviation estimates due to GPS uncertainty, and the solid black line shows the value of f. Color notation is the same as in Figure 1-1. 36

1-3 Drifter-based divergence (a,c,e,g) and vorticity (b,d,f,h) estimated using different methods at 1 m (a,b), 10 m (c,d), 30 m (e,f), and 50 m (g,h). Color notation is the same as in Figure 1-1. 37

1-4 The relationship between estimated terms in the (a) horizontal divergence balance equation, and (b) vertical vorticity balance equation. Correlation coefficients are shown at the top left corner of each subplot. Color notation is the same as in Figure 1-1. 38

1-5 Estimates of 3D and 2D FTLEs at 4 depths using drifter-based measurements. 3D FTLEs were computed using the ellipsoid fit method. 2D FTLEs were computed using the unstructured grid method. Dashed curve shows the FTLE induced by the vertical shear of horizontal velocity. 39

1-6 Drifter trajectories up to 2.5 days, with winds shown as grey arrows. Winds between days 2 through 4 are predominantly southwesterly. 40

1-7 Panel (a): Ekman currents shown at one hour intervals over three days. The colored lines represent the center of mass of all drifters in each layer. Colored arrows represent the direction and relative magnitude of Ekman currents. The displacement between the 1 m layer and the bottom layers is around 10-15 km after three days. Panel (b): Accumulated Ekman displacement over three days. Estimated zonal displacement due to Ekman currents for the 1 m layer is 6 km Eastward. 40

1-8 Simulated drifter trajectories from the SOCIB WMOP model. Trajectory segments outside of the 400-m-resolution model domain (dashed box) and/or past 48 hours after deployment were computed using the 2-km-resolution model velocities. The solid black box encircles the 25-hour-long trajectory segments, which are also shown in the small inset. 41

1-9 Panel (a) shows Ekman currents at the center of mass of the drifter distribution at each level every 5 min for 5 days, and the cumulative Ekman displacements after 5 days. Panel (c) shows simulated trajectories advected by the model currents with the Ekman velocity fields removed. 41

1-10 Same content as Figure 2 but for the simulated drifter release in SOCIB WMOP 42

1-11 Eulerian model divergence and vorticity (solid) and simulated-drifter-based Lagrangian divergence (a-d) and vorticity (e-h) estimated using different methods (as indicated by the legend) at 1 m (a,e), 10 m (b,f), 30 m (c,g), and 50 m (d,h). 44

1-12 At 4 depths, comparison between the Eulerian model vertical velocity (solid) and vertical velocity estimated using drifter based methods according to the legend. “4 layers, laterally separated” and “4 layers, vertically stacked” refer to simulation where model divergence at 4 depths was used at the geographical locations corresponding to the center of mass of the 6 drifters at 4 depths, or at the same geographical location, respectively. 45

1-13 Same content as shown in Figure 1-4 but for simulated drifters released in SOCIB WMOP. 46

1-14 Same content as shown in Figure 1-5 but for simulated drifters released in SOCIB WMOP. 47

1-15 Satellite-based SSH contours (grey curves) and geostrophic currents (arrows), with the ship-based sections (thick grey and black lines) and multi-level drifter trajectories (colored curves) superimposed. The 6 sections that were used for our analysis are shown in black and are numbered 1 through 6, with the section number indicated next to the section. The grey sections located between sections 1 and 2, 2 and 3, 3 and 4, and 4 and 5 were qualitatively similar to their neighboring black sections and were omitted for brevity. 47

1-16 Drifter based estimates of vorticity at all depths, color coded such as in Figure 1-1. Grey shaded regions correspond to the time interval when each section was taken (section s are labeled at the bottom of the graph) and colored dots correspond to the times the center of mass of drifters in each layer passed the section. 49

1-17 Density for section 1, computed using (a) CTD data for both temperature and salinity, (b) temperature but with fixed salinity, and (c) salinity but with fixed temperature. 49

1-18 For sections 1 (bottom) through 6 (top), profiles of density (left) and zonal (middle) and meridional (right) currents. All sections (black rectangles) are superimposed on section 1. Red curves in the left panels correspond to sections 2 through 6 as labeled above each panel. Drifters are shown by circles, color-coded by zonal or meridional velocity, corresponding to the panel they are in. 50

1-19 Error analysis for testing of the LLS method of estimating gradients, for a simulation involving two arrays of 3 stations. The top left and top middle panels correspond to the LLS method that does not include time (so all measurements are considered to be taken instantaneously). The bottom three panels correspond to the LLS method including time such as in Equation 1.6. The red box corresponds to the regime in which the vessel from the CALYPSO experiment operates, with sampling intervals of about 2 minutes and 400 meters (represented by the bottom and left edges of the square), and with sections being measured at roughly 1 hour and 5 km apart (represented by right and top edges of the square). The top right panel shows velocity fields from the 400 m SOCIB WMOP model, with one example of the simulation layout. . . 51

2-1 Locations of FTLE estimates for real drifters. Panel (a) contains only drifter locations as black dots, with grey edges representing the connections between neighboring trajectories used in the unstructured grid FTLE method. These edges are determined by the Delaunay triangulation algorithm, and all edges are used in the computation. Panel (b) shows drifter locations again as black dots, but also shows grey dots representing the centers of FTLE estimates, for which connected drifters define axes in the computation. These edges were chosen manually. 57

2-2 Spaghetti plots of trajectories from real drifters (left panel), trajectories from simulated drifters released at the same times and locations of real drifters (middle panel), and trajectories from simulated drifters released at the new chosen location (right panel). Trajectories are shown as black slightly transparent lines. 64

2-3 Forward FTLE snapshot at the release time of real drifters. The black box in the northern part of the domain represents the start location of real drifters. The blue box represents the chosen start location of simulated drifters. FTLE ridges are associated with stable manifolds, and ridges inside and surrounding the blue box align roughly with the backward-advected final locations of Figure 2-2. 64

2-4 FTLE estimates for real drifters with $\tau = 0.5$. The left panel shows estimates as a function of initial position. Results in the middle and right panels are shown as a function of current position at the integration time. 65

2-5 Same as Figure 2-4 except for $\tau = 1$ days. 66

2-6 Same as Figure 2-4 except for $\tau = 3$ days. 66

2-7 Arc-length estimates for real drifters with $\tau = 0.5$. The left panel shows estimates as a function of initial position. Results in the middle and right panels are shown as a function of current position at the integration time. . . 67

2-8 Same as Figure 2-7 except for $\tau = 1$ days. 67

2-9 Same as Figure 2-7 except for $\tau = 3$ days. 67

2-10 Correlation dimension estimates for real drifters with $\tau = 0.5$. The left panel shows estimates as a function of initial position. Results in the middle and right panels are shown as a function of current position at the integration time. 68

2-11 Same as Figure 2-10 except for $\tau = 1$ days. 68

2-12 Same as Figure 2-10 except for $\tau = 3$ days. 68

2-13 Encounter number estimates for real drifters with $\tau = 0.5$. The left panel shows estimates as a function of initial position. Results in the middle and right panels are shown as a function of current position at the integration time. 69
2-14 Same as Figure 2-13 except for $t = 1$ days. 69
2-15 Same as Figure 2-13 except for $t = 3$ days. 69
2-16 Divergence estimates for real drifters at $t = 0.5$. The left panel shows estimates as a function of initial position. Results in the middle and right panels are shown as a function of current position at the integration time. 71
2-17 Vorticity estimates for real drifters at $t = 0.5$. The left panel shows estimates as a function of initial position. Results in the middle and right panels are shown as a function of current position at the integration time. 71
2-18 Same as Figure 2-16 except for $t = 1$ days. 71
2-19 Same as Figure 2-17 except for $t = 1$ days. 71
2-20 Same as Figure 2-16 except for $t = 3$ days. 72
2-21 Same as Figure 2-17 except for $t = 3$ days. 72
2-22 Dilation estimates for real drifters with $\tau = 0.5$. The left panel shows estimates as a function of initial position. Results in the middle and right panels are shown as a function of current position at the integration time. 73
2-23 Same as Figure 2-22 except for $\tau = 1$ days. 73
2-24 Same as Figure 2-22 except for $\tau = 3$ days. 73
2-25 LAVD estimates for real drifters with $\tau = 0.5$. The left panel shows estimates as a function of initial position. Results in the middle and right panels are shown as a function of current position at the integration time. 74
2-26 Same as Figure 2-25 except for $\tau = 1$ days. 74
2-27 Same as Figure 2-25 except for $\tau = 3$ days. 74
2-28 Spectral clusters for real drifters with $\tau = 0.5$. The left panel shows estimates as a function of initial position. Results in the middle and right panels are shown as a function of current position at the integration time. 75
2-29 Same as Figure 2-28 except for $\tau = 1$ days. 75
2-30 Same as Figure 2-28 except for $\tau = 3$ days. 75
2-31 FTLE fields for results from simulated drifters (top row) and from a grid with spacing of .001 degrees (bottom row) with integration time $\tau = 0.5$. Results in the left column (top left and bottom left) are shown as a function of initial position. Results in the middle and right columns are shown as a function of current position at the integration time. 77
2-32 Same as Figure 2-31 except for $t = 2$ days. 77

2-33 Same as Figure 2-31 except for $t = 4$ days. 78

2-34 Arc-length fields for results from simulated drifters (top row) and from a grid with spacing of .001 degrees (bottom row) with integration time $\tau = 0.5$. Results in the left column (top left and bottom left) are shown as a function of initial position. Results in the middle and right columns are shown as a function of current position at the integration time. 78

2-35 Same as Figure 2-34 except for $\tau = 2$ days. 79

2-36 Same as Figure 2-34 except for $\tau = 4$ days. 79

2-37 Correlation Dimension field for results from simulated drifters (top row) and from a grid with spacing of .004 degrees (bottom row) with integration time $\tau = 0.5$. Results in the left column (top left and bottom left) are shown as a function of initial position. Results in the middle and right columns are shown as a function of current position at the integration time. 80

2-38 Same as Figure 2-37 except for $\tau = 2$ days. 81

2-39 Same as Figure 2-37 except for $\tau = 4$ days. 81

2-40 Encounter number and volume fields for results from simulated drifters (top row) and from a grid with spacing of .001 degrees (bottom row) with integration time $\tau = 0.5$. Results in the left column (top left and bottom left) are shown as a function of initial position. Results in the middle and right columns are shown as a function of current position at the integration time. . 82

2-41 Same as Figure 2-40 except for $\tau = 1.5$ days. 82

2-42 Same as Figure 2-40 except for $\tau = 4$ days. 83

2-43 Divergence field for results from simulated drifters (top row) and from a grid with spacing of .001 degrees (bottom row) at time $t = 0.5$. Results in the left column (top left and bottom left) are shown as a function of initial position. Results in the middle and right columns are shown as a function of current position at the integration time. 83

2-44 Vorticity field for results from simulated drifters (top row) and from a grid with spacing of .001 degrees (bottom row) at time $t = 0.5$. Results in the left column (top left and bottom left) are shown as a function of initial position. Results in the middle and right columns are shown as a function of current position at the integration time. 84

2-45 Same as Figure 2-43 except for $t = 2$ days. 84

2-46 Same as Figure 2-44 except for $t = 2$ days. 85

2-47 Same as Figure 2-43 except for $t = 4$ days. 85

2-48 Same as Figure 2-44 except for $t = 4$ days. 86

2-49 Dilation field for results from simulated drifters (top row) and from a grid with spacing of .001 degrees (bottom row) with integration time $\tau = 0.5$. Results in the left column (top left and bottom left) are shown as a function of initial position. Results in the middle and right columns are shown as a function of current position at the integration time. 86
2-50 Same as Figure 2-49 except for $\tau = 2$ days. 87
2-51 Same as Figure 2-49 except for $\tau = 4$ days. 87
2-52 LAVD field for results from simulated drifters (top row) and from a grid with spacing of .001 degrees (bottom row) with integration time $\tau = 0.5$. The dense grid has now been confined to a diamond-shape, encompassing the domain formed by simulated drifters. Results in the left column (top left and bottom left) are shown as a function of initial position. Results in the middle and right columns are shown as a function of current position at the integration time. 88
2-53 Same as Figure 2-52 except for $\tau = 2$ days. 88
2-54 Same as Figure 2-52 except for $\tau = 4$ days. 89
2-55 Spectral clusters field for results from simulated drifters. Left panel results are shown as a function of initial position. Results in the middle and right panels are shown as a function of current position at the integration time. . . 90
2-56 Same as Figure 2-55 except for $\tau = 2$ days, with $r = 18.5$ km. 90
2-57 Same as Figure 2-55 except for $\tau = 2$ days, with $r = 15.3$ km. 90
2-58 Same as Figure 2-55 except for $\tau = 4$ days, with $r = 5.5$ km. 90
2-59 Same as Figure 2-55 except for $\tau = 4$ days, with $r = 9.3$ km. 91
2-60 Same as Figure 2-55 except for $\tau = 4$ days, with $r = 19$ km. 91

Chapter 1

Observing and Quantifying Vertical and Horizontal Ocean Flow Properties using Drifters Drogued at Different Depths

1.1 Introduction

Traditional Lagrangian surface drifters are one of the oldest tools in physical oceanography, but they can only provide information about near-surface currents. This chapter analyzes data from a multi-layer drifter experiment, which is unique in its ability to describe the vertical structure of ocean flows using Lagrangian data. The multi-depth experiment and methods shown in this chapter prove to be a promising strategy for studying both horizontal and vertical processes throughout the upper part of the water column.

This chapter specifically focuses on an experiment in the Alboran Sea during a spring 2018 field experiment as part of the CALYPSO project (https://calypsodri.whoi.edu/). The experiment targeted the Almería-Oran front, which extends roughly between Almería, Spain and Oran, Algeria. Vertical processes near such fronts are expected to be more significant than other regions of the ocean, making this region a promising arena to test the methods in this thesis.

The experiment involved releasing 24 drifters – 6 drifters each drogued at depths 1 m, 10 m, 30 m, and 50 m. These drifters were released in roughly circular clusters that were vertically aligned, to allow for stacking of layers to create a three-dimensional array. The first 25 hours of the experiment were analyzed, during a period of time when drifter layers were still roughly aligned vertically (within 10 km) and while drifters within layers still formed relatively small polygons. Divergence, vorticity, and vertical velocity were estimated using

position data from the drifter arrays.

Finite-time Lyapunov exponents (FTLEs), a common method from dynamical systems, were also computed in this chapter using real drifter trajectories. FTLEs are rarely computed for drifter arrays, and this particular multi-layer experiment allows for the computation of both 2D and 3D FTLEs in the real ocean. This chapter introduces a somewhat novel framework for estimating 2D and 3D FTLEs in the context of a multi-layer drifter experiment.

1.2 Methods

1.2.1 Multi-layer drifter deployment

A multi-layer array of 24 drifters, with six drifters drogued at depths of 1, 10, 30 and 50 m was deployed on May 29, 2018. The drifters at 1 m were of the CODE design originally developed by Dr. Russ Davis of SIO. The same design of drifters was used by Rypina et al. (2014), Rypina et al. (2016) and Chen et al. (2014), and are in use by the U.S. Coast Guard for search and rescue operations. Drifters at lower depths were of the holey-sock design, similar to the standard SVP drifters (https://www.aoml.noaa.gov/phod/gdp/) but with a custom-length cable between the surface buoy and the subsurface holey-sock drogue. Drifters were equipped with SPOT Trace GPS tracker, which transmitted geographical positions at 5 min intervals for about 10 days (the same SPOT Trace trackers are used in CARTHE drifters, see D'Asaro et al. (2020)).

The drifters were released about 1 day upstream of the Almería-Oran front, along the western edge of the Eastern Alboran Gyre. The actual release location was determined in real time based on available density and velocity data from undulating CTD (u-CTD) and ADCP measurements as well as glider measurements from the same cruise. Drifters were released at each of the four depths at six stations (2 rows of 3 stations), with neighboring stations being 1-2 km apart from each other (stations shown in Figure 1-1). The deployment was completed within about 2 hours. The methods used for estimating velocity gradients (and subsequently divergence and vorticity) work best when drifters remain close together and form a near "circle." To compensate for unwanted drifter advection between drifter releases, a "dynamic deployment" strategy was used in which velocity data from ADCP measurements was used to project drifter locations forward in time. This strategy resulted in a tight, approximately 2 km by 2 km cluster of drifters by the time the final drifter was released.

1.2.2 Ancillary Datasets

Two additional ancillary datasets were used to put drifter-based observations into context. Specifically, satellite-based sea surface height (SSH) data and its corresponding geostrophic velocities, as well as in-situ CTD and ADCP measurements along several sections during the time of the cruise. The SSH data and geostrophic velocities are level-4 gridded maps available publicly on the Copernicus Marine Service website (https://resources.marine.copernicus.eu/?option=com_csw&view=details&product_id=SEALEVEL_MED_PHY_CLIMATE_L4_REP_OBSERVATIONS_008_056). CTD data came from the u-CTD module towed by the drifter deployment vessel during the cruise, and ADCP data similarly came from the ship-mounted ADCP instrument on the same vessel.

1.2.3 Estimation of velocity gradient, divergence and vorticity

In order to compute estimated divergence and vorticity from drifters, horizontal velocities were first computed using a centered finite-difference scheme. Then, the linear least-squares (LLS) method of Molinari and Kirwan (1975) was applied to estimate horizontal velocity gradients from drifter velocities and positions. The accuracy of this method is affected by the number of drifters, distance between drifters, and the geometry of the polygon formed by the drifters. The method works best in tight equidistant clusters of many drifters, and it deteriorates with less drifters or "stretched" clusters (quantified by the aspect ratio, i.e. the ratio of longest to shortest dimension of the drifter polygon). This method was tested as part of the PhD thesis of Sebastian Essink (Essink, 2019) using a 500 m resolution numerical model of a baroclinically unstable front. Essink showed reasonable agreement ($R^2 > 0.6$) between estimated and true model vorticity for clusters of 6 simulated drifters, with separation of about 3 km, and with polygon aspect ratio of < 10. In this chapter, the geometric configuration of drifters is characterized by the area of the polygon formed by the drifters, and the aspect ratio of the drifter distribution.

The method itself is based off of the Taylor expansion of velocity fields around a point in space . The x-component of velocity u_i at point (x_i, y_i) near $\bar{x}$ can be written as

$$u_i = \bar{u} + \frac{\partial u}{\partial x}(x_i - \bar{x}) + \frac{\partial u}{\partial y}(y_i - \bar{y}) \ , \tag{1.1}$$

which can be included in a system of linear differential equations for $i = 1, 2, \ldots N$ points,

$$\begin{bmatrix} u_1 \\ u_2 \\ \vdots \\ u_n \end{bmatrix} = \begin{bmatrix} 1 & (x_1 - \bar{x}) & (y_1 - \bar{y}) \\ 1 & (x_2 - \bar{x}) & (y_2 - \bar{y}) \\ \vdots & \vdots & \vdots \\ 1 & (x_N - \bar{x}) & (y_N - \bar{y}) \end{bmatrix} \begin{bmatrix} \bar{u} \\ \frac{\partial u}{\partial x} \\ \frac{\partial u}{\partial y} \end{bmatrix} , \tag{1.2}$$

where we will call the vector on the LHS U, the matrix on the RHS R, and the vector on the RHS A, such that:

$$U = RA \ . \tag{1.3}$$

Since the matrix R does not necessarily have an inverse (provided that it is not square), then the least squares method is used to estimate A as

$$\begin{aligned} A &= (R^T R)^{-1} R^T U \\ &= \begin{bmatrix} \bar{u} & \frac{\partial u}{\partial x} & \frac{\partial u}{\partial y} \end{bmatrix}^T \ . \end{aligned} \tag{1.4}$$

Thus, the second and third components of the vector A are LLS approximations of the horizontal derivatives of u. Similarly, the same operation can be done for a matrix V containing the y-components of velocity,

$$\begin{aligned} B &= (R^T R)^{-1} R^T V \\ &= \begin{bmatrix} \bar{b} & \frac{\partial v}{\partial x} & \frac{\partial v}{\partial y} \end{bmatrix}^T \ , \end{aligned} \tag{1.5}$$

and then all four horizontal derivatives of u and v are known and can be summed to form divergence and vorticity.

One modification of this algorithm could involve time-derivatives as well, by simply including a temporal derivative term in the Taylor expansion,

$$u_i = \bar{u} + \frac{\partial u}{\partial x}(x_i - \bar{x}) + \frac{\partial u}{\partial y}(y_i - \bar{y}) + \frac{\partial u}{\partial t}(t_i - \bar{t}) \ , \tag{1.6}$$

in which measurements u_i are taken at varying times as well as positions. This introduces a

fourth column to the matrix R and a fourth element, $\frac{\partial u}{\partial x}$ to the least-squares estimate vector A or B. While the method including time seems impractical for drifter data whose locations change dramatically over time, it was hypothesized that it could be used for ADCP data, for which multiple measurements are taken near a central location over various times. Testing of this method is included in section 1.3.3.

Another method for estimating horizontal divergence is related to the change in area of the drifter polygon, written as

$$\nabla_H \cdot \vec{u} = \frac{1}{A}\frac{dA}{dt} \ . \tag{1.7}$$

This area method is a standard technique and is described in many classic oceanographic and meteorological texts, such as Holton and Hakim (2013), Dutton (2002), or Pedlosky (1987).

Also, both the area-averaged vertical vorticity and area-averaged divergence of drifter clusters can be estimated by applying Green's theorem. This involves evaluating the circulation around the drifter polygon (for vorticity) and the total flux out of the drifter polygon (for divergence). The relevant formulas are

$$\int\int_A (\nabla \times \vec{u}) \cdot \hat{z} da = \oint \vec{u} \cdot d\vec{s} \ , \tag{1.8}$$

and

$$\int\int_A (\nabla_H \cdot \vec{u}) \, da = \oint \vec{u} \cdot \hat{n} d\vec{s} \ , \tag{1.9}$$

where A is the area of the drifter polygon, and $d\vec{s}$ and $\hat{n}ds$ are unit vectors that are tangential and normal to the polygon, respectively, and the integrals on the right sides are taken all the way around the polygon. For area-averaged vorticity and divergence, $\nabla_H \cdot \vec{u}$ and $(\nabla \times \vec{u}) \cdot \hat{z}$ can be taken out of the integral as a constant, and then $\int\int_A da$ can be replaced by A. The vorticity and divergence can then be written as:

$$(\nabla \times \vec{u}) \cdot \hat{z} = \frac{1}{A} \oint \vec{u} \cdot d\vec{s} \ , \tag{1.10}$$

and

$$(\nabla_H \cdot \vec{u}) = \frac{1}{A} \oint \vec{u} \cdot \hat{n} d\vec{s} \,, \tag{1.11}$$

respectively.

1.2.4 Estimation of vertical velocity

Vertical velocity can be estimated by integrating the continuity equation, $\frac{\partial u}{\partial x} + \frac{\partial v}{\partial y} = -\frac{\partial w}{\partial z}$ downwards from the surface ($z = 0$) to some depth z ($z < 0$), which gives $w(z) = w(0) - \int_z^0 dz(\frac{du}{dx} + \frac{dv}{dy})$. For our computations we assume that $w(0) = 0$.

Vertical velocity at the sea surface are mainly due to tides and surface gravity waves. The strongest tidal component in the Alboran Sea is M_2, with an amplitude of $\sim$20 cm near the Eastern Alboran gyre (Alberola et al., 1995). The resulting tidally-induced vertical velocities are approximately 10^{-5} m/s, which is one to two orders of magnitude smaller than our drifter-based estimated vertical velocities at 10 m and below. Surface gravity waves act on small spatial and temporal scales, so they are unlikely to have strong affects on the scales of $\mathcal{O}$(1 km) and $\mathcal{O}$(10 km).

In practice, to compute vertical velocity for drifter clusters, we use summation of the drifter layers in place of integration,

$$w(z_n) = -\sum_{i=1}^{n} \frac{1}{2} \left(\left(\frac{du_i}{dx} + \frac{dv_i}{dy} \right) + \left(\frac{du_{i-1}}{dx} + \frac{dv_{i-1}}{dy} \right) \right) \Delta z_i \text{for } N = 1, ..., 4 \,, \tag{1.12}$$

where the subscript 0 corresponds to the ocean surface; $n = 1, ..., 4$ is the level index at which drifter data is available; Δz_i is the vertical spacing between neighboring layers (i.e., $\Delta z_i = z_i - z_{i-1} = -1, -9, -20, -20$ m in our case), divergence at the surface is assumed to be equal to that for the level immediately below (i.e., 1 m in our case). Equation 1.12 assumes a piecewise-linear profile of horizontal divergence (in which values increase or decrease linearly between layers), or equivalently, a piecewise-constant profile (in which the value between two layers is equal to the mean divergence, or half sum, of the two layers).

1.2.5 Estimation of the aspect ratio of the drifter polygon

To compute the aspect ratio, r, of a 2-dimensional polygon spanned by the drifters in any layer, we first compute a dispersion ellipse as in Rypina et al. (2012), Rypina et al. (2016), and Kamenkovich et al. (2015) using drifter positions $x_i(t)$, $y_i(t)$, $i = 1, ..., N$ where N is the number of drifters ($N = 6$ in this case), and then take the square-root of the ratio between the major and minor axes of the ellipse,

$$r = \sqrt{\frac{D_\tau}{D_n}} \ . \tag{1.13}$$

Here

$$D_\tau = D_{xx} \cos^2\theta + D_{xy} \sin 2\theta + D_{yy} \sin^2\theta \tag{1.14}$$

$$D_n = D_{xx} \sin^2\theta - D_{xy} \sin 2\theta + D_{yy} \cos^2\theta \tag{1.15}$$

are the components of the dispersion tensor in the major and minor direction, and

$$\tan 2\theta = \frac{2D_{xy}}{D_{xx} - D_{yy}} \tag{1.16}$$

gives the angle between ellipse's major axis, D_τ and the longitudinal direction, and

$$\begin{aligned} D_{xx} &= \frac{1}{N}\sum_{i=1}^{N}(x_i - \bar{x})^2 \\ D_{yy} &= \frac{1}{N}\sum_{i=1}^{N}(y_i - \bar{y})^2 \\ D_{xy} &= \frac{1}{N}\sum_{i=1}^{N}(x_i - \bar{x})(y_i - \bar{y}) \end{aligned} \tag{1.17}$$

are the components of the 2x2 single-particle dispersion tensor in Cartesian coordinates, with the overbar denoting the mean value for all i.

In three dimensions, the components of the 3x3 dispersion tensor in Cartesian coordinates can similarly be computed as

$$D_{ij} = \frac{1}{N}\sum_{i=1}^{N}(x_i - \bar{x}_i)(x_j - \bar{x}_j) \qquad\qquad i,j = 1,2,3.\ , \tag{1.18}$$

where the 3 eigenvalues and eigenvectors of D_{ij} correspond to the axes of the dispersion ellipsoid.

1.2.6 Estimation of finite-time Lyapunov exponents

The finite-time Lyapunov exponent (FTLE) is a measure of the largest exponential separation rate between a trajectory and its closest neighbors (Haller, 2002, 2015; Shadden et al., 2005). It can equivalently understood to be the exponential rate at which a circular parcel of fluid stretches into an ellipse or ellipsoid. Using d_0 to denote the circle diameter of a set of trajectories at $t = 0$ and $d(\tau)$ to denote the major axis of an ellipse formed by the trajectories at some time $t = \tau$, FTLE values can be estimated as

$$\lambda(\tau) = \frac{1}{\tau}\log\frac{d(\tau)}{d_0}\ . \tag{1.19}$$

In order to calculate FTLEs based on real drifters, we use the same dispersion ellipse-fitting method such as in Equations 1.14-1.17 to determine the major axes of the resulting ellipse. Since the drifters do not form a perfect circle to begin with, this method does not work well for short times.

In numerical models, FTLEs are most often computed by releasing dense grids of regularly-spaced simulated trajectories and then computing the largest eigenvalue (σ) of the right Cauchy-Green tensor (G) evaluated at each particle's initial location using trajectories of its 4 (in 2D) or 6 (in 3D) closest neighbors (Haller, 2002, 2015; Shadden et al., 2005; Lekien and Ross, 2010), i.e.,

$$\lambda = \frac{1}{\tau}\ln\sqrt{\sigma}\ . \tag{1.20}$$

Here $G = \left(\frac{\Delta x_i}{\Delta x_{0,j}}\right)^T\left(\frac{\Delta x_i}{\Delta x_{0,j}}\right)$ and Δx_i and $\Delta x_{0,j}$ are the final and initial distance in the i-th direction between initially nearby particles. A more complete description of the standard FTLE algorithm is described in section 2.2.1. While this method is robust and widely found in literature, it requires regularly-spaced trajectories on a dense grid, and so it is not applicable to irregularly-spaced clusters in drifter experiments.

A modification of the above algorithm for unstructured meshes was proposed by Lekien and Ross (2010). Given the initial and final positions of N particles, the FTLE value at the initial position of the i-th particle can be estimated as

$$\lambda = \frac{1}{\tau} \ln \sqrt{\tilde{\sigma}} \ , \tag{1.21}$$

where $\tilde{\sigma}$ is the largest positive singular value of a matrix $\tilde{M}$,

$$\tilde{M} = DX_f (DX_0)^T (DX_0 (DX_0)^T)^{-1} \ , \tag{1.22}$$

which is a least-squares formula minimizing $||DX_f - MDX_0||$.

Here

$$DX_0 = \begin{pmatrix} x_1^0 - x_i^0 \dots x_{N-1}^0 - x_i^0 \\ y_1^0 - y_i^0 \dots y_{N-1}^0 - y_i^0 \\ z_1^0 - z_i^0 \dots z_{N-1}^0 - z_i^0 \end{pmatrix} \tag{1.23}$$

and

$$DX_f = \begin{pmatrix} x_1^f - x_i^f \dots x_{N-1}^f - x_i^f \\ y_1^f - y_i^f \dots y_{N-1}^f - y_i^f \\ z_1^f - z_i^f \dots z_{N-1}^f - z_i^f \end{pmatrix} \tag{1.24}$$

are matrices containing initial and final displacements between the i-th trajectory and its $N-1$ neighbors. Note that the largest singular value of $\tilde{M}$ is equal to the largest eigenvalue of $\tilde{G} = \tilde{M}^T \tilde{M}$, which is the unstructured-mesh counterpart of the right Cauchy-Green tensor. This method was used to estimate 2-dimensional FTLEs for clusters of 6 drifters. However, due to the several orders of magnitude difference between horizontal $\mathcal{O}$(1 km) and vertical $\mathcal{O}$(1 m) displacements in the elements of DX_0 and DX_f, the method produces unreliable and noisy results for 3D FTLEs. For this reason we use the ellipsoid method such as in Equation 1.18 to estimate FTLEs in 3 dimensions.

In 3-dimensional flows, disparity between 2D and 3D FTLEs is due to two factors: ver-

tical velocity advecting parcels downwards, and vertical shear of horizontal velocity, which causes drifters to separate horizontally between layers. Sulman et al. (2013) introduced a reduced formulation of FTLEs called $\mathrm{FTLE}_{\mathrm{3d2d}}$ which ignores vertical velocity but takes shear into account, i.e. $\frac{\Delta z}{\Delta x_0} = \frac{\Delta z}{\Delta y_0} = 0$, $\frac{\Delta z}{\Delta z_0} = 1$ in G. They studied whether FTLE_{3d2d} can be used to approximate full 3D FTLEs in two idealized flows: a quadrupole model flow and an ABC flow. They found that the method worked well in the former flow but not the latter. Because drifters in our experiment were confined to one depth, it is not possible to compute full 3D FTLEs from drifters, and instead the ellipsoid method allows only for FTLE_{3d2d} to be estimated. We refer to these estimates as 3D FTLEs in this chapter for simplicity and to distinguish from the 2D FTLEs at fixed depth.

A geometrical argument can be used to approximate the contribution from vertical shear of horizontal velocities to 3D FTLEs. In a velocity field with vertical shear and no vertical velocity ($w = 0$), a small ball of fluid with diameter d_0 will tilt and elongate in the vertical plane (x-z), keeping its horizontal extent in the perpendicular direction (y) unchanged. Taking the vertical (x-z) cross-section of the resulting tilted ellipsoid, the major axis (d) of the tilted ellipsoid in the (x-z)-plane at time τ as

$$d(\tau) = \sqrt{d_x^2 + d_z^2} \ , \tag{1.25}$$

where d_x and d_z are the horizontal and vertical components of d, respectively. Because $w = 0$, $d_z = d_{z0} = const$ (=49 m in our case). Assuming that the initial diameter of the ball is small, i.e., $d_0 << d_x$, the horizontal component can be estimated by $d_x(t) \sim \int \Delta v(t) dt$, giving

$$\begin{aligned} \lambda_{shear} &= \frac{1}{T} \log \frac{\sqrt{d_x^2 + d_z^2}}{d_0} \\ &= \frac{1}{T} \log \frac{\sqrt{(\int \Delta v(t) dt)^2 + d_{z0}^2}}{d_0} \ . \end{aligned} \tag{1.26}$$

Since a particle trajectory is an integrated quantity of velocity, the full FTLE is not a sum of its contributions from the horizontal and vertical velocity and horizontal and vertical shear. Nevertheless, comparing λ_{shear} to 3D FTLEs is still informative for quantifying the importance of vertical shear.

1.2.7 Investigating the vertical vorticity balance following drifter trajectories

Absolute vorticity in ocean flows,

$$\vec{\omega}_a = 2\vec{\Omega}_{\text{Earth}} + \vec{\omega} \ , \tag{1.27}$$

consists of both vorticity due to rotation of the Earth itself and rotation seen in the frame of the rotating Earth.

Ignoring friction, the "vorticity equation" which determines evolution of the z-component of absolute vorticity is

$$\begin{aligned}\frac{D}{Dt}\omega^{(z)} &= \left[\omega^{(x)}\frac{\partial}{\partial x} + \omega^{(y)}\frac{\partial}{\partial y} + (2|\omega|\sin\phi)\,\frac{\partial}{\partial z}\right] w - \left(2|\omega|\sin\phi \ + \omega^{(z)}\right)\left(\frac{\partial u}{\partial x} + \frac{\partial v}{\partial y} + \frac{\partial w}{\partial z}\right) \\ &\quad + \frac{\frac{\partial\rho}{\partial x}\frac{\partial p}{\partial y} - \frac{\partial\rho}{\partial y}\frac{\partial p}{\partial x}}{\rho^2} \\ &= \left(\omega^{(x)}\frac{\partial w}{\partial x} + \omega^{(y)}\frac{\partial w}{\partial y}\right) + \left(2|\omega|\sin\phi + \omega^{(z)}\right)\frac{\partial w}{\partial z} + \frac{\frac{\partial\rho}{\partial x}\frac{\partial p}{\partial y} - \frac{\partial\rho}{\partial y}\frac{\partial p}{\partial x}}{\rho^2} \ , \end{aligned} \tag{1.28}$$

where ρ is density and p is pressure.

We would like to study the balance between the time change of vorticity following a water parcel (i.e. the material derivative on the LHS of equation 1.28), the "tilting" of horizontal vorticity into vertical vorticity by vertical velocity (1st term on the RHS of 1.28), stretching of the water column in the vertical direction (2nd term on RHS), and the baroclinic production of horizontal vorticity (3rd term on RHS).

The time derivative and stretching terms of this equation can be estimated from our drifter data, but the tilting and baroclinic production terms require other data. Since different terms describe different physical processes, quantifying and comparing them can shed light on the physical mechanisms that govern subduction and upwelling events near fronts.

1.2.8 Investigating the evolution of horizontal divergence following trajectories

If we ignore friction, the equation which determines the evolution of divergence of horizontal velocity, $\nabla_H \cdot \vec{u} = \frac{\partial u}{\partial x} + \frac{\partial v}{\partial y}$ is given by

$$\frac{D}{Dt}(\nabla_H \cdot \vec{u}) = -\left(\frac{\partial \vec{u}}{\partial x} \cdot \nabla\right) u - \left(\frac{\partial \vec{u}}{\partial y} \cdot \nabla\right) v + \frac{1}{\rho^2}\nabla_H \rho \cdot \nabla_H p - \frac{1}{\rho}\nabla_H^2 p + f\omega^{(z)} - \beta u \ , \tag{1.29}$$

where $\beta = \frac{\partial f}{\partial y}$. The term $\nabla_H \rho \cdot \nabla_H p$ can be interpreted as follows: Suppose a uniform pressure gradient exists in the x-direction (i.e. $\frac{\partial p}{\partial x} = const$ and that $\frac{\partial \rho}{\partial x} > 0$), then a slightly denser water parcel will accelerate at a slower rate than a less dense neighboring parcel, so the two will separate. Similarly for the Laplacian term, if $p_{xx} > 0$ for instance, then a parcel at a slightly more positive x-location will accelerate faster than a parcel at a smaller x-location, and the two will separate. The term $f\omega^{(z)}$ is more easily understood using its individual gradient terms. Take $-f\frac{\partial u}{\partial y}$ for instance and suppose that $\frac{\partial u}{\partial y} > 0$, then a parcel at further y will feel more Coriolis acceleration than a neighboring parcel at smaller y. Finally, the term $-\beta u$ can be understand when considering u that is uniform in y. A parcel with greater y will observe a stronger Coriolis acceleration than a parcel at smaller y, since f is larger at larger y (since $\beta > 0$). This leads to a change in divergence following the parcel. The vorticity and divergence equations are commonly-used tools in literature. A more complete description of these equations can be found in classical oceanographic and meteorological texts, such as Holton and Hakim (2013), Dutton (2002), or Pedlosky (1987).

The terms that can be estimated exclusively from our drifter data are $\frac{D}{Dt}\nabla_H \cdot \vec{u}$, $f\omega^{(z)}$ and $-\beta u$, whereas all other terms require additional data from other observational platforms.

1.2.9 Bootstrapping uncertainty analysis of divergence and vorticity

We compute standard deviation intervals for drifter-based estimates of both divergence and vorticity in order to estimate uncertainty, using the bootstrapping method described by Efron (1979). This involves re-applying the linear least squares (LLS) procedure to the 6 subsets composed from any 5 of the 6 drifters at each depth to generate 6 (time-dependent) divergence and vorticity estimates, and then the (time-dependent) standard deviation of this ensemble are computed to estimate the uncertainty of divergence and vorticity values.

1.2.10 Uncertainty in divergence and vorticity due to the GPS positioning errors

Error due to GPS positioning can be approximately represented by white noise with a standard deviation of 5 m ($\sigma_x = 5$ m). This GPS estimate is provided by the manufacturer

(https://www.findmespot.com/en-ca/support/spot-satellite-gps-messenger/get- help/messaging/how-accurate-is-the-spot-satellite-gps-messenger-w) and is consistent with other sensitivity tests done at WHOI. Although the accuracy of the SPOT GPS Trackers may vary with location due to varying satellite coverage, we expect similar standard deviation values for our study region near the Almería-Oran front since the Mediterranean Sea typically has thorough satellite coverage. Errors in consecutive GPS fixes are uncorrelated, so they contribute in quadrature to the velocity errors that result from velocity approximations that come from GPS positions. In other words, $\sigma_u = \frac{\sqrt{2}\sigma_x}{2\Delta t} = 1.18 \times 10^{-2}$ m/s for $\Delta t = 5$ min. To reduce noise, a 10-minute (3-point) moving average window is applied to the velocity time series, giving $\sigma_{<u>} = \frac{\sigma_u}{\sqrt{3}} = 6.8 \times 10^{-3}$ m/s. This gives us an approximate upper bound on the error in our estimated velocity gradient terms of: $\sigma_{\partial u/\partial x} = \frac{\sqrt{2}\sigma_{<u>}}{\Delta x}$. Applying again a sliding 10-minute moving average window to the gradient time series decreases the standard deviation by another factor of $\sqrt{3}$, so $\sigma_{\partial u/\partial x} = 5.5 \times 10^{-6}$ 1/s. Summing the two gradient terms each required for divergence and vorticity increases the standard deviation of divergence and vorticity by $\sqrt{2}$, so $\sigma_{\nabla_H \cdot \vec{u}} = \sigma_{(\nabla \times \vec{u}) \cdot \hat{z}} = 7.8 \times 10^{-}6$ 1/s. Finally, applying applying the 10-min averaging to the divergence and vorticity time series once more reduces the errors by another $\sqrt{3}$, giving $\sigma_{<\nabla_H \cdot \vec{u}>} = \sigma_{<vort(\vec{u})>} = 4.6 \times 10^{-}6$ 1/s, which is an order of magnitude smaller than the Earth Coriolis parameter in this region. Note, however, that this error estimate depends on the moving-average window (which allows trading resolution for precision) and would have be larger if the smoothing window was shorter or not applied. The 3-point 10-min moving-average window (twice the sampling interval) was applied, which coincides with the time resolution of the drifter-based velocity estimates computed by center-differencing drifter positions. More rigorous analysis of errors in velocity gradients, vorticity, and divergence can be found in Kirwan and Chang (1979), Ohlmann et al. (2005), Haza et al. (2014), and Spydell et al. (2019). Compared to the more rigorous estimates found in Kirwan and Chang (1979) for instance, this estimate does not account for errors from aliasing of under-sampled motions on scales comparable to the sampling interval. This error estimate was numerically checked by adding a random noise with standard deviation of 5 m to simulated drifters from the model, and then applying the identical smoothing and Least Squares algorithms to compute vorticity and divergence. the resulting variance is similar and of the same magnitude as our back-of-the-envelope error calculation. Note, however that model resolution (2 min) is only slightly smaller than the GPS sampling period (5 min), so this estimate might still miss contributions from aliased small scale motions that are present in real flows. Our estimate also does not account for the geometry of the drifter polygon or cross-drifter error covariances; these effects have been investigated by Spydell et al. (2019).

1.2.11 Ekman analysis of real drifters using bulk flux algorithms

It was hypothesized that the separation between drifter layers could be due in part to strong westerly or southwesterly winds that persisted in the days after the drifters were released. The first day after release saw relatively small magnitude winds with highly variable direction, during which drifters layers saw minimal separation. After the first day, winds from the west and southwest were observed and remained for several days. These winds are shown for day 2.5 in Figure 1-6. The winds may have caused "Ekman currents" which would push drifters near the surface in an Eastward direction, but would have minimal effect on drifters at depth.

Since momentum exchange between the atmosphere and ocean is usually difficult to measure directly without specialized equipment, bulk formulas that relate fluxes to more easily measurable variables such as wind speed, temperature, and humidity are often used. A bulk formula for wind stress over the ocean is given as

$$\tau = \rho_a C_D \left(\Delta U\right)^2 \ , \tag{1.30}$$

where τ is the magnitude of the wind stress, ρ_a is the density of air, C_D is the drag coefficient that must be parameterized, and ΔU is the difference in wind speed between the atmosphere and ocean (Edson et al., 2013).

A mix of gridded observations and model data were used to compute wind stress. Atmospheric temperature, relative humidity, and atmospheric pressure are from the Atmospheric Infrared Sounder (AIRS) Level 3 Data with daily 1 degree resolution. Sea Surface Temperature (SST) was taken from the Multi-Scale Ultra High Resolution (MUR) Level 4 SST data with daily 0.01 degree resolution. Wind velocity data was provided by the Western Mediterranean Operational Forecast System (WMOP) implemented by SOCIB (Balearic Islands Coastal Observing and Forecasting System). WMOP is based on a configuration of the Regional Ocean Modeling System (ROMS) and uses boundary conditions provided by the Mediterranean Forecasting model from the Copernicus Marine Service (Mourre et al., 2018). Winds were provided as hourly data with 2 km resolution.

The COARE 3.5 drag coefficient parameterization described in Edson et al. (2013) was used to compute wind stress along trajectories. The COARE drag coefficient is expressed as a function of atmospheric stability and surface roughness,

$$C_D(\frac{z}{z_0}, \frac{z}{L}) = \left[\frac{\kappa}{\ln(\frac{z}{z_0}) - \psi_m(\frac{z}{L})} \right] \ , \tag{1.31}$$

where z is the height above the surface, κ is the von Karman constant, z_0 is the roughness length, L is the Monin-Obukhov (MO) length, and ψ_m is an atmospheric stability function described in Edson et al. (2013).

The atmospheric temperature, SST, relative humidity, atmospheric pressure, and wind data were first linearly interpolated in both time and space hourly on a 2 km grid, and wind stress was computed at each location. Next, this grid of wind stress values was linearly interpolated along drifter locations. Ekman currents were computed using the standard Ekman boundary-layer solutions,

$$\begin{aligned} u_{\text{ek}} &= \frac{\sqrt{2}}{\rho f d} e^{-z/d} \left(\tau_x \cos(\frac{z}{d} - \frac{\pi}{4}) - \tau_y \sin(\frac{z}{d} - \frac{\pi}{4}) \right) \\ v_{\text{ek}} &= \frac{\sqrt{2}}{\rho f d} e^{-z/d} \left(\tau_x \sin(\frac{z}{d} - \frac{\pi}{4}) + \tau_y \cos(\frac{z}{d} - \frac{\pi}{4}) \right) \ , \end{aligned} \tag{1.32}$$

where d is the Ekman depth, which was computed in this case by the wind-speed dependent formula,

$$d = \frac{3.2U}{\sin(\phi)} \ , \tag{1.33}$$

where U is the wind speed magnitude and ϕ is latitude. After Ekman currents were computed along trajectories, the displacement of each drifter that can be attributed to Ekman currents was computed as

$$\begin{aligned} s_x &= \int_S u_{\text{ek}}(t) dt \\ s_y &= \int_S v_{\text{ek}}(t) dt \ , \end{aligned} \tag{1.34}$$

where s_x is zonal displacement, s_y is meridional displacement, and S represents the trajectory curve along which currents are being integrated.

1.2.12 High-resolution ocean circulation model and analysis of simulated drifters

An ultra-high-resolution simulation of the SOCIB WMOP ocean circulation modelling system implemented at SOCIB (Balearic Islands Coastal Observing and Forecasting System (Tintoré et al., 2013) to quantify uncertainties of the multi-layer drifter-based estimates of divergence, vorticity, and vertical velocity. The WMOP model is based on a configuration of the Regional Ocean Modelling System (ROMS - www.myroms.org). It covers the Western Mediterranean Sea with a spatial resolution of 2 km (Juzà et al., 2016; Mourre et al., 2018). Boundary conditions were provided by the Mediterranean Forecasting model from the Copernicus Marine Service. Additionally, two-way nesting was initiated between the 2 km grid and a 400 m resolution domain covering the region where real drifters were located during the first 25 hours after deployment (the nested grid extends from -3.52^{o}E to -1.02^{o}E and from 35.06^{o}N to 36.84^{o}N; see Figure 1-8a). The SOCIB WMOP model also had 32 vertical terrain-following layers, resulting in a vertical resolution varying from 2 m at the surface to 8 m at 50 m depth in the area of the drifter deployments. The model was forced by the realistic atmospheric forcing from the Spanish Meteorological Agency HIRLAM model with a 5 km and 1-hourly resolution. The nested simulation was initialized on May 28, 2018 from the 2 km resolution WMOP reanalysis product which assimilated data from satellite products (temperature and sea level anomalies), Argo temperature and salinity profiles, and from HF radar surface currents in the Ibiza Channel. The Ensemble Optimal Interpolation procedure used to assimilate the data is described in Hernandez-Lasheras and Mourre (2018) and Mourre et al. (2018). The nested simulation was then run without additional data assimilation updates. This approach allowed us to create a simulation initialized from a state as close as possible to real conditions, but fully governed by model equations at high resolution. Model temperature, salinity, density, sea velocity, and wind stress fields were saved at 2-min temporal resolution within the 400-m resolution domain over 48 hours starting on Jun 1, 2018. In spite of many differences in the magnitude and exact positions of the current structures, comparisons with the data from satellites, drifters, gliders and u-CTD sections taken during the same cruise showed that the model solution provided a realistic representation of the Almería-Oran front and associated salinity gradients (Garcia-Jove et al., 2020) (CALYPSO website, https://calypsodri.whoi.edu/). While horizontal velocities are explicitly solved for in the WMOP model, vertical velocities are diagnosed from integration of the continuity equation at each model grid point.

Eulerian velocity gradients were computed by finite-difference model velocities between neighboring grid points. Simulated drifters were released into the 400 m resolution model

at the same locations, depths, and times as real drifters, and were next advected by the model. The MATLAB function ode45 (a 4th order variable-timestep Runge-Kutta integration scheme) along with bi-linear velocity field interpolation in time and space was used to integrate trajectories. Simulated trajectories were saved at 5 min time intervals to match real drifter data.

Estimates for simulated drifter divergence, vorticity, and vertical velocity were computed using the same methods as real drifters, and were then compared to the Eulerian model values for the same quantities (when interpolated to simulated drifter positions). Correlation coefficients were next used to quantify agreement between the Lagrangian drifter estimates and Eulerian field values. Two additional experiments were also run: one in which Eulerian model divergence was used to estimate vertical velocity rather than drifter-based LLS estimates (this includes errors due to lateral separation of layers but not errors due to the LLS method), and one in which Eulerian model divergence was used at 4 depths following the center of mass of the drifter clusters (this includes no errors due to lateral separation or the LLS method, and only includes errors due to sparse integration of 4 layers rather than a more dense field).

Model-based Ekman currents were also estimated by using model output of wind stress and applying the Ekman layer depth formula from Equation 1.33, and computing Ekman currents as above in Equation 1.32. A 2-day running average to model wind stress and wind speed were also applied, since the Ekman layer depth does not instantaneously adjust to wind speed.

1.3 Results

1.3.1 Analysis of Real Drifters

A spaghetti diagram of trajectories of 24 drifters with drogues at different depths is shown in Figure 1-1, color-coded by drogue depth. After release, drifters at all depths began moving anticyclonically around the northwestern edge of the Eastern Alboran Gyre, reaching their northernmost location after about 25 hours.

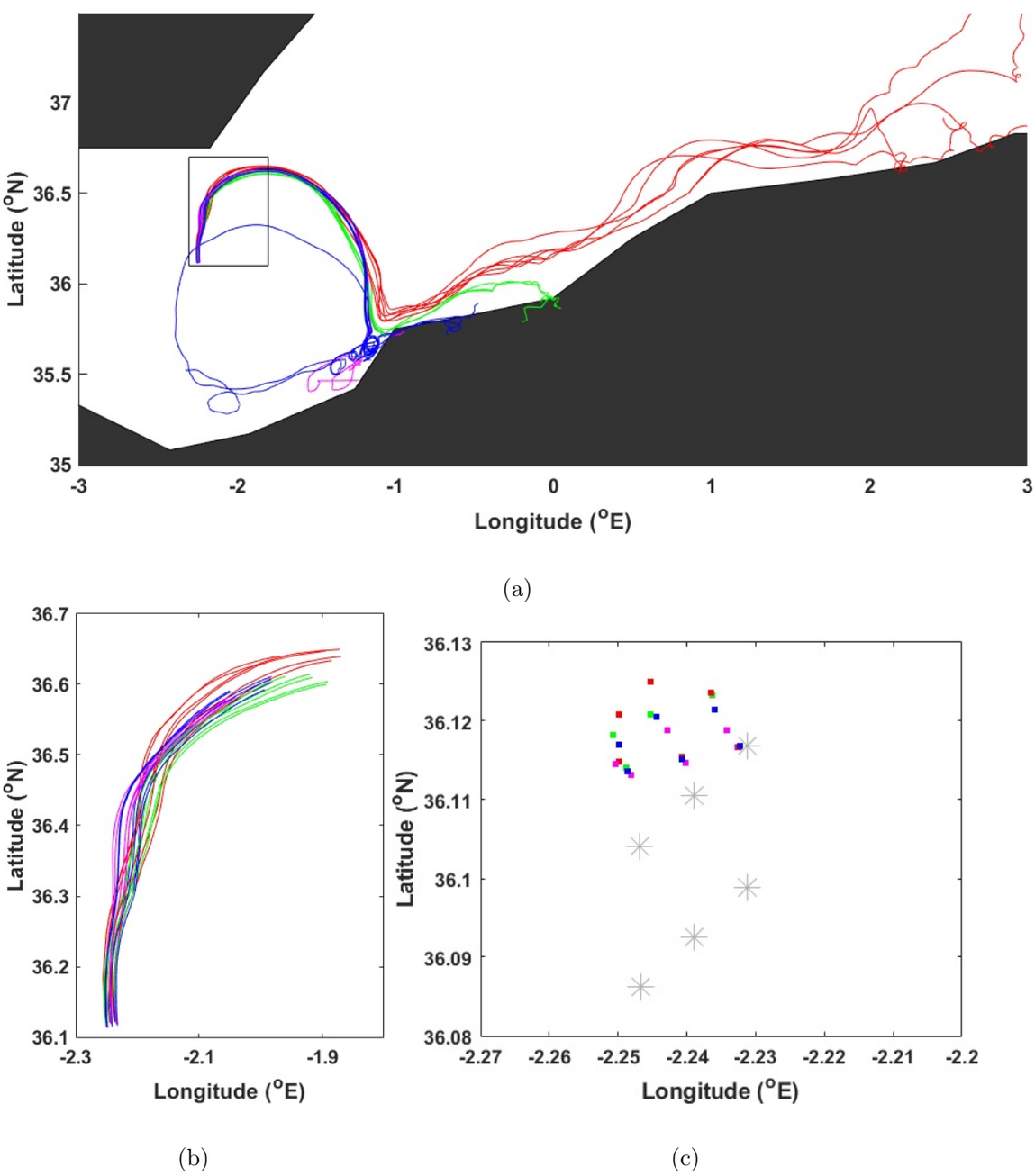

(a)

(b)

(c)

Figure 1-1: Trajectories of drifters, color-coded by drogue depth. 25-hour trajectory segments are encompassed by the black box. Solid black area represents land. The left inset shows a zoomed-in view of the 25-hour trajectory segments. The right inset shows deployment station locations (asterisks) and drifter locations at the time when the last drifter was released (squares).

Oceanic currents were surface-intensified, causing the upper layers of drifters to move faster than the lower layers, and so the top layers split from the bottom layers and moved

eastward. After the 25 hour period of our analysis, this separation reached $\mathcal{O}(10$ km) between the top and bottom layers. A plot of the separation between the center of mass of the top and bottom layers is shown in Figure 1-2a.

In incompressible 2D flows, the area of a 2D fluid element remains constant as the flow progresses in time. A polygon formed by a finite number of drifters is not a material curve surrounding a fluid element, so the area of this polygon is not necessarily conserved even in incompressible flows. However, it should be nearly conserved given that there are a large number of drifters within a tight space, so that a material contour is sufficiently spanned by the drifters. Therefore, any large changes in area of this polygon over time should approximately indicate the present of divergence (or convergence) in the flow, i.e. $\nabla_H \cdot \vec{u} = \frac{du}{dx} + \frac{dv}{dy} \neq 0$. During the first 25 hours of the experiment, the all 4 layers of drifters increased in time, with the largest growth being that of the first layer (1 m) and the smallest growth being that of the deepest layer (50 m).

It is typical in ocean flows for a fluid element to stretch into a long and narrow filament, due to time-dependent horizontal shear and strain of horizontal velocities. The drifter distributions at each layer observed this behavior, and drifters at each layer had an increase in their aspect ratio. A plot of aspect ratio vs. time for each of the drifters is shown in Figure 1-2c. The deepest cluster of drifters stretched most rapidly, reaching an aspect ratio of 10 after 12 hours. All layers reached an aspect ratio of 10 or above after 25 hours.

Figure 1-2f shows vertical velocity estimated by integrating LLS estimates of divergence downward. The time series are predominantly dominated by upwelling (positive vertical velocity), with a few instances of isolated downwelling. Upwelling is generally estimated to be larger at depth than near the surface, with the 50 m layer reaching a maximum estimate of 3.3 mm/s. The strongest downwelling event occurred in the 50 m layer at about hour 19 and reached about 1 mm/s. The vertical velocity is also seen to change sign between 1 m and 50 m in a few instances.

As shown in Figure 1-3a through 1-3d, LLS estimates of drifter-based divergence in the first three layers (1 m, 10 m, 30 m) agree well with estimates using the area method from Equation 1.7 and the circulation method from Equation 1.11. Correlation coefficients between the three methods of estimates are 0.7-0.9 for the top three levels during the first 25 hours. At 50 m however, the LLS estimate of divergence correlates well with the circulation estimate (correlation coefficient of 0.8) but does not agree well with the area method (cor-

relation coefficient of 0.33). Agreement becomes worse over time, likely because the aspect ratio became large at a faster rate than other layers. This agrees with Essink (2019) who concluded, using a high-resolution numerical model, that the LLS method fails with large aspect ratios. For vorticity, there is a good agreement between the LLS estimate and the circulation estimate (with correlation coefficient of 0.8).

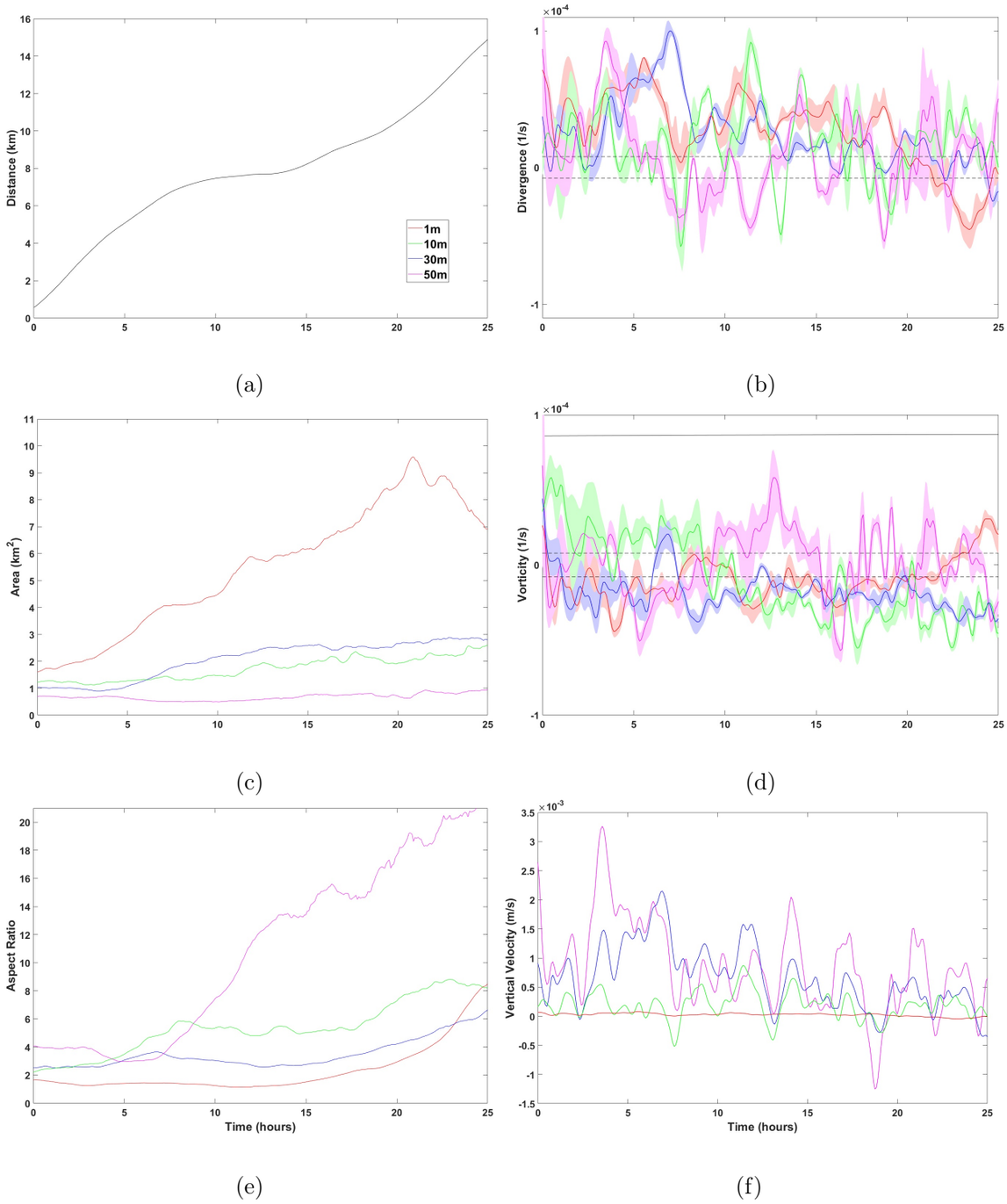

Figure 1-2: Drifter-based estimates of (a) separation between the center of mass of the drifter distribution at 1 m and at 50 m), (c) area of the polygon formed by the drifters, (e) aspect ratio of the polygon, (b) divergence, (d) vorticity, and (f) vertical velocity at 4 depths. In panels b and d colored stripes show the ±1 standard deviation interval from bootstrapping method. The dashed black line shows ±1 standard deviation estimates due to GPS uncertainty, and the solid black line shows the value of f. Color notation is the same as in Figure 1-1.

Figure 1-2d and 1-2e show divergence and vorticity estimates using the LLS method, along with ±1 standard deviation interval from the bootstrapping method described in section

1.2.9. Divergence and vorticity change sign multiple times and estimates are of the same order of magnitude as the Earth Coriolis parameter f at all layers.

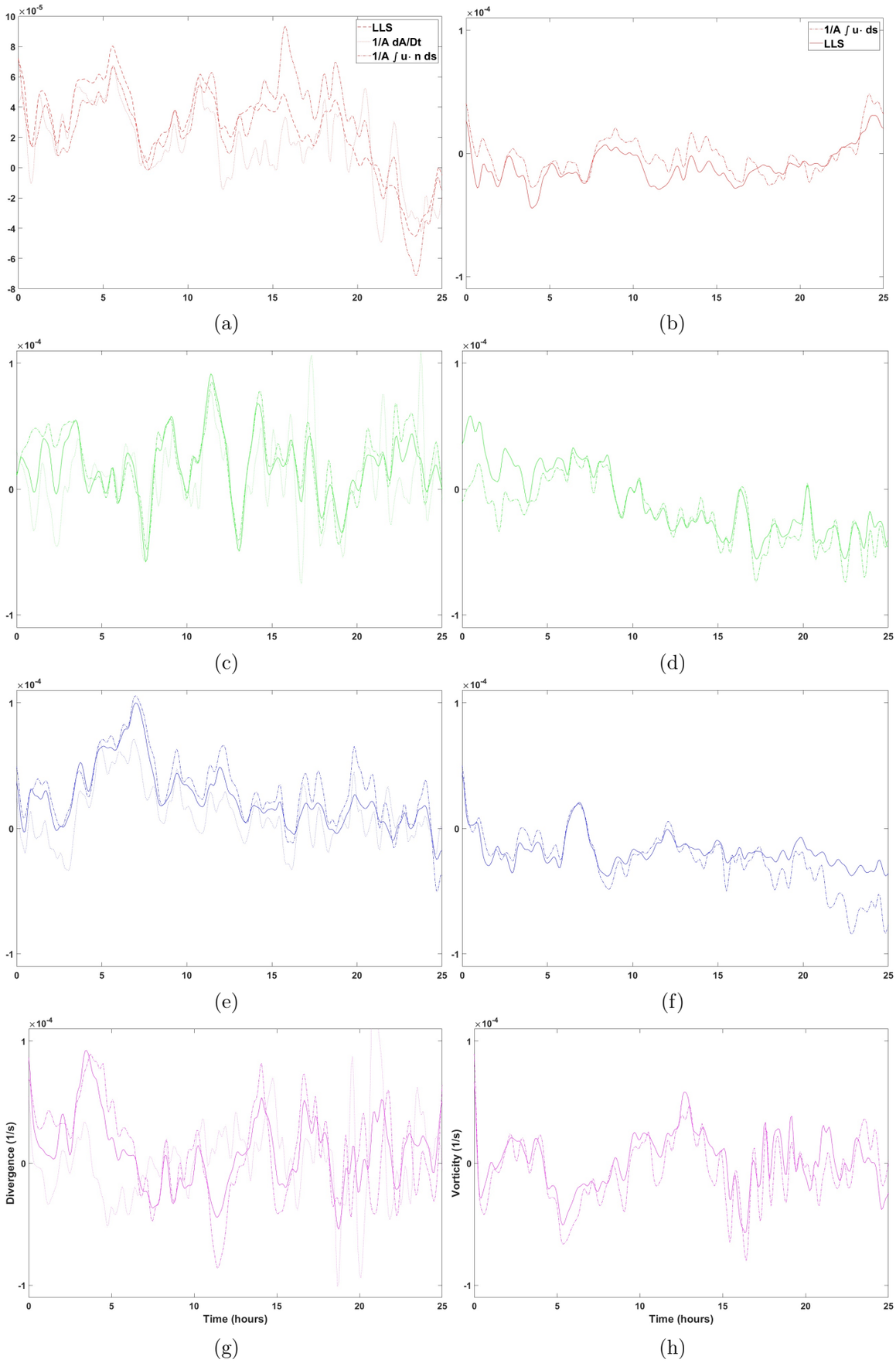

Figure 1-3: Drifter-based divergence (a,c,e,g) and vorticity (b,d,f,h) estimated using different methods at 1 m (a,b), 10 m (c,d), 30 m (e,f), and 50 m (g,h). Color notation is the same as in Figure 1-1.

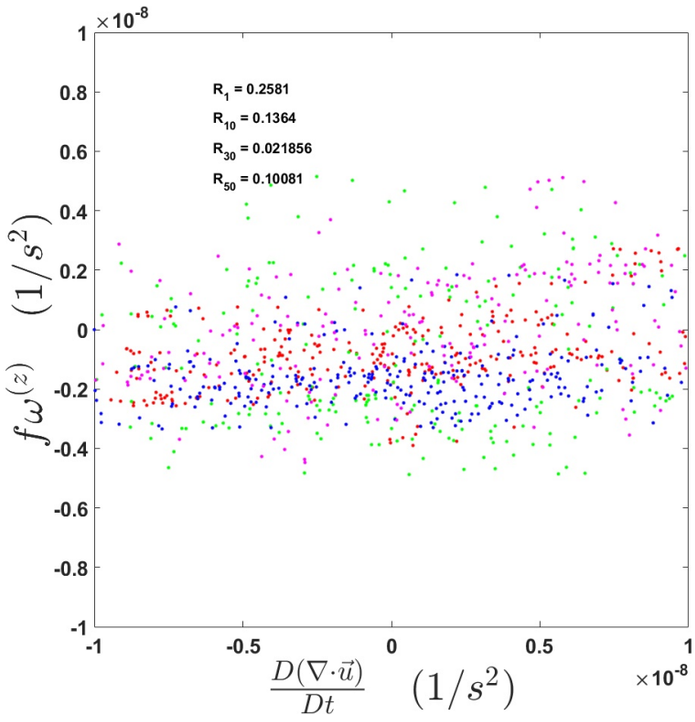

(a)

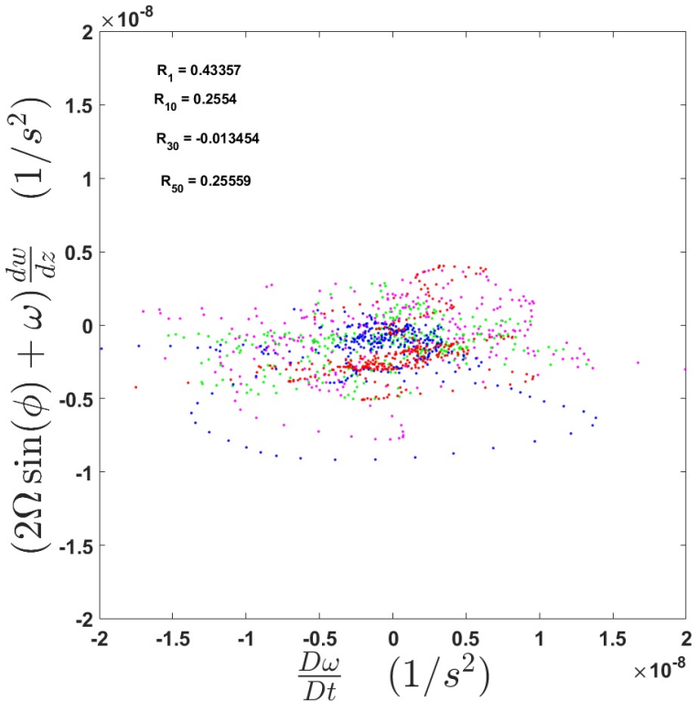

(b)

Figure 1-4: The relationship between estimated terms in the (a) horizontal divergence balance equation, and (b) vertical vorticity balance equation. Correlation coefficients are shown at the top left corner of each subplot. Color notation is the same as in Figure 1-1.

Figure 1-4a shows estimated terms from the divergence equation based on drifter data. Both the material change in the horizontal divergence $\frac{D}{Dt}\nabla_H \cdot \vec{u}$ and the term $f\omega^{(z)}$ are $\mathcal{O}(10^{-8})\text{s}^{-2}$. The terms do not correlate well with each other, however, with the total range of variability for the material derivative being 4-5 times larger than $f\omega^{(z)}$. The term βu much smaller ($\mathcal{O}(10^{12}\ \text{s}^{-2})$). Figure 1-4b shows estimated terms of the vorticity equation based on drifter data. Once again, the magnitudes of both the material change in vertical vorticity and the vortex stretching term are of similar magnitude to each other ($\mathcal{O}(10^{-8})\text{s}^{-2}$),

but the range of variability for the rate of change term being roughly twice larger than for the vortex stretching term. The two terms are not well-correlated with each other at any depth, with correlation coefficients between -.05 to .45.

Figure 1-5 shows FTLE estimates for drifter clusters (2D) and for the entire collection of drifters (3D). Higher FTLE values in upper layers indicate stronger separation between drifters compared to lower layers. The 2D FTLE curves at each depth are relatively variable initially but become significantly smoother between hours 12 and 25. 3D FTLEs (using the ellipsoid method described in section 1.2.6) shows a local minimum at 1 hour followed by a maximum at 3 hours, and decreases monotonically after the maximum to its final value of about $\times\ 10^{-5}$ s^{-1} at 25 hours. The 3D FTLE estimate may not be reliable for the first several hours since the drifters were not deployed in a sphere and were not aligned with the most unstable direction of flow. At 3 hours and onward, the 3D curve agrees well with the semi-analytic estimate of vertical-shear-induced drifter separation from Equation 1.26, suggesting that the drifters sufficiently aligned themselves with the unstable direction, so the 3D ellipsoid FTLE method may be more reliable at greater times. This agreement also suggests that drifter-based 3D FTLE estimates are dominated by vertical shear of horizontal velocity.

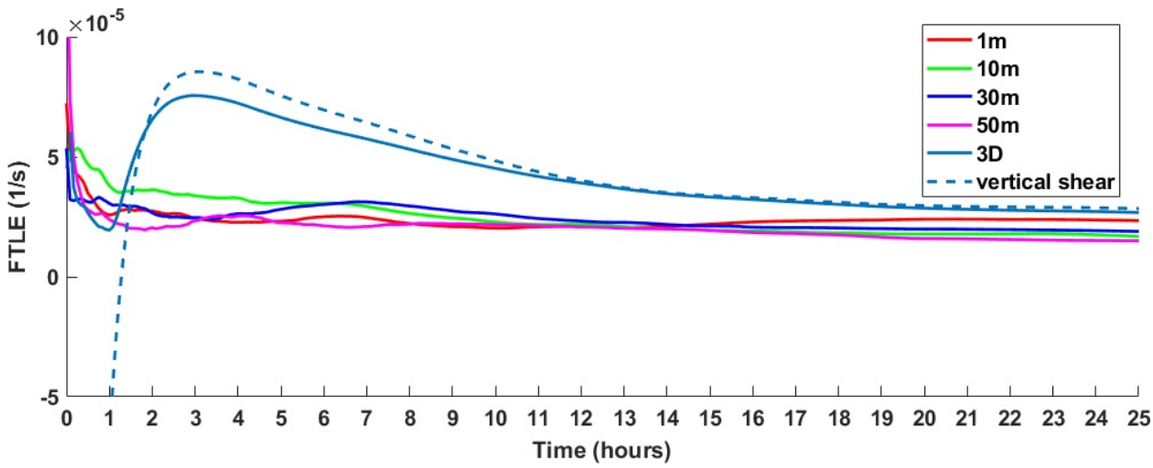

Figure 1-5: Estimates of 3D and 2D FTLEs at 4 depths using drifter-based measurements. 3D FTLEs were computed using the ellipsoid fit method. 2D FTLEs were computed using the unstructured grid method. Dashed curve shows the FTLE induced by the vertical shear of horizontal velocity.

Figure 1-6 shows winds superimposed along with drifter trajectories. These winds predominantly come from the southwest, indicating that the wind may have intensified currents in the shallow layers in the eastward direction. Figure 1-7a shows computed Ekman currents using bulk flux algorithms, computed for the center of mass of drifters within a layer. Figure 1-7b shows accumulated Ekman displacement for the center of mass of drifters in each layer. Results show that Ekman currents likely contributed to the Eastward displacement of the drifters at 1 m and 10 m. After 3 days, the total zonal displacement of the 1 m layer was

around 6 km. The real displacement between the 1 m and 30/50 m layers is closer to around 10-15 km, however a 6 km displacement may have been sufficient to push the upper drifters outside of the gyre and into the Eastward-flowing jet (which could presumably account for the remaining separation). Between days 3 and 4, an additional ∼6 km of Eastward zonal displacement occurred in the top layer, meaning that as the experiment progressed, wind stress may have been intensifying the flow of the jet, continuing to contribute to separation between drifter layers.

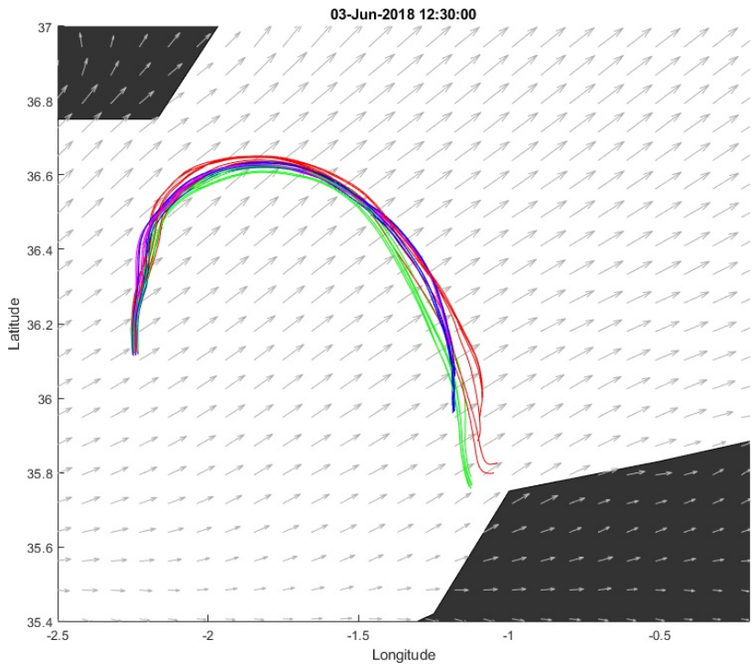

Figure 1-6: Drifter trajectories up to 2.5 days, with winds shown as grey arrows. Winds between days 2 through 4 are predominantly southwesterly.

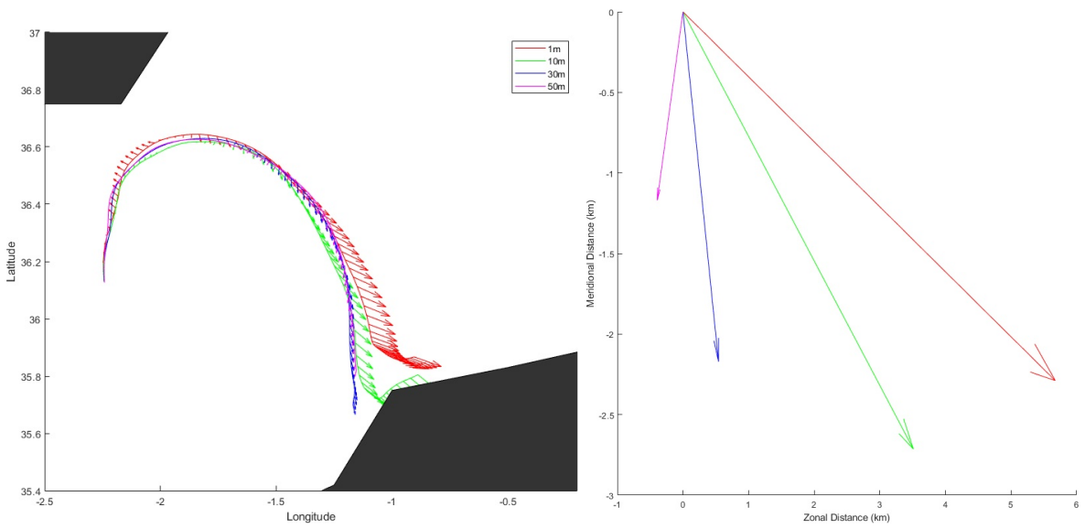

(a) (b)

Figure 1-7: Panel (a): Ekman currents shown at one hour intervals over three days. The colored lines represent the center of mass of all drifters in each layer. Colored arrows represent the direction and relative magnitude of Ekman currents. The displacement between the 1 m layer and the bottom layers is around 10-15 km after three days. Panel (b): Accumulated Ekman displacement over three days. Estimated zonal displacement due to Ekman currents for the 1 m layer is 6 km Eastward.

1.3.2 Analysis of Simulated Drifters

Figure 1-8a shows trajectories of simulated drifters. Currents in the model are slightly weaker in the model compared to the real ocean, so the 25-hour drifter trajectories are slightly shower than real trajectories (the limits of which are roughly shown by the black rectangle in Figures 1 and 6a). The Eastern Alboran Gyre appears to be shifted slightly to the southwest in the model. Regardless, the simulated drifters are in decent qualitative agreement with real drifters. The simulated drifters move anticyclonically around the northwestern edge of the gyre, and later split apart, with the two bottom layers recirculating in the gyre while the two upper layers move eastward.

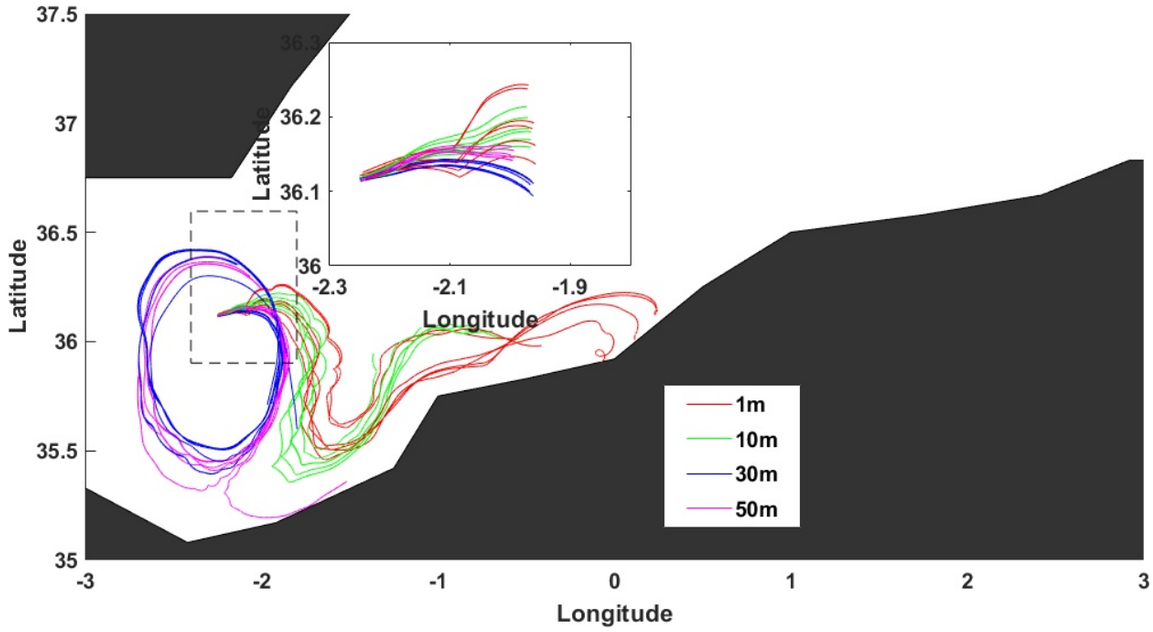

(a)

Figure 1-8: Simulated drifter trajectories from the SOCIB WMOP model. Trajectory segments outside of the 400-m-resolution model domain (dashed box) and/or past 48 hours after deployment were computed using the 2-km-resolution model velocities. The solid black box encircles the 25-hour-long trajectory segments, which are also shown in the small inset.

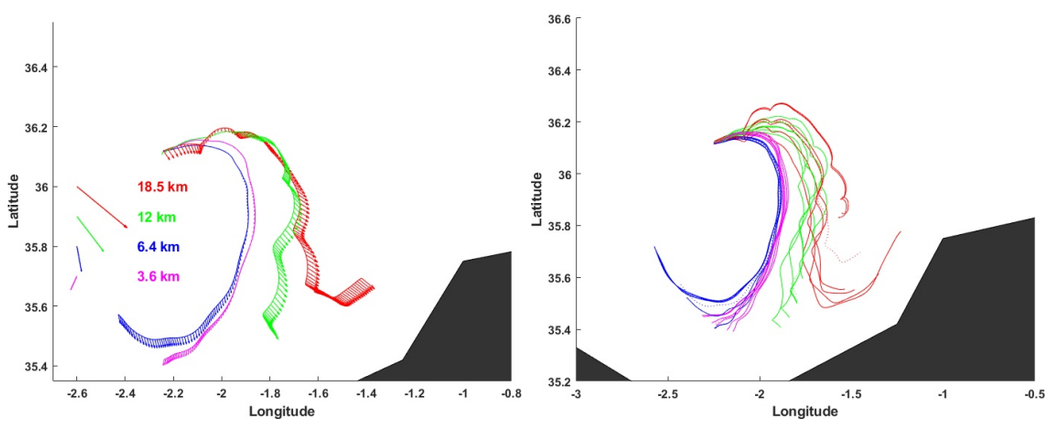

(a) (b)

Figure 1-9: Panel (a) shows Ekman currents at the center of mass of the drifter distribution at each level every 5 min for 5 days, and the cumulative Ekman displacements after 5 days. Panel (c) shows simulated trajectories advected by the model currents with the Ekman velocity fields removed.

Figure 1-9a shows Ekman currents indicated by colored arrows along trajectories, as well as accumulated Ekman displacement (magnitude and direction of which are indicated by the colored arrows on the left side of the figure). The splitting between the top two and bottom two layers is consistent with the effect of Ekman currents pushing the top two layers eastward at a greater rate than the bottom two layers. When Ekman currents are removed from the model velocity fields, the trajectories of simulated drifters at 10 m are shown to recirculate instead of heading eastward. This shift is not strong enough, however, to push the 1 m trajectories back into the gyre.

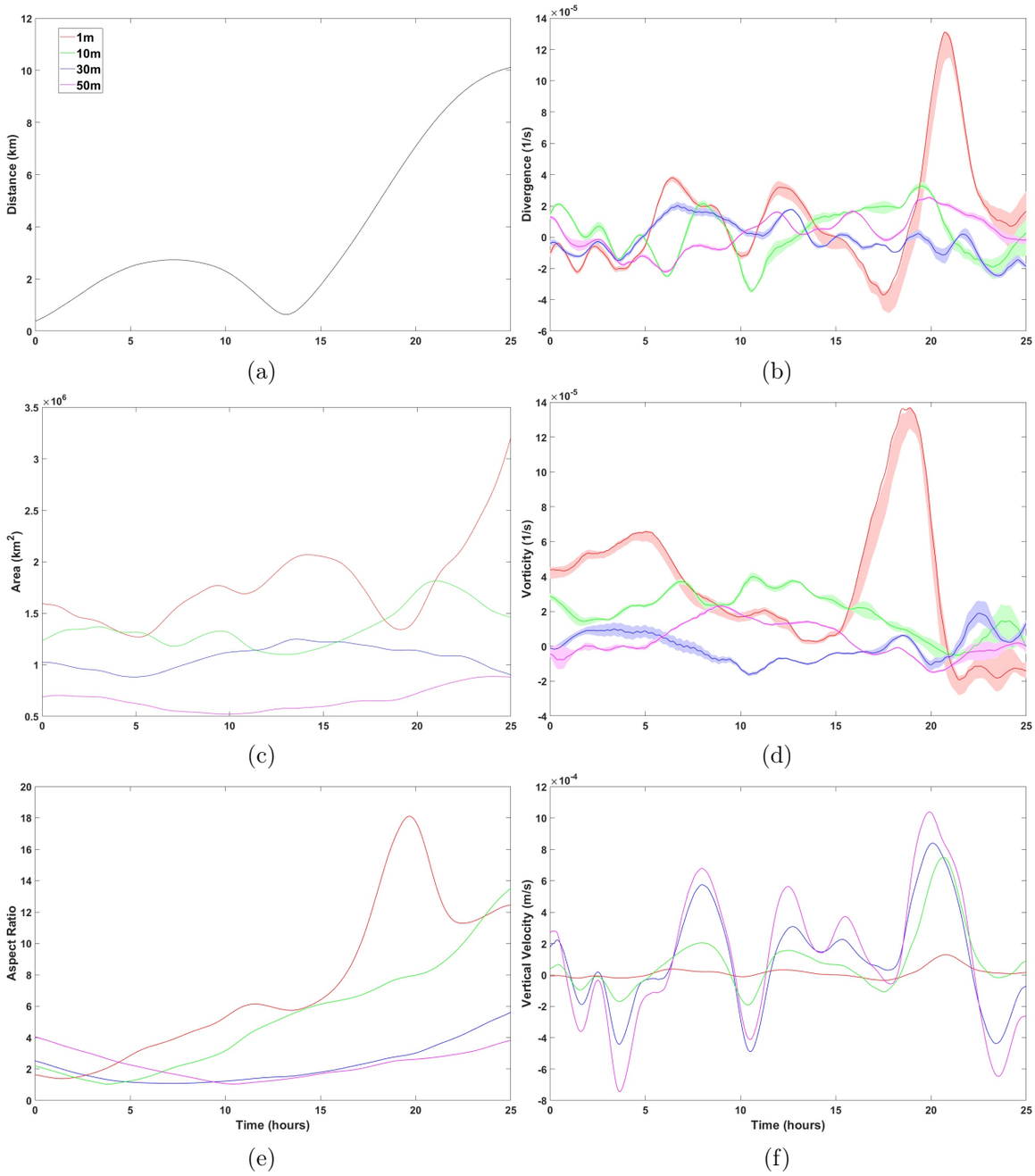

Figure 1-10: Same content as Figure 2 but for the simulated drifter release in SOCIB WMOP

Estimates of displacement, polygon area and aspect ratio, divergence, vorticity, and vertical velocity derived from simulated drifters are shown in Figures 1-10a through 1-10f. Displacement between the top and bottom layers of simulated drifters remained $\sim 30\%$ smaller than the displacement of real drifters after 25 hours. Growth in polygon area is generally

slower for simulated drifters compared to real drifters, particularly at 1 m. simulated drifters elongate more quickly however, as shown by the aspect ratio time series, which grows significantly faster for simulated drifters at 1 m, comparably to real drifters at 10 m, and slower than real drifters at 30 m and 50 m. The 1 m layer grows to a particularly high maximum of 25 after 22 hours. Estimates of divergence and vorticity in the model are about 2-3 times smaller than for real drifters, except at 1 m where the values are comparable. Divergence and vorticity estimates in the model are also much smoother in time than their real drifter counterparts. Simulated divergence and vorticity estimates generally oscillate around zero and switch signs multiple times for both real and simulated drifters, with the exception that simulated vorticity for depths 1 m and 10 m are predominantly positive, unlike real drifters. While quantitatively, simulated vertical velocities are about 3 times smaller in the model compared to real drifters, they are qualitatively similar, being larger $\mathcal{O}(1$ mm/s) at 50 m compared to small values at the surface. Vertical velocities also switch sign multiple times at all depths, just as for real drifters. Simulated estimates suggest a roughly equal amount of positive and negative vertical velocities, while real drifters showed predominantly only positive vertical velocities.

Excellent agreement exists between all methods for estimating divergence and vorticity to the model "truth," as shown in Figure 1-11 (also see correlation coefficients for "vorticity" and "divergence" in Table 1.1. One exception is the LLS estimates of divergence and vorticity in the top layer, which disagree with truth at about hour 15 and onward. This disagreement is likely due to a high aspect ratio of the drifter polygon for the top layer (as shown in Figure 1-10c). The standard deviation estimated from the bootstrapping method during these times also become large, further confirming that LLS estimates are less reliable at around 15 hours and beyond.

	Vorticity	Divergence	Vertical velocity	laterally stacked	vertically stacked
1 m	-0.18 (0.95)	0.72	0.71	0.99	0.99
10 m	0.9	0.96	0.31	0.44	0.82
30 m	0.9	0.96	0.50	0.48	0.92
50 m	0.96	0.99	0.41	0.48	0.89

Table 1.1: correlation coefficient between the Eulerian model "true" values of vorticity, divergence and vertical velocity in the 400 m SOCIB WMOP simulation, and estimates obtained using different drifter-based methods. Divergence, vorticity and vertical velocity in the left 3 columns were obtained for simulated drifters. "Laterally separated" and "vertically stacked" refer to simulations where Eulerian model divergence at 4 depths were used at the locations corresponding to the center of mass of the 6 drifters at 4 depths, or at the same geographical location, respectively.

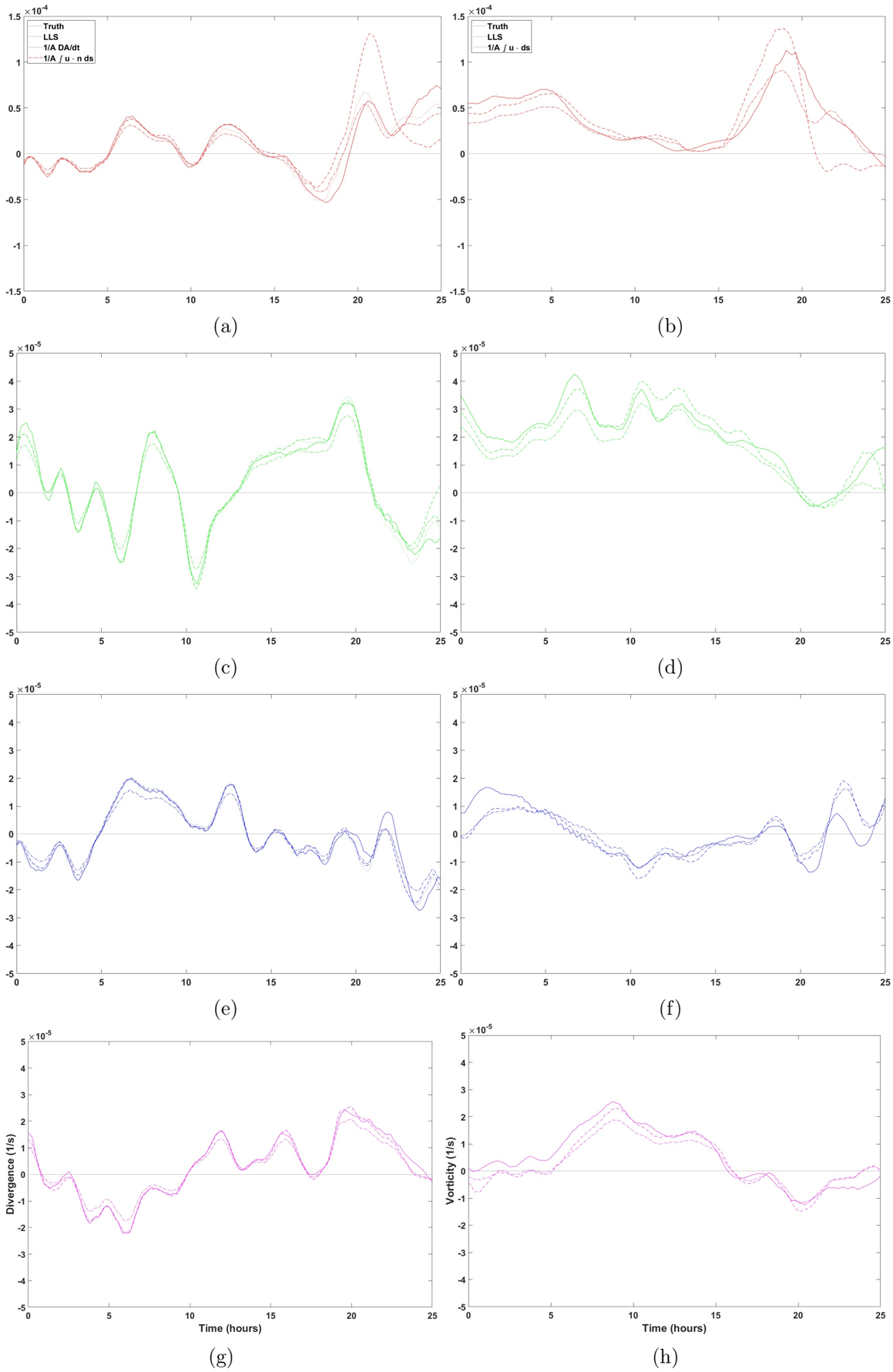

Figure 1-11: Eulerian model divergence and vorticity (solid) and simulated-drifter-based Lagrangian divergence (a-d) and vorticity (e-h) estimated using different methods (as indicated by the legend) at 1 m (a,e), 10 m (b,f), 30 m (c,g), and 50 m (d,h).

Correlation between Eulerian w in the model and divergence-based estimates are relatively high at 1 m (0.71) but low at all other depths (0.3-0.5). Using Eulerian model divergence values rather than LLS-derived values only slightly improved the estimates (cor-

relation to "true" values in the three bottom layers increased to about 0.5). Removing the lateral shift between layers and integrating downwards using layers from the same geographic location significantly improves estimates (correlation coefficients rise to 0.82 - 0.99). These coefficients can be seen in Table 1.1 under the "vertical velocity," "laterally separated," and "vertically stacked" columns.

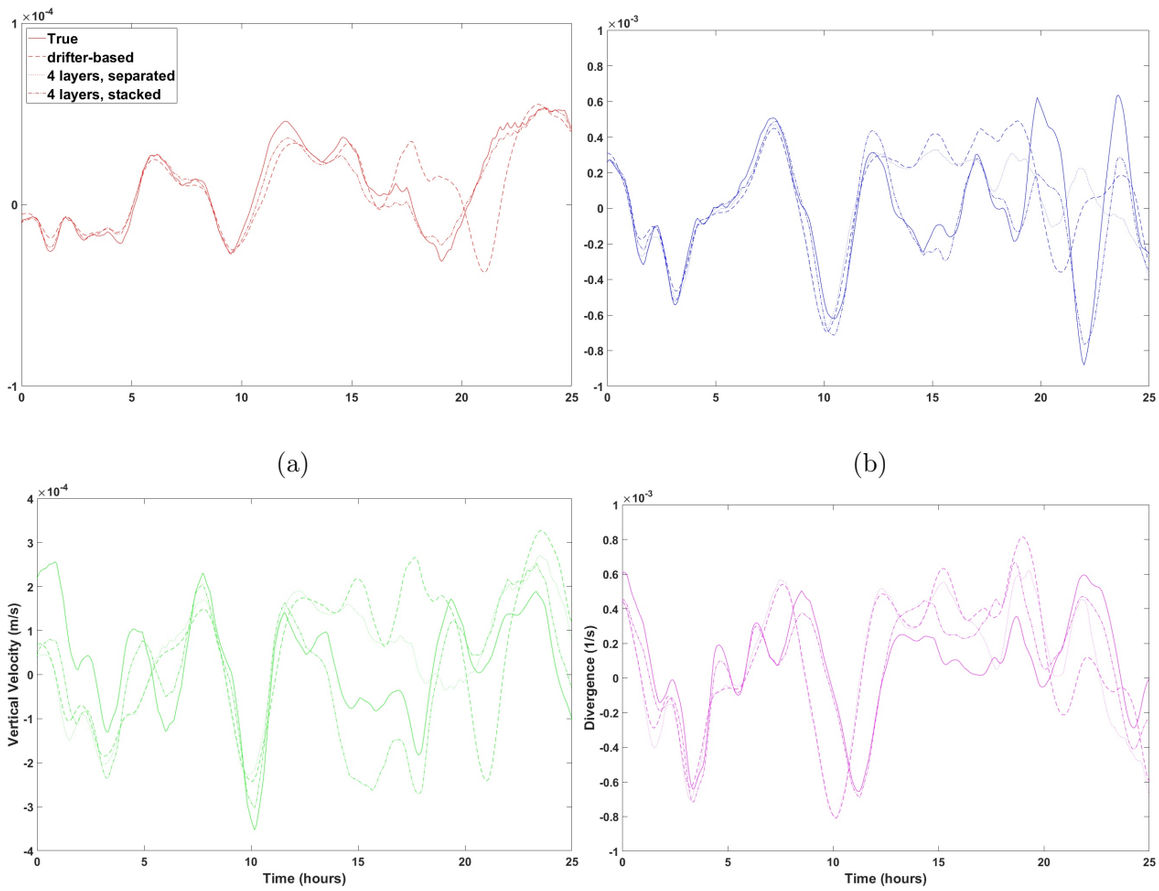

Figure 1-12: At 4 depths, comparison between the Eulerian model vertical velocity (solid) and vertical velocity estimated using drifter based methods according to the legend. "4 layers, laterally separated" and "4 layers, vertically stacked" refer to simulation where model divergence at 4 depths was used at the geographical locations corresponding to the center of mass of the 6 drifters at 4 depths, or at the same geographical location, respectively.

Much like the divergence balance terms computed for real drifters, βu in the model is significantly smaller in magnitude (10^{12} s^{-2}) than $\frac{D}{Dt}(\nabla_H \cdot \vec{u})$ and $f\omega^{(z)}$, which are $\mathcal{O}(10^{-8})$ s^{-2}. The range of variability for the $\frac{D}{Dt} div_h \vec{u}$ is several times smaller compared to real drifters, whereas the range of variability of $f\omega^{(z)}$ is similar to real drifters (so the distribution seen in Figure 1-13a are less elongated in the x-direction than those in Figure 1-4a). In the vorticity balance equation, the vortex stretching term and $\frac{D}{Dt}\omega^{(z)}$ are both 2-3 times smaller compared to real drifters. These two terms correlate slightly better in the model with correlation coefficients reaching up to 0.6.

FTLE values for simulated drifters are comparable (but slightly smaller) than those computed for real drifters. The contribution of vertical shear of horizontal velocity is significant but less dominant than for real drifters, likely due to the larger spread of simulated drifters within layers and smaller spread between layers.

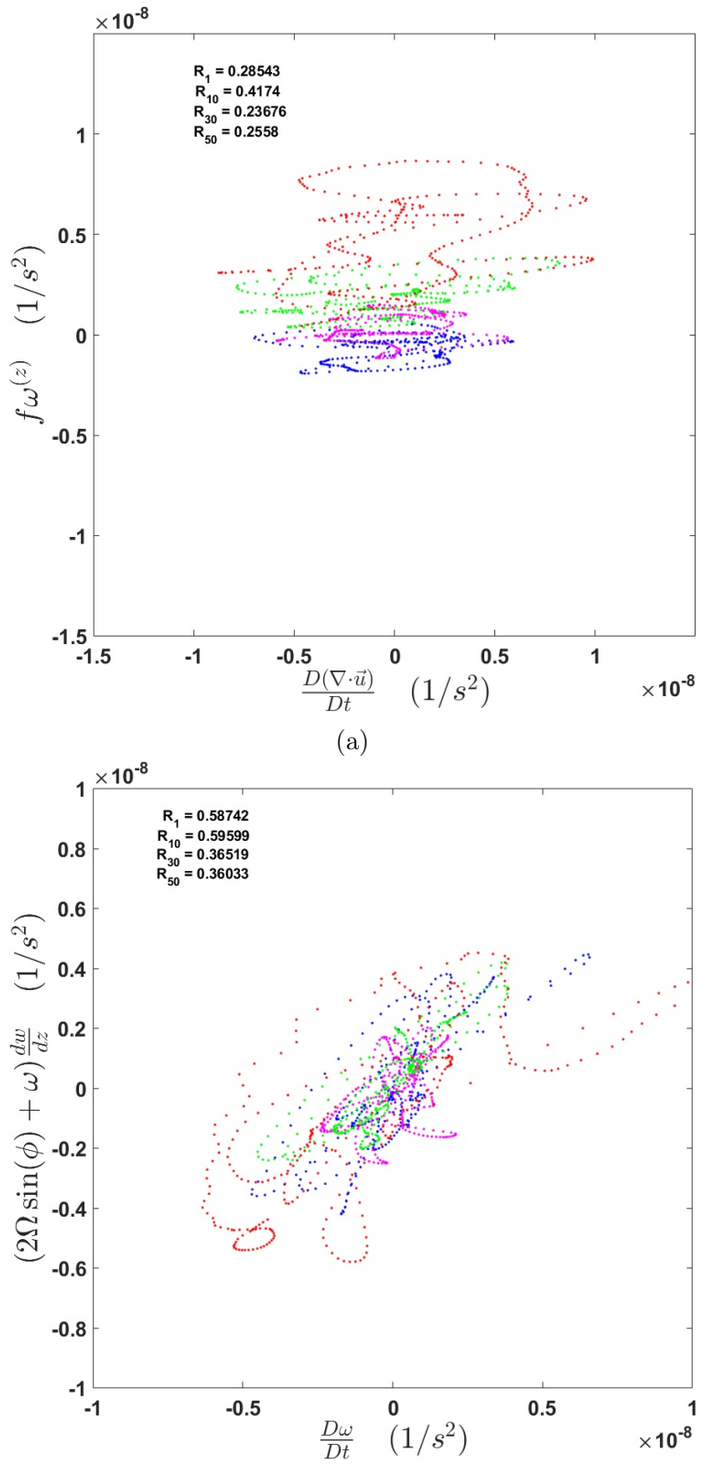

Figure 1-13: Same content as shown in Figure 1-4 but for simulated drifters released in SOCIB WMOP.

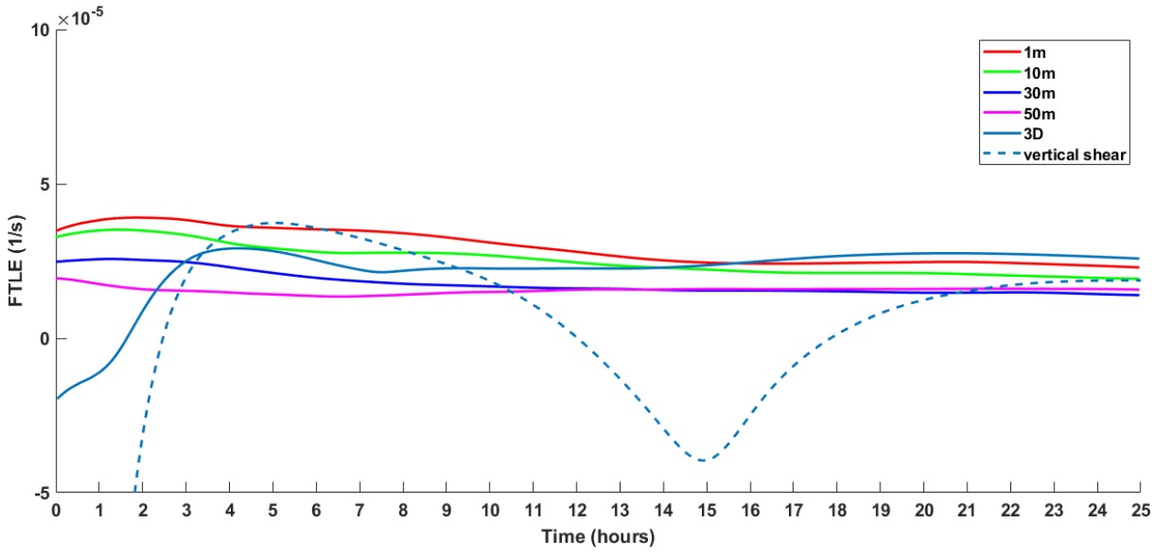

Figure 1-14: Same content as shown in Figure 1-5 but for simulated drifters released in SOCIB WMOP.

1.3.3 Analysis of the concurrent u-CTD and ADCP measurements

Data from simultaneous u-CTD and ship-based ADCP instruments from the drifter experiment, as well as satellite-based sea surface height (SSH) and inferred geostrophic velocities, will now be used to put the observed drifter behavior in terms of the general dynamics of the region at the time.

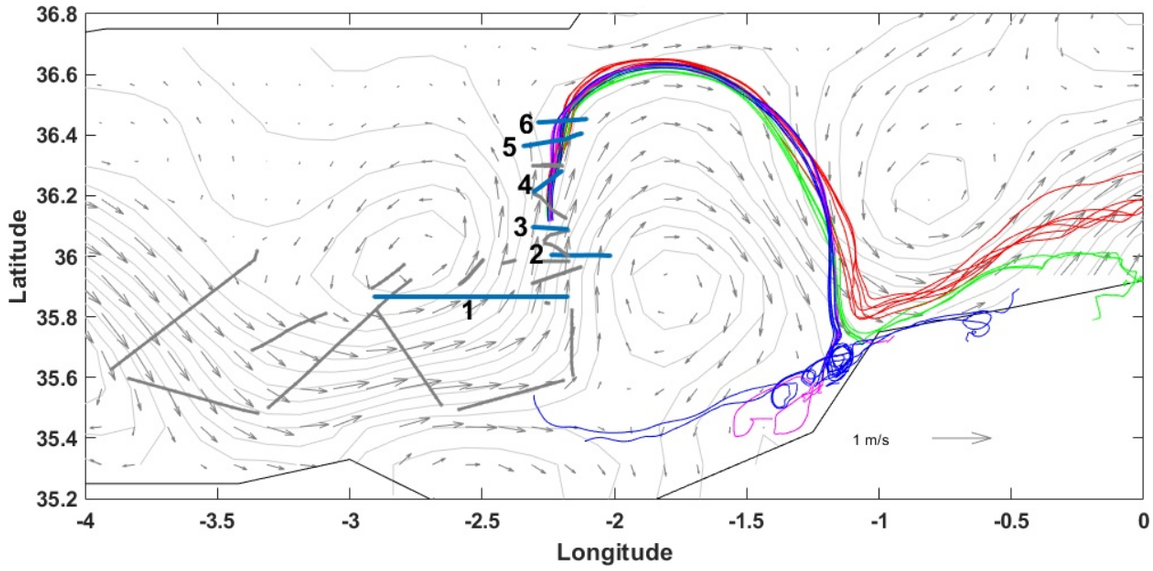

Figure 1-15: Satellite-based SSH contours (grey curves) and geostrophic currents (arrows), with the ship-based sections (thick grey and black lines) and multi-level drifter trajectories (colored curves) superimposed. The 6 sections that were used for our analysis are shown in black and are numbered 1 through 6, with the section number indicated next to the section. The grey sections located between sections 1 and 2, 2 and 3, 3 and 4, and 4 and 5 were qualitatively similar to their neighboring black sections and were omitted for brevity.

The satellite-based SSH and corresponding maxima of horizontal velocities reveal the surface-intensified jet along the edge of the Eastern Alboran Gyre (shown in Figure 1-15). The same maxima are seen in all of the ADCP sections taken before and after drifter deployment (Figure 1-18). Horizontal velocities estimated from drifters (shown by color in

Figure 1-18) are consistent with ADCP measurements and are also in general agreement with geostrophic velocities derived from SSH. Velocities within the jet reach a meridional velocity of around $\mathcal{O}(1$ m/s) close to the surface and go down to about 150 m. Uniform densities can be seen in the upper 25 m of u-CTD sections and sloping isopycnals exist between 25 m and 150 m and are located in the same lateral position as the jet. Therefore the two shallower drifter layers (1 m and 10 m) were within the mixed layer, while the bottom two layers (30 m and 50 m) were below the mixed layer. The zonal extent of the front is on the order of $\mathcal{O}(20$ km), which is much larger than the initial size of drifter polygons ($\sim$ 2 km diameter). All sections reveal qualitatively similar water column structure in the water column. Density near the front is mostly controlled by salinity below the mixed layer ($\sim$ 25 m), but temperature dominates density above 25 m and is not negligible at depth, as seen in Figure 1-17. The density difference on opposite sides of the front at around 50-100 m is around 1 kg/m^3, compared to a density difference of 1.5 kg/m^3 near stronger Almería-Oran front. As seen in sections 4 through 6, the shallower drifters layers crossed the sections increasingly further east from the deeper layers, suggesting that drifters in the top layers were advected downstream towards the center of the jet while the deeper drifters did not. This observation is consistent with the existence of secondary ageostrophic currents with cross-front velocities at the surface and subduction on the denser side of the front (Hoskins, 1982). On the less dense side of the front, upwelling is expected, but drifters appear to have not reached depths deep enough to observe these effects. The behavior of drifters in the top layers suggests that they may have been pushed to the anticyclonic side of the jet while they headed north, whereas deeper drifters stayed on the cyclonic side. This can be seen in the time-series of drifter-based vorticity estimates, which shows positive vorticity in all layers at the time of deployment, but when crossing section 6 (12-15 hours), vorticity in the top layers became negative while vorticity in the bottom layers remained positive (shown in Figure 1-16).

As mentioned in section 1.2.3, it was hypothesized that the least-squares method including time could be used to estimate time derivatives of u and v in addition to the spatial derivatives. This method was tested in the 400 m SOCIB WMOP model using 6 "stations" of measurements with space and time intervals roughly corresponding to those of the vessel which took measurements during the drifter experiment. An RMS error analysis of the estimates was conducted to determine whether using the method for real data could be useful. In the real experiment, the vessel transits fin the east/west direction for some time to survey one "section," and then heads north or south to begin another section. To simulate this, the 6 stations of in the error analysis consisted of two arrays of 3 stations. The two arrays are

separated by $\Delta y = \Delta x$, and consecutive stations in an array are separated by Δx. Measurements begin in the furthest southwest station and are taken at intervals of Δt in the counter clockwise station, so that the final station in time is the one in the northwest corner. Δx and Δt were varied, and then the least-squares algorithm was used to compute derivatives of u at 150 locations in the 400 m resolution domain. Both the modified LLS method with time and the traditional LLS method were used. RMS errors between the estimates and the "true" Eulerian values were computed for the ensemble of 150 locations. True Eulerian values are computed at the spatiotemporal mean at each set of 6 measurements.

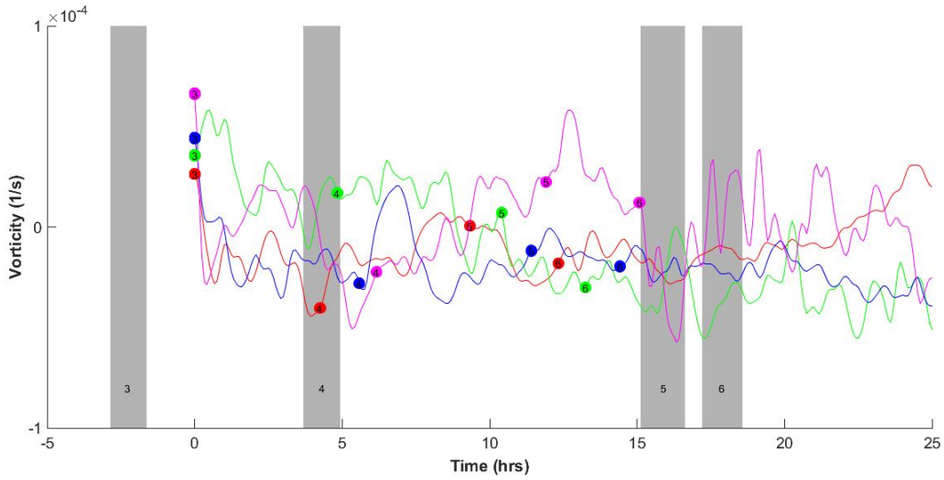

Figure 1-16: Drifter based estimates of vorticity at all depths, color coded such as in Figure 1-1. Grey shaded regions correspond to the time interval when each section was taken (section s are labeled at the bottom of the graph) and colored dots correspond to the times the center of mass of drifters in each layer passed the section.

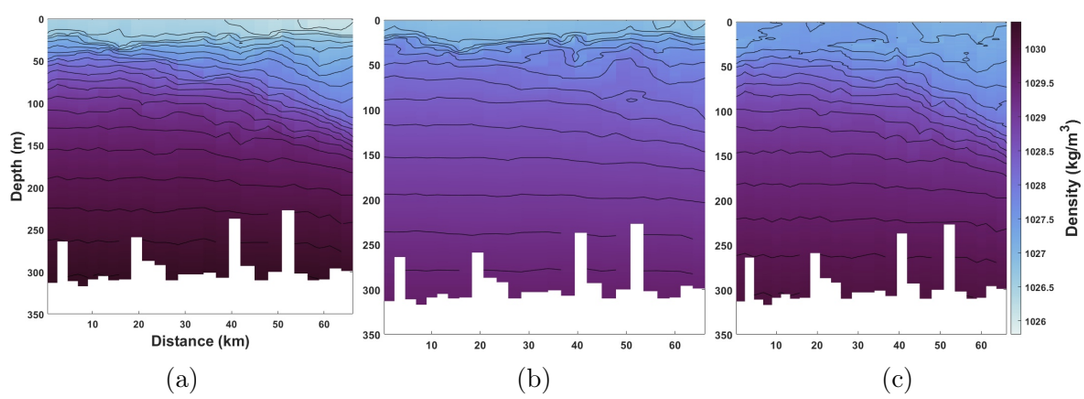

(a) (b) (c)

Figure 1-17: Density for section 1, computed using (a) CTD data for both temperature and salinity, (b) temperature but with fixed salinity, and (c) salinity but with fixed temperature.

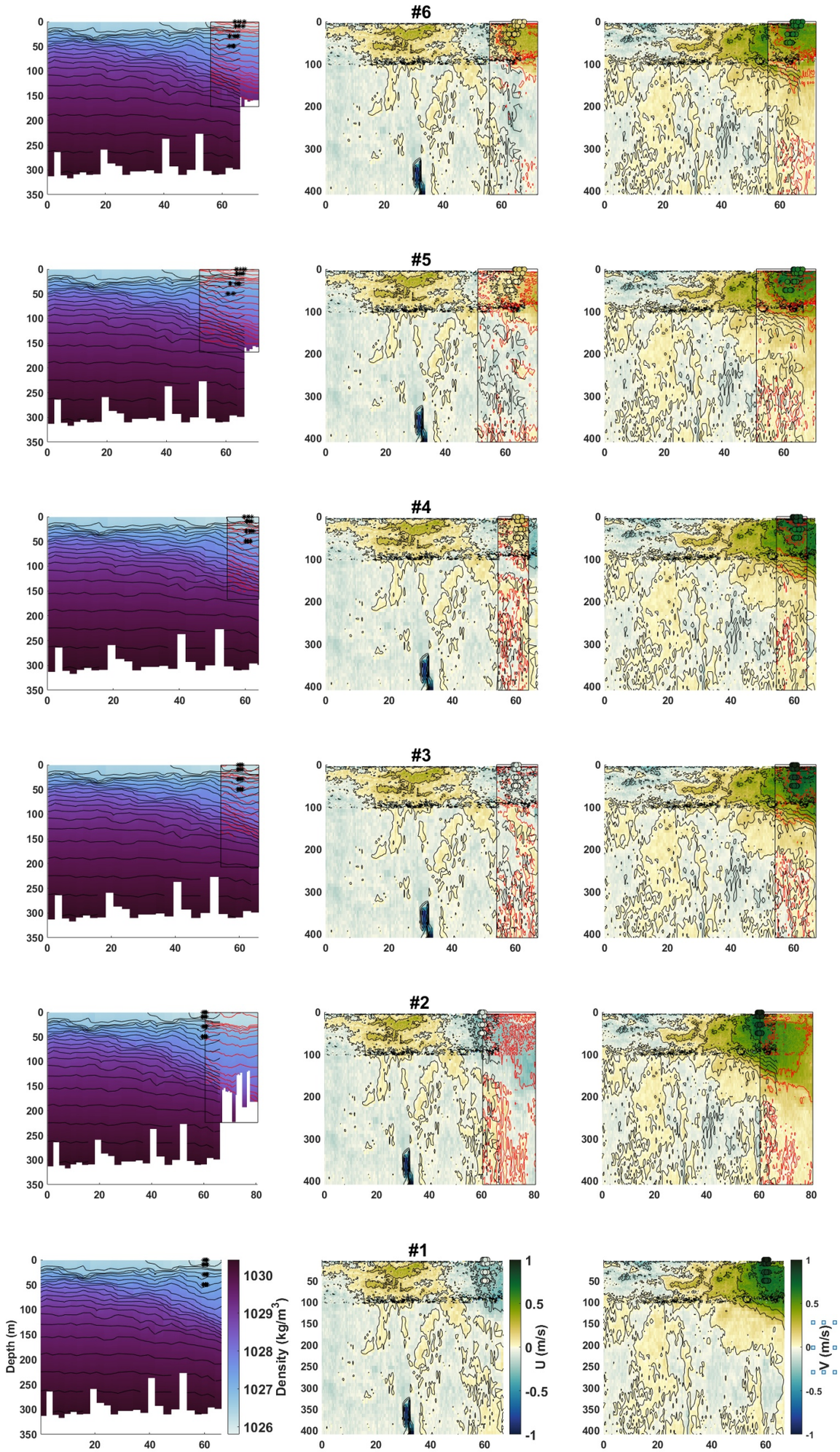

(a)

Figure 1-18: For sections 1 (bottom) through 6 (top), profiles of density (left) and zonal (middle) and meridional (right) currents. All sections (black rectangles) are superimposed on section 1. Red curves in the left panels correspond to sections 2 through 6 as labeled above each panel. Drifters are shown by circles, color-coded by zonal or meridional velocity, corresponding to the panel they are in.

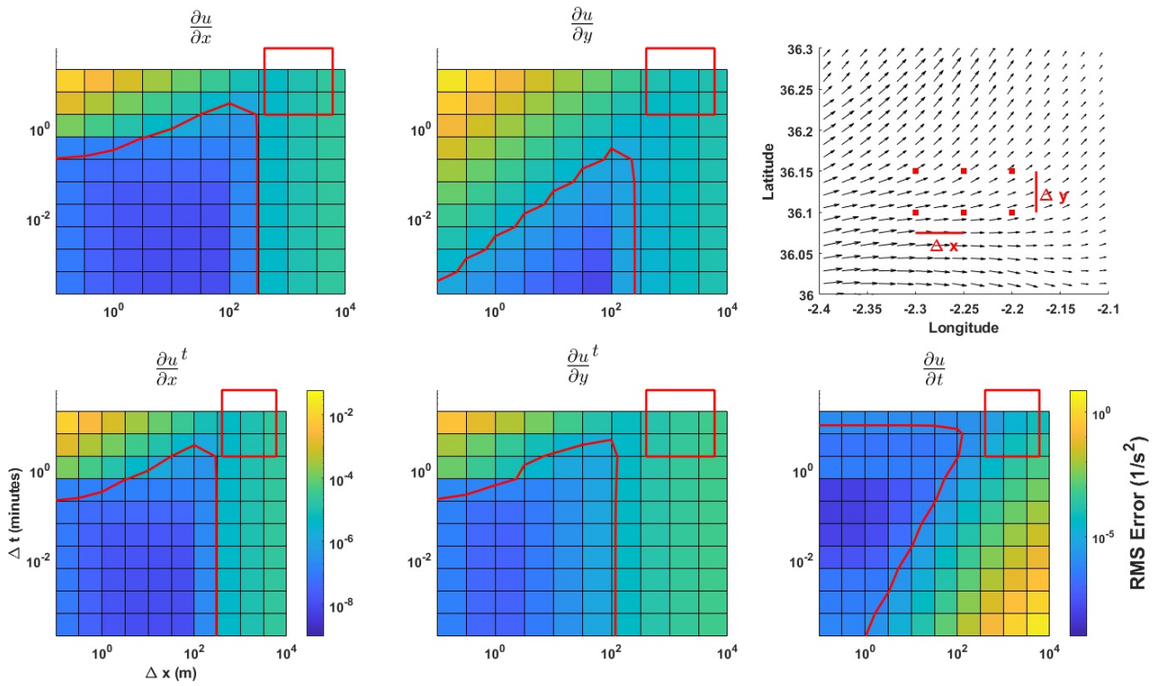

Figure 1-19: Error analysis for testing of the LLS method of estimating gradients, for a simulation involving two arrays of 3 stations. The top left and top middle panels correspond to the LLS method that does not include time (so all measurements are considered to be taken instantaneously). The bottom three panels correspond to the LLS method including time such as in Equation 1.6. The red box corresponds to the regime in which the vessel from the CALYPSO experiment operates, with sampling intervals of about 2 minutes and 400 meters (represented by the bottom and left edges of the square), and with sections being measured at roughly 1 hour and 5 km apart (represented by right and top edges of the square). The top right panel shows velocity fields from the 400 m SOCIB WMOP model, with one example of the simulation layout.

Results indicate that estimates within realistic regimes of Δx and Δt always lead to errors of greater than 20% of the magnitude of their respective Eulerian values. For this reason, further estimates of gradients along ADCP sections was not conducted. However, this analysis was done for a particular setup in which a single simulated ship transits along consecutive sections. Future studies may use more sources of data (such as multiple ships) that are distributed less sparsely in both time and space.

1.4 Discussion

In this chapter, estimates of divergence, vorticity, vertical velocity, and finite-time Lyapunov exponents (FTLEs) were analyzed based on measurements from drifters drogued at 1 m, 10 m, 30 m, and 50 m. Multi-layer drifters such as those used in the experiment provide a unique advantage over traditional drifters in their ability to characterize flows in three dimensions, including the processes which govern vertical transport of physical and biogeochemical material between ocean layers. The experiment was conducted near a strong front, where these vertical transport processes are expected to be much stronger compared to other regions of the ocean.

Divergence and vorticity estimations were O(f) during the 25 hour period of analysis, and different methods for estimating divergence and vorticity generally agreed well with each other. Using the bootstrapping method for computing standard deviation from 6 sets of 5 drifters in each layer, STD was estimated to be less than 10% of the temporal-mean absolute value for both divergence and vorticity. Errors in these estimations could be due to errors in the LLS method, shape/size of the polygon spanned by drifters, and due to actual spatial variations of velocity gradients. Vertical velocity estimates, computed by integrating divergence estimates downward, were O(1 mm/s) during the experiment. These estimates from real drifters are several times larger than those computed in the 400 m SOCIB WMOP model of the Alboran Sea. Vertical velocities estimated from real drifters were also generally positive (indicating upwelling), with a few instances of negative velocities (indicating downwelling). At some times during the experiment, w estimates changed signs between layers, meaning that surface divergence may not be a good indicator of deep downwelling. Vertical velocity estimates also generally agreed with measurements from a 3D Lagrangian float released at a nearby time and location (Tarry et al., 2021).

Two methods were used to understand the observed splitting between the two top and bottom two layers of drifters. The first method was to estimate horizontal displacement caused by Ekman currents by computing wind stress using the bulk flux algorithms found in (Edson et al., 2013). This analysis found that after 3 days, the total estimated zonal displacement of the 1 m layer due to Ekman currents was around 6 km. The real displacement between the 1 m and 30/50 m layers is closer to around 10-15km, however a 6 km displacement may have been sufficient to push the upper drifters outside of the gyre and into the Eastward-flowing jet. The second method to evaluate this separation was to use the 400 m resolution model to gain insight. This was possible since both real and simulated drifters exhibited similar behavior. Results from the model suggested that Ekman currents contributed to the splitting between the top and bottom layers by pushing the top two layers of drifters eastward out of the Eastern Alboran Gyre over the first several days after deployment.

To investigate sources of error in drifter-based methods, estimates of divergence, vorticity, and vertical velocity from simulated drifters were compared to "true" Eulerian model values. LLS estimates of divergence and vorticity generally agreed well, with high correlation coefficients. One exception was in the 1 m layer at around hour 15, when the drifter polygon was particularly elongated. Errors in vertical velocity estimates were shown to come primarily

from separation of drifter layers from one another. Some error was also due to the sparsity of drifter layers (i.e. four layers rather than a dense set of layers), and a much smaller amount of error was due to errors in the LLS estimates themselves.

The plausibility of estimating velocity gradients from underway ADCP data was also analyzed, but was shown to be impractical through error analysis of simulated shipboard measurements in the 400 m SOCIB WMOP model. The accuracy of this method is primarily affected by the temporal and spatial distribution of measurements. Specifically, measurements from a single vessel as it transits to parallel sections does not provide adequate temporal coverage in order to accurately estimate gradients. Future work might involve shipboard data from multiple vessels, allowing for measurements that are well-distributed in time and space.

Drifter-based estimates of divergence and vorticity were also used to estimate terms from the vorticity and divergence equations. The time-rate-of-change of vertical vorticity following trajectories was estimated to be the same order of magnitude as the vortex stretching term, though these two terms did not correlate well in time. This indicates that vortex stretching is a significant contributor, but not the only significant contributor, to the evolution of vorticity. In the divergence equation, the term $f\omega^{(z)}$ was estimated to be of similar magnitude to the time-rate-of-change of horizontal divergence following trajectories, but $f\omega^{(z)}$ was 2-3 times larger. All other terms in the vorticity and divergence equations require horizontal gradients of vertical velocity, pressure, or density. These terms cannot be estimated from data from this drifter experiment, and are not easily estimated in general without simultaneous measurements of the relevant quantities throughout the domain. Estimating the remainder of the terms of the divergence and vorticity equations was also attempted in the 400 m SOCIB WMOP model, but these computations were difficult and results were not shown. Completing these balances requires vertical gradients of horizontal velocities, and the fields required to compute these gradients were not always readily available. Further, numerical models often use various advection schemes that make horizontal advection terms challenging to compute for end users.

Lagrangian drifter data gives the unique advantage of the ability to compute diagnostics that identify Lagrangian coherent structures, such as FTLEs. 2D and 3D FTLEs were computed in this chapter to demonstrate their use in multi-layer drifter experiments. Ridges in FTLE fields correspond to stable and unstable manifolds of hyperbolic trajectories. While such variations in the field cannot be ascertained through this experiment, the framework

for their estimation was shown to be effective and could be expanded upon in subsequent work. Future experiments might involve more densely populated arrays in the vertical or horizontal directions.

Chapter 2

Applying Dynamical Systems Techniques to Real Drifters

2.1 Introduction

In the past several decades, the dynamical systems approach to Lagrangian transport has been applied to a variety of problems in physical oceanography such as transport and mixing in oceanic flows (Wiggins, 2005; Rypina and Pratt, 2017; Mendoza and Mancho, 2010). These techniques attempt to identify coherent regions of flow fields often called Lagrangian coherent structures (LCS) which categorize the flow into regions of distinct behavior. Mathematically, LCSs often correspond to features such as stable and unstable manifolds, KAM stable tori, and other clusters of distinct behavior (Haller, 2002; Shadden et al., 2005; Wiggins, 2005; Huntley et al., 2015; Haller, 2015).

In April 2018, several hundred drifters were released as part of the Submesoscale Processes and Lagrangian Analysis on the Shelf (SPLASH) experiment in the northern Gulf of Mexico. One subset of 135 of these drifters were released on April 21 in a diamond-shaped formation with nearly regular spacing. Drifters were placed approximately 1km apart and consisted of roughly 11 rows in the northwest-southeast direction and 12 rows in the northeast-southwest direction.

This relatively gridded set of trajectories provides a unique opportunity to quantify Lagrangian Coherent Structures in a real ocean environment. This is possible since LCS metrics rely exclusively on information from Lagrangian trajectories such as ocean drifters. While FTLEs were computed in Chapter 1 for real drifters in the Alboran Sea, the FTLE values were not able to be studied in the context of coherent structures, since the locations of FTLE estimates were too few and sparse. In this chapter, FTLEs and other similar tools including

trajectory arc-length, correlation dimension, Lagrangian-averaged vorticity deviation, dilation, and spectral clustering are computed for the dense set of drifters in the Gulf of Mexico, allowing us to compare variations in their fields.

2.2 Methods

2.2.1 Finite-time Lyapunov Exponents

Finite-time Lyapunov exponents were explained briefly in Section 1.2.6. In this section, slightly more detail will be given to the computation of FTLEs in regular mesh grids. To constructs FTLEs, the right Cauchy-Green deformation tensor is computed for an initial condition and a grid of its neighboring points. The Cauchy-Green deformation tensor, for two dimensional flows, is a 2×2 matrix which measures local stretching between points, and is constructed as in Equation (2.1):

$$G = \left(\frac{\Delta \vec{x}_{ij}}{\Delta \vec{x}_{0,ij}} \right)^T \left(\frac{\Delta \vec{x}_{ij}}{\Delta \vec{x}_{0,ij}} \right) \ , \tag{2.1}$$

where we compute $\frac{\Delta x_{ij}}{\Delta x_{0,ij}}$ in the finite-difference form such as in Equation (2.2):

$$\frac{\Delta \vec{x}_{ij}}{\Delta \vec{x}_{0,ij}} = \begin{pmatrix} \frac{x_{i+1,j}(t+\tau) - x_{i-1,j}(t+\tau)}{x_{i+1,j}(t) - x_{i-1,j}(t)} & \frac{x_{i,j+1}(t+\tau) - x_{i,j-1}(t+\tau)}{y_{i,j+1}(t) - y_{i,j-1}(t)} \\ \\ \frac{y_{i+1,j}(t+\tau) - y_{i-1,j}(t+\tau)}{x_{i+1,j}(t) - x_{i-1,j}(t)} & \frac{y_{i,j+1}(t+\tau) - y_{i,j-1}(t+\tau)}{y_{i,j+1}(t) - y_{i,j-1}(t)} \end{pmatrix} \ , \tag{2.2}$$

where $x_{i,j}(t)$ indicates the x-location of the particle in grid position i, j at time t, etc. The FTLE is considered a "forward" FTLE when τ is positive and a "backward" FTLE when τ is negative.

We can then compute the FTLE of a trajectory using

$$\lambda(\vec{x}_0, t_0, \tau) = \frac{1}{|\tau|} \ln \sqrt{\sigma} \ , \tag{2.3}$$

where σ is the maximum eigenvalue of the deformation tensor, G. This process is repeated for each point on a grid of initial conditions to construct an FTLE field.

FTLEs were computed using two different methods for drifters in order to create a densely populated FTLE field. The first method is the unstructured grid method from Lekien and Ross (2010) which was also described in section 1.2.6. For this method, the Delaunay triangulation algorithm was used to define drifter neighbors. This algorithm maximizes the minimum angle in the triangulation, in order to avoid thinly stretched "sliver" triangles.

The method performs well at finding neighbors for drifters that sufficiently "surround" each center. Figure 2-1a shows each drifter and its neighbors for the unstructured grid method. All neighbors chosen by the triangulation algorithm are used, even when regardless of edge length.

The second method used to compute FTLEs for drifters was the typical differencing method for regular grids described by Equations 2.1-2.3. For this method, FTLE values were defined at the center of sets of four drifters that formed nearly orthogonal axes (i.e. two drifters define the "x" axis and two other drifters define the "y" axis). These sets of drifters were chosen manually, and since their edges are never perfectly aligned with the x-y coordinate system, all sets of four drifters were rotated into a new coordinate frame, defined by the mean angle of rotation of their edges with respect to the x or y axes in the coordinate system. Figure 2-1b shows each chosen center connected to its chosen neighbors. The "center" is defined as the intersection between the lines connecting drifter pairs.

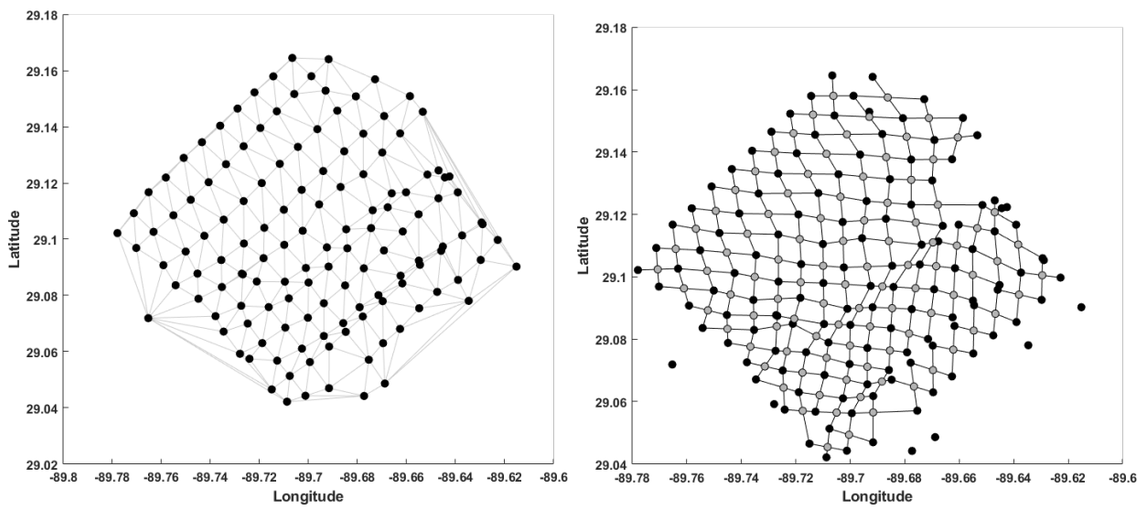

(a) (b)

Figure 2-1: Locations of FTLE estimates for real drifters. Panel (a) contains only drifter locations as black dots, with grey edges representing the connections between neighboring trajectories used in the unstructured grid FTLE method. These edges are determined by the Delaunay triangulation algorithm, and all edges are used in the computation. Panel (b) shows drifter locations again as black dots, but also shows grey dots representing the centers of FTLE estimates, for which connected drifters define axes in the computation. These edges were chosen manually.

2.2.2 Arc-Length

The method of trajectory arc-lengths fall into a category of methods often named "Lagrangian Descriptors" in literature, which are used to quantify stable and unstable manifolds and KAM tori of flow fields Mendoza and Mancho (2010) Mancho et al. (2013) Lopesino et al. (2017). It is typically written as an integral in both forward and backward time, but since only forward-time trajectories can be ascertained from the drifter experiment, we use a

definition written only in forward-time:

$$M(\vec{x}_0, t_0, \tau) = \int_{t_0}^{t_0+\tau} ||\vec{u}(\vec{x}(\vec{x}_0, t))||\ dt\ . \tag{2.4}$$

Arc-length fields in forward time can reveal stable manifolds of hyperbolic trajectories . For drifter trajectories, this metric is easy to compute since only drifter positions are needed.

2.2.3 Trajectory Complexity (Correlation Dimension)

The concept of trajectory complexity was introduced by Rypina et al. (2011) where different regions of the flow domain are parititoned into regions of different complexity levels. The method was shown to reveal structures revealing LCSs such as stable and unstable manifolds. Correlation dimension and ergodicity defect were proposed as two metrics of trajectory complexity. Here we use the correlation dimension, which first involves mapping the set of trajectories onto a unit square. Then, a distribution function is computed as

$$F(s) = \frac{1}{N^2}\left[N_j(s)\right]^2\ , \tag{2.5}$$

where N is the number of trajectories, and N_j is the number of trajectories that lie inside of the j^{th} element with edge length $s = 2^{-m}$ for $m = 0, 1, ...M$. The correlation dimension c can then be computed as the slope of $F(s)$ vs s in log-log coordinates for small s and large N. This method can be applied identically to drifters as well as dense regular grids of trajectories.

2.2.4 Encounter Number

The concept of encounter volume (or encounter number) was introduced by Rypina and Pratt (2017) as a diagnostic for measuring mixing potential in fluid flows, and its connection to diffusivity was shown in Rypina et al. (2018). It measures the "amount" of fluid in a domain encountered by a fluid element, within some radius R of the parcel. These fields also reveal LCS structures such as stable manifolds, since stable manifolds act as pathways that bring fluid from remote regions of the domain into regions near hyperbolic trajectories, where many encounters occur with other fluid elements. The encounter number can be written as

$$EN(\vec{x}_0, t_0, \tau) = \sum_{k=1}^{K} I(min(|\vec{x}_k(\vec{x}_{0k}, t_0, \tau) - \vec{x}(\vec{x}_0, t_0, \tau)| \leq R)\ , \tag{2.6}$$

where the indicator function I is 1 if true and 0 if false, and K is the total number of

Lagrangian parcels released. The encounter volume can then be computed as $V \approx N\delta V$ where δV represents the approximate volume of a fluid element (determined by the grid spacing of initial positions). This method can be applied identically for both drifters and dense grids. Since approximation δV may not be constant for trajectories that do not begin perfectly gridded, a different δV could be used for each trajecotry. For simplicity, this paper shows results of encounter number only for drifter estimates.

2.2.5 Vorticity and Divergence

Vorticity and divergence estimate were computed using the same LLS method described in Section 1.2.3, however instead of using a fixed set of drifters at each time, divergence and vorticity "neighbors" are chosen instantaneously depending on the distance and distribution of surrounding drifters. 6 neighbors within 3km were always used to estimate gradients in all cases. A criteria was set that the nearest 6 drifters must create a polygon with an aspect ratio of less than 6 (where aspect ratio is defined such as in Section 1.2.5), and that the "center" drifter must be instantaneously within a polygon formed by the 6 drifters. The "in polygon" requirement ensures that there is a sufficient distribution of neighbors around the center drifter in all directions, and also ensures that the center of mass of the distribution (the location where gradients are being estimated) is somewhere near the center drifter itself. Divergence and vorticity values are thus taken to be at the drifter location, despite that the actual center of mass might be at a location that is slightly shifted spatially. Drifters which had 6 neighbors within 3km that do not fit the aspect ratio and "in polygon" requirements are considered to fit the less-restrictive criteria.

2.2.6 Dilation

Dilation was proposed by Huntley et al. (2015) as a method for identifying "clusters" of material at the ocean surface. It is computed as the time-averaged divergence experienced by a particle along its trajectory,

$$\Delta(\vec{x}_0, t_0, \tau) = \frac{1}{\tau} \int_{t_0}^{t_0+\tau} \nabla \cdot [\vec{u}(\vec{x}(\vec{x}_0, t))]\, dt \ , \tag{2.7}$$

or discretely,

$$\Delta_i^\tau = \frac{\Delta t}{N} \sum_{n=1}^{N} (\nabla \cdot \vec{u})_i^n \ , \tag{2.8}$$

where i corresponds to the i-th trajectory and n is the time step.

For drifters, divergence is computed in the least-squares sense as described in Sections 1.2.3 and 2.2.5. When drifters went for short periods of time (less than 1 hour) without fitting the requirements for estimating divergence as described in Section 2.2.5, divergence values were linearly interpreted between available estimates. When gaps in availability of divergence estimates lasted for longer than 1 hour, drifter dilation values are not computed for all future times.

2.2.7 Lagrangian-Averaged Vorticity Deviation

Lagrangian-averaged vorticity deviation (LAVD) is a method introduced by Haller et al. (2016) to identify Lagrangian vortices (rotationally coherent LCSs). They show that these rotational LCSs are defined by tubular level surfaces of LAVD fields along singular maximal level surfaces. The LAVD is defined as

$$\mathrm{LAVD}(\vec{x}_0, t_0, \tau) = \frac{1}{\tau}\int_{t_0}^{t_0+\tau} |\omega(\vec{x}(\vec{x}_0, t)) - \bar{\omega}(t)|dt \ , \tag{2.9}$$

where $\omega(\vec{x}(t))$ is the instantaneous vorticity of a parcel with initial position x_0 at time t, and $\bar{\omega}$ is the instantaneous spatial mean of the vorticity ω within the domain. The factor $\frac{1}{\tau}$ in front of the integral is trivial and is not usually included in litereature, since it is a constant which multiplies all LAVD values in a field (we are interested not in specific LAVD values of trajectories but rather the comparison between all trajectories in the field), but we have included it here to remain consistent with the definition of dilation such as in Equation 2.8 and to keep the range of LAVD values somewhat simialar between time frames.

For drifter trajectories, we use vorticity values computed using the least-squares formula and criteria described in Sections 1.2.3 and 2.2.5 and discretely sum:

$$\mathrm{LAVD}_i^{\tau} = \frac{\Delta t}{N}\sum_{n=1}^{N} |\omega_i^n - \bar{\omega}| \ . \tag{2.10}$$

As with dilation, when drifters went for short periods of time (less than 1 hour) without fitting the requirements for estimating vorticity as described in Section 2.2.5, vorticity values were linearly interpreted between available estimates. When these gaps lasted for longer than 1 hour, drifter LAVD values are not computed for all future times.

2.2.8 Spectral Clustering of Trajectories

Spectral clustering is a technique described in reviews such as von Luxburg (2007) and Shi and Malik (2000), which is based on the minimization problem which separates graph nodes into disjoint sets. The method has been more recently adapted for LCS detection in geophysical flows Froyland and Padberg-Gehle (2015) Hadjighasem et al. (2016) Vieira and Allshouse (2020). We follow an optimized-parameter adaption of the method described by Filippi et al. (2021).

The spectral clustering method begins with a matrix consisting of the time-average distance between trajectories, written as

$$r_{ij} = \frac{1}{\tau} \int_{t_0}^{\tau} |x_i(t) - x_j(t)| dt \ , \tag{2.11}$$

where the vertical brackets correspond to the Euclidean norm and i, j are indices corresponding to each drifter trajectory. Then the weights matrix is

$$w_{ij} = \begin{cases} 1/r_{ij}, & \forall i \neq j \\ \text{constant offset} w_{ij} = const, & i = j. \end{cases} \ . \tag{2.12}$$

Next, the sparsification radius r is chosen, and W is sparsified by removing all weights where

$$w_{ij} \leq 1/r \ . \tag{2.13}$$

Next, the diagonal degrees matrix D is computed such that $d_{ii} = \sum_{j=1}^{N} w_{ij}$ (i.e. a sum over the i-th row or column). The graph Laplacian $L = D - W$ can then be formed, and the eigenvectors and eigenvalues of the generalized eigenvalue problem $L\vec{v} = \lambda D\vec{v}$ can be solved. Equivalently, a simple eigenvalue problem of $L_N\vec{v} = \vec{v}$ can be solved, where L_N is the normalized graph Laplacian defined as

$$L_N = D^{-1/2} L D^{-1/2} \ . \tag{2.14}$$

Once the eigenvalues and eigenvectors have been solved for, the number of eigenvalues

k_{gap} before the spectral eigengap (i.e. the largest gap between ascending eigenvalues of L_N) is determined, and the first k_{gap} eigenvectors are sorted into $k_{gap}+1$ clusters using the K-means algorithm. The output of K-means is an $N \times 1$ vector that assigns a cluster index to each trajectory.

The selection of the sparsification radius r is typically determined by the user depending on each problem, but Filippi et al. (2021) have described an algorithm which detects optimal values. They define optimal r as local maxima of the normalized spectral eigengap for varying r, where the normalized eigengap is defined as

$$\text{Normalized eigengap} = \frac{|\text{maximum eigengap}|}{\lambda_{max} - \lambda_{min}} \ , \tag{2.15}$$

where λ_{max} and λ_{min} are the maximum and minimum eigenvalues of L_N for a given r. Local peaks in the normalized eigengap vs. r determine optimal r values which result in clusters with higher intra-cluster similarity and lower inter-cluster similarity compared to r values that are locally smaller or larger. Some distributions of the normalized eigengap have multiple peaks for varying r. In these cases, results for r corresponding to all local maxima are used.

The offset constant, w_{ii} is another typically user-determined parameter that must be chosen somewhat carefully. w should be substantially higher than off-diagonal elements of W, but excessively large offsets lead to numerical errors due to the limits of double-precision (Hadjighasem et al., 2016; Filippi et al., 2021). Filippi et al. (2021) suggest choosing a value of the form:

$$\max(w_{ij}) \times 10^n \ , \tag{2.16}$$

with integer n, where n is the smallest value at which convergence is reached in the normalized spectral eigengap for a given r. For results in this chapter, an offset with $n = 7$ was chosen for all cases.

Spectral clustering results from densely gridded trajectories are not shown in this Chapter due to the computational costs, but may be included in future work. The ability of spectral clustering techniques to reveal Lagrangian coherent structures has been shown in papers such as Hadjighasem et al. (2016) and Filippi et al. (2021).

2.2.9 NCOM Forecasts during SPLASH

Forecasts from the Navy Coastal Ocean Model (NCOM) during the SPLASH experiment in the northern Gulf of Mexico were used to produce simulated drifter trajectories and high-resolution fields of all LCS metrics. The model seems to reproduce the main qualitative features of the circulation in the region, such as the various cyclonic and anticyclonic submesoscale eddies and the strong transient density fronts formed by the confluence of the freshwater run off from the coast with the saltier waters from the Gulf of Mexico. However, the model cannot be expected to reproduce all of the small-scale details and the exact locations of these flow features, as well as the exact times when these were formed or when they disappeared. In particular, comparison between the model density fields and SPLASH drifters suggests that as the drifters approached the coast near day 1 after deployment, they aligned along one such density front which then carried them into the Gulf as it moved offshore during the subsequent few days. Despite this favorable general comparison between the real drifters and the model surface density fields, the simulated drifters released at the time and locations of the real drifters head too much north after deployment and miss the front. If we shift the release locations of simulated drifters to the southeast, then they exhibit the same qualitative behavior as the real drifters. So we decided to analyze the simulated drifters released at the shifted location (instead of those released at the same release locations as real drifters). More specifically, the exact shifted release locations were determined by back-tracking from the locations of the real drifters on days 1-2 (when they were near the front that seems to strongly influence their motion) back to day 0. The center of the shifted location is about 17 km to the southeast of real drifter start locations. The new simulated drifter trajectories behaved similarly to real drifter trajectories, by splitting into northward-moving and southward-moving trajectories as they approached the coast, then aligning with the front, and eventually moving westward towards the center of the domain. The new simulated trajectories took slightly longer time than real drifters to reach the coast and align with the front. For this reason, slightly later times (t = 0.5, 2, and 4 days) are displayed in results for simulated drifters compared to slightly earlier times (t = 0.5, 1, and 3 days) for real drifters.

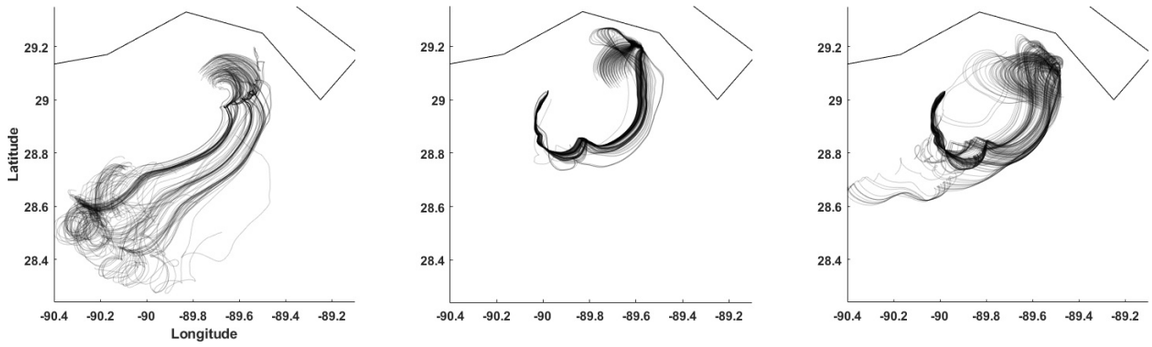

Figure 2-2: Spaghetti plots of trajectories from real drifters (left panel), trajectories from simulated drifters released at the same times and locations of real drifters (middle panel), and trajectories from simulated drifters released at the new chosen location (right panel). Trajectories are shown as black slightly transparent lines.

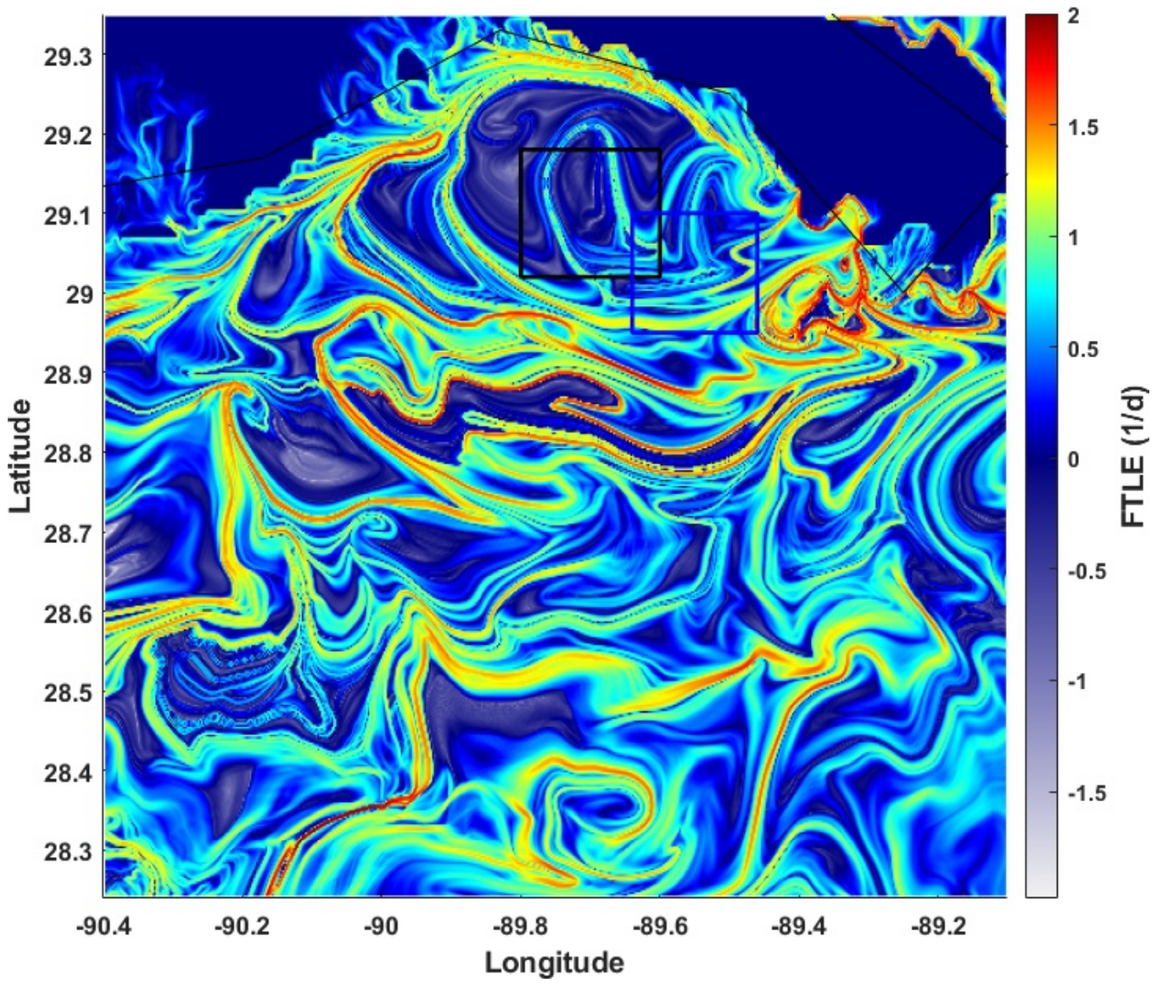

Figure 2-3: Forward FTLE snapshot at the release time of real drifters. The black box in the northern part of the domain represents the start location of real drifters. The blue box represents the chosen start location of simulated drifters. FTLE ridges are associated with stable manifolds, and ridges inside and surrounding the blue box align roughly with the backward-advected final locations of Figure 2-2.

2.3 Analysis of Real Drifter Results

In this section, results of FTLEs, arc-length, correlation dimension, encounter number, divergence, vorticity, dilation, LAVD, and spectral clustering are shown for estimates from real drifters (Figures 2-4 through 2-25). Results are shown for integration times $\tau = 0.5$, 1, and 3 days. With the exception of divergence and vorticity, all metrics should be viewed as functions of initial position alone (left columns) for interpreting LCSs, however, including final positions helps the viewer to visually see where trajectories near certain features appear at later times. Gaps in drifter position data were linearly interpolated so long as the gap did not exceed 6 hours. When gaps exceeded 6 hours, drifters are no longer included in the computation, leading to more sparsely occupied fields for later times.

2.3.1 Finite-time Lyapunov Exponents

Figures containing FTLE estimates for real drifters are shown below for integration times $\tau = 0.5$, 1, and 3 days. For $\tau = 0.5$ days in Figure 2-4, large FTLE values dominate the middle of the domain, separating drifters that initially begin in the north (which align with the coast and move northward) and those that begin in the south (which reach the coast slightly later and continue southward). Some convergence is also indicated in the southernmost corner of the domain by negative FTLE values. Drifters beginning in the northwest edge of the domain become the northward-moving drifters, which continue separating from each other. This separation within the group of northern drifters is indicated by high FTLE values for integration time $\tau = 1$ day as seen in Figure 2-5. Another convergence zone exists in the region where the southward-moving drifters begin meeting northward-moving drifters, as shown by the negative FTLEs in the northeast edge of the initial-positions domain for $\tau = 1$. As the drifters continue, a small convergence zone in the center of the domain leads to small and often negative FTLEs, effectively creating a dark blue "cluster" at $\tau = 3$ and beyond. The rest of the drifters after $\tau = 3$ produce relatively noisy results.

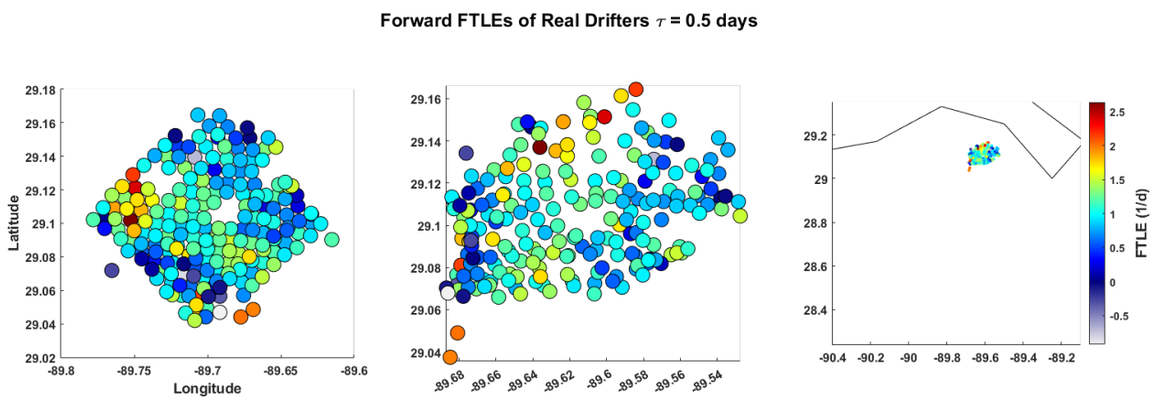

Figure 2-4: FTLE estimates for real drifters with $\tau = 0.5$. The left panel shows estimates as a function of initial position. Results in the middle and right panels are shown as a function of current position at the integration time.

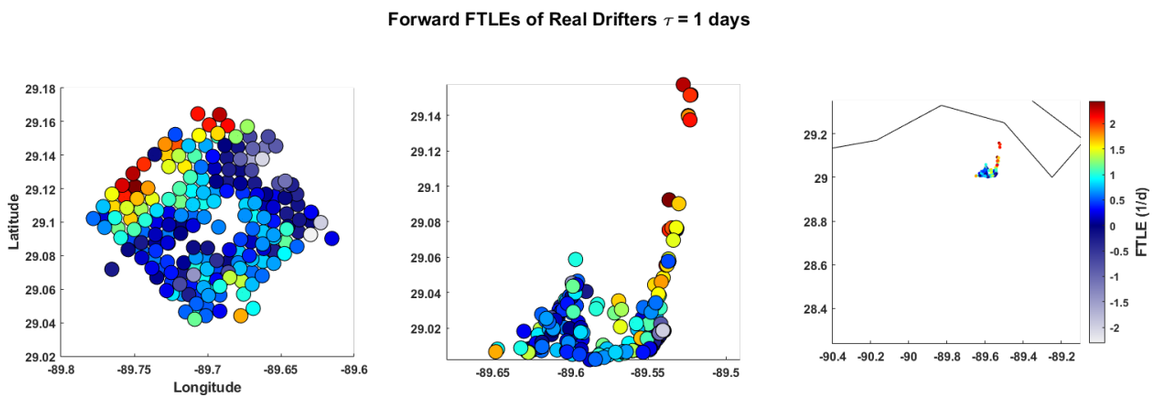

Figure 2-5: Same as Figure 2-4 except for $\tau = 1$ days.

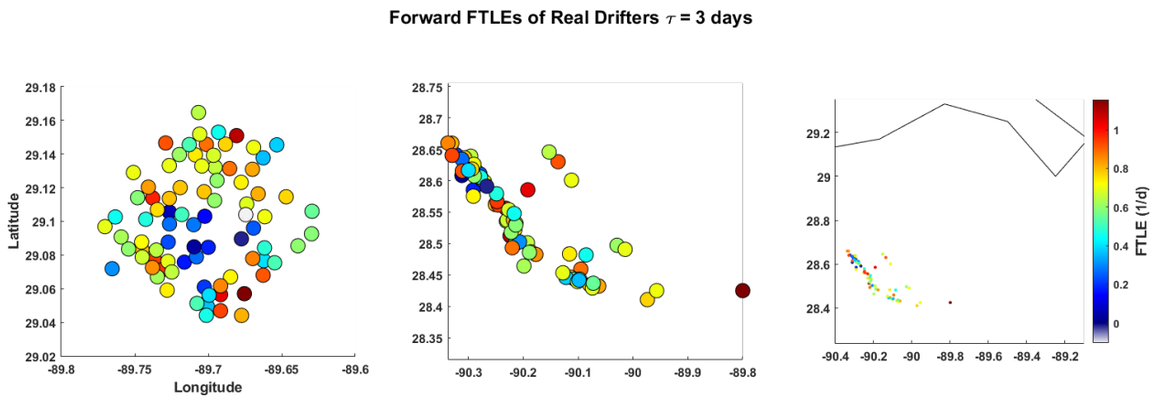

Figure 2-6: Same as Figure 2-4 except for $\tau = 3$ days.

2.3.2 Trajectory Arc-Length

Arc-length results for real drifters are shown below for integration times $\tau = 0.5$, 1, and 3 days. At small integration times such as at $\tau = 0.5$, the separation between small and large-valued arc-length values indicates the separation between drifters which headed north (high arc-length values) and south (low arc-length values) after reaching the coast (see Figure 2-8). These two "clusters" of drifters remain distinguishable even at later times. At $\tau = 1$ and 3 days for instance, there is generally a region of predominantly blue drifters in the southernmost part of the phase space (westernmost cluster of drifters in the final position space) and a red cluster of drifters in the northermost part of the phase space (the long "tail" of drifters in the final-position space). Note that the blue cluster consists of the same low and negatively valued FTLE values from Figures 2-6. Variation within the arc-length field does not change dramatically as τ increases.

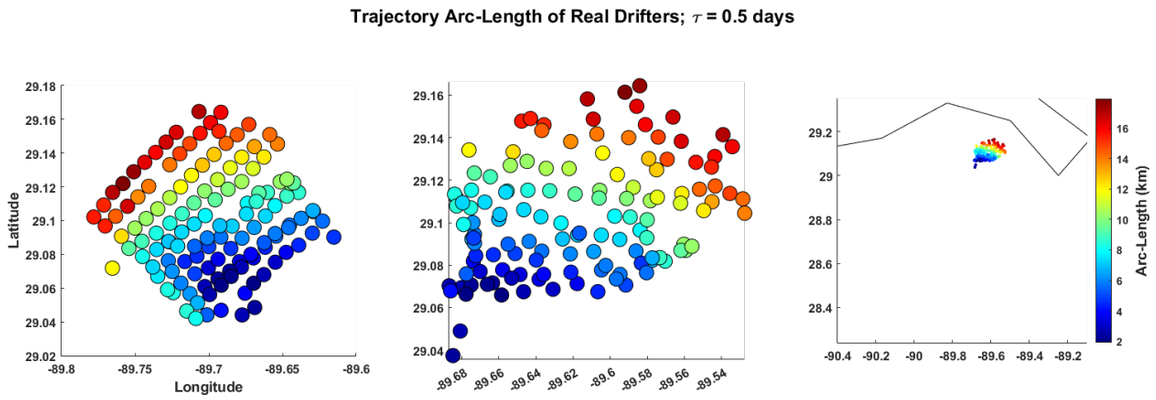

Figure 2-7: Arc-length estimates for real drifters with $\tau = 0.5$. The left panel shows estimates as a function of initial position. Results in the middle and right panels are shown as a function of current position at the integration time.

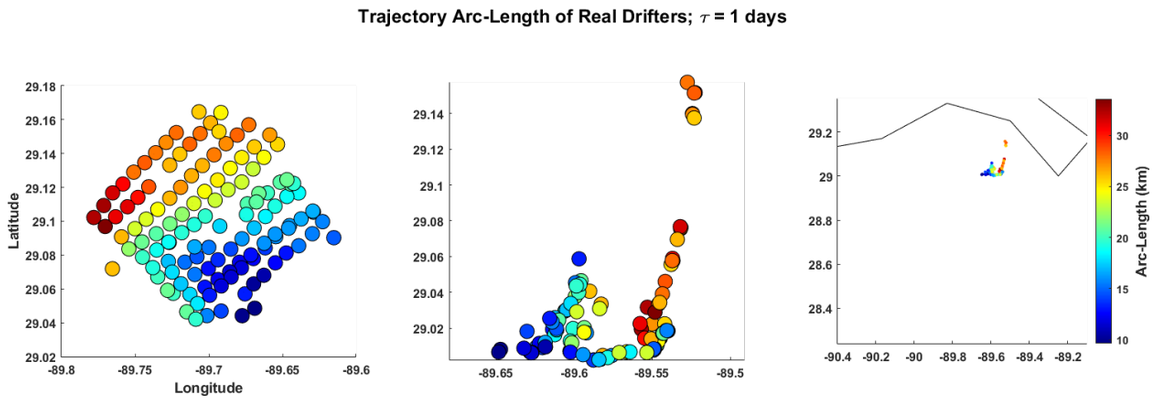

Figure 2-8: Same as Figure 2-7 except for $\tau = 1$ days.

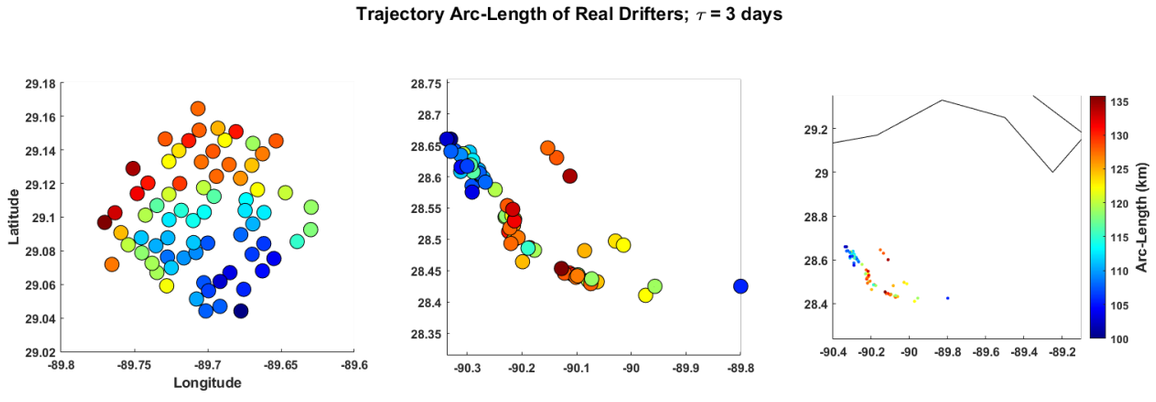

Figure 2-9: Same as Figure 2-7 except for $\tau = 3$ days.

2.3.3 Trajectory Complexity (Correlation Dimension)

Correlation dimension estimates for real drifters are shown below for integration times $\tau = 0.5$, 1, and 3 days. Analysis of correlation dimension for real drifters is similar to the analysis of arc-length. The same separation between drifters which head north as they approach the coast and those which head south can be seen as lower vs. higher values of the correlation dimension (see Figures 2-10 and 2-11). The higher-valued (red) part of the domain is more prevalent in CD compared to arc-length, however. Similarly to arc-length, variation in the CD field does not change dramatically as τ is increased.

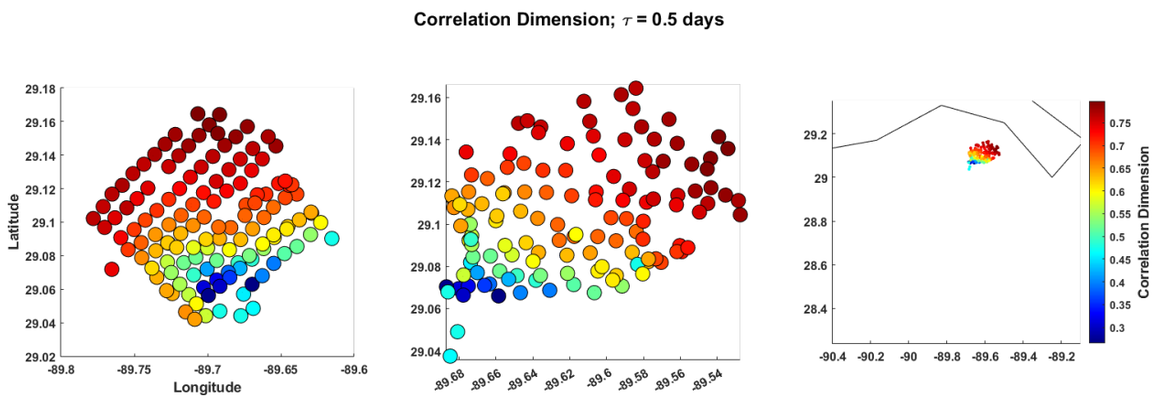

Figure 2-10: Correlation dimension estimates for real drifters with $\tau = 0.5$. The left panel shows estimates as a function of initial position. Results in the middle and right panels are shown as a function of current position at the integration time.

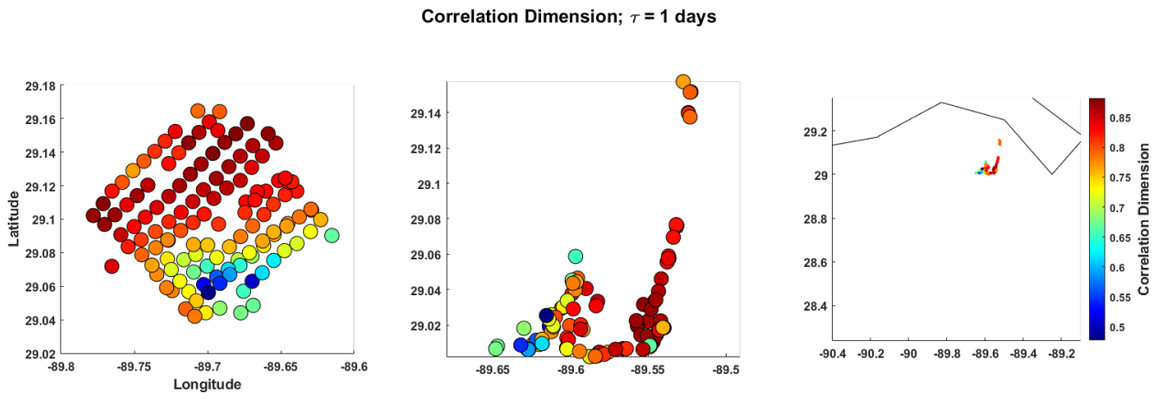

Figure 2-11: Same as Figure 2-10 except for $\tau = 1$ days.

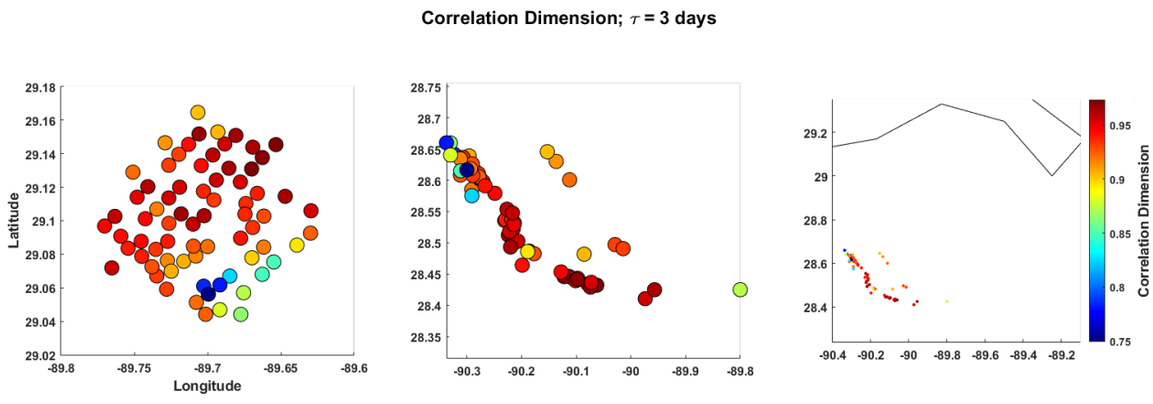

Figure 2-12: Same as Figure 2-10 except for $\tau = 3$ days.

2.3.4 Encounter Number

Encounter number results for real drifters are shown below for integration times $\tau = 0.5$, 1, and 3 days. For the case with $\tau = 0.5$ days, there is an initial region of high encounter number due to some slight convergence in the southernmost part of the domain (see Figure 2-13). This convergence is consistent with the convergence seen in the FTLE fields in Figure 2-4. As drifters reach the coast, the boundary between drifters which head north and south is characterized by high encounter number, since the southward-moving drifters reach the coast slightly later, and begin to encounter some of the northern-moving drifters that already

reached the coast (see Figure 2-14). At later times such as with $\tau = 3$ and beyond, the encounter number field is somewhat noisy as most drifters have made many encounters within their own "clusters," however, a few of the drifters that initially headed north remain far away from the other clusters and maintain persistently low encounter number values (Figure 2-15).

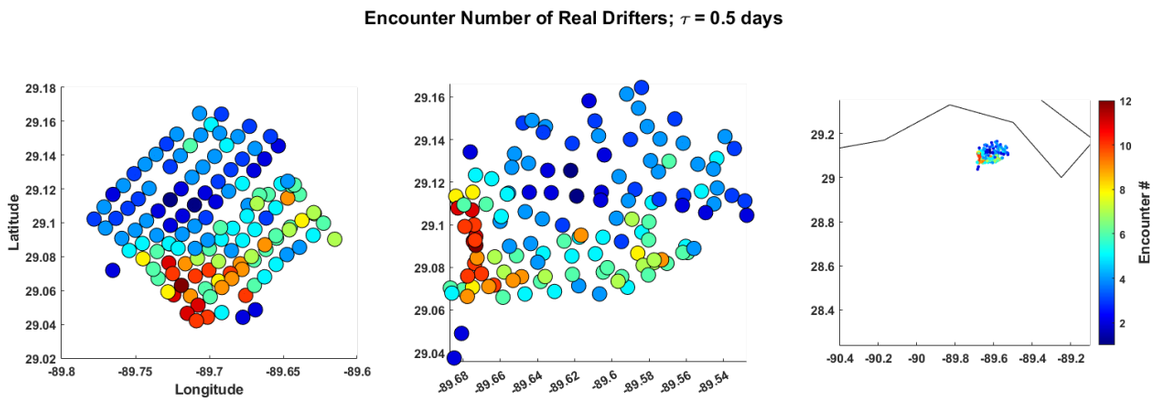

Figure 2-13: Encounter number estimates for real drifters with $\tau = 0.5$. The left panel shows estimates as a function of initial position. Results in the middle and right panels are shown as a function of current position at the integration time.

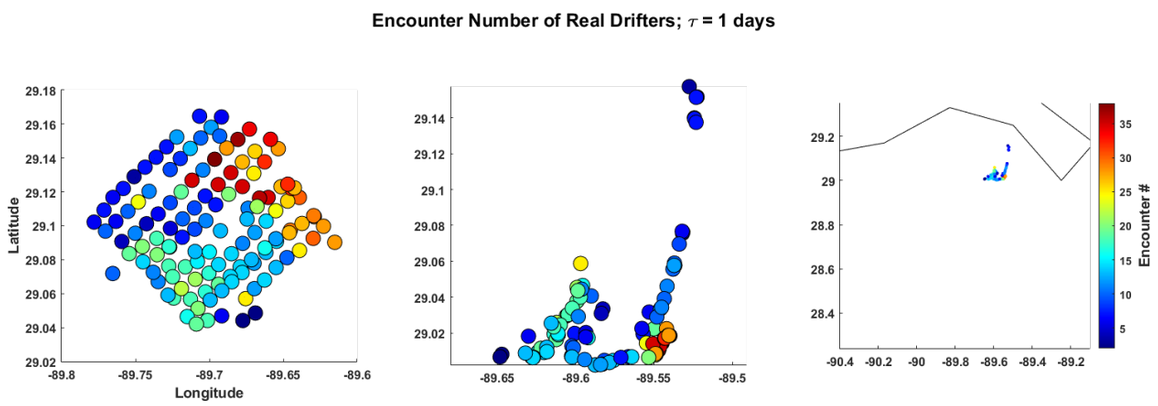

Figure 2-14: Same as Figure 2-13 except for $t = 1$ days.

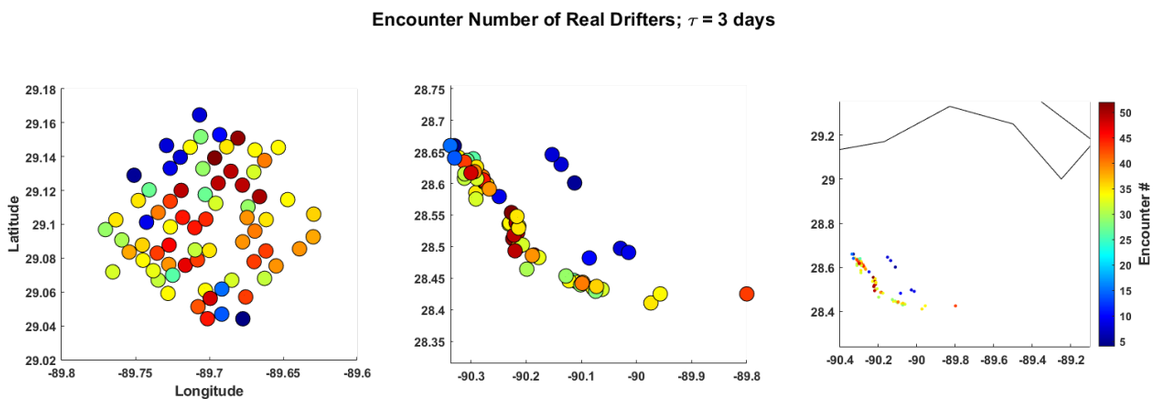

Figure 2-15: Same as Figure 2-13 except for $t = 3$ days.

2.3.5 Divergence and Vorticity

As discussed in Chapter 1, divergence and vorticity estimates using LLS methods are generally good, so long as drifters are not too far from each other and form a sufficiently distributed

polygon with a low aspect ratio. Snapshots of divergence and vorticity estimates from real drifters are shown below for $t = 0.5$, $t = 1$, and $t = 3$ days. A circle is displayed when the more restrictive criteria was used during the computation, and diamonds are shown when the less restrictive criteria was used. Blank diamonds are shown when neither criteria was met. We note that the left columns may be misleading, since they display instantaneous divergence/vorticity of trajectories, as measured at their current location, but as a function of initial position (meaning values in the far left panels do not correspond to the Eulerian divergence/vorticity of their shown locations). These panels have been included for comparison to Dilation and LAVD computation in the following sections. In the middle and right panels, values correspond correctly to their shown location.

Divergence and vorticity estimates for real drifters are generally $\mathcal{O}(10^{-5})$ at small times ($t < 1$ day) and $\mathcal{O}(10^{-4})$ at larger times (t > 1 day). Values of order $\mathcal{O}(10^{-4})$ are comparable to estimates from multi-layer drifters near the Almeria-Oran front in Chapter 1. Values at long times are also relatively noisy and difficult to interpret, aside from a few regions which experience noticeable convergence or rotation.

Divergence fields reveal a region of slight convergence (negative divergence) in the southwestern part of the final-position domain in Figure 2-16 at $t = 0.5$. This convergence is consistent with the negative FTLE values and high encounter numbers in Figures 2-4 and 2-13. There is also a region of negative divergence at $t = 1$ in Figure 2-14, within the zone where southward-moving drifters begin to reach the coast and interact with northward-moving drifters. This convergence is again consistent with the negative FTLE values and high encounter number in Figures 2-5 and 2-14.

Vorticity is initially predominantly negative, indicating anticyclonic (clockwise) rotation in Figure 2-17. There is also a region of larger negative values in the southernmost part of the domain at $t = 0.5$ days, indicating much stronger anticylonic rotation than surrounding regions. At $t = 1$ day, there is a region of strong positive vorticity values in the region where the northward and southward-moving drifters meet, indicating particularly strong cyclonic (counter-clockwise) rotation in this convergence zone.

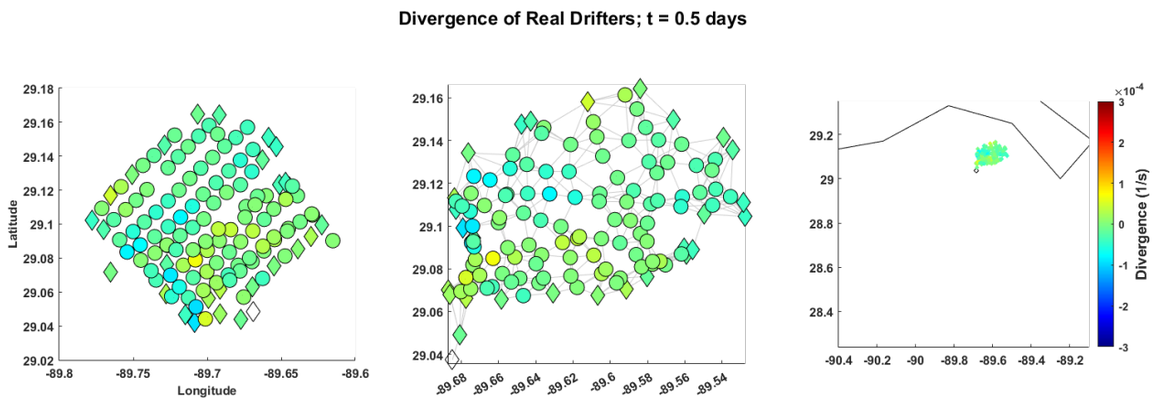

Figure 2-16: Divergence estimates for real drifters at $t = 0.5$. The left panel shows estimates as a function of initial position. Results in the middle and right panels are shown as a function of current position at the integration time.

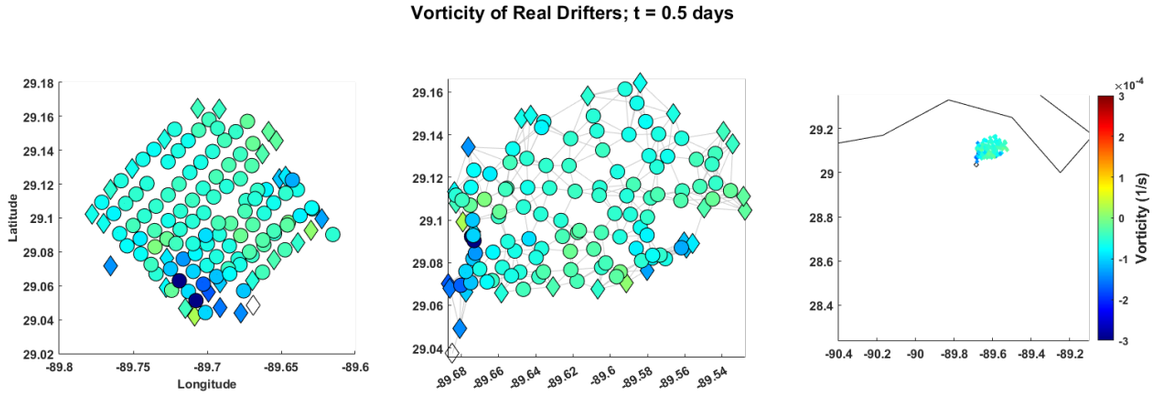

Figure 2-17: Vorticity estimates for real drifters at $t = 0.5$. The left panel shows estimates as a function of initial position. Results in the middle and right panels are shown as a function of current position at the integration time.

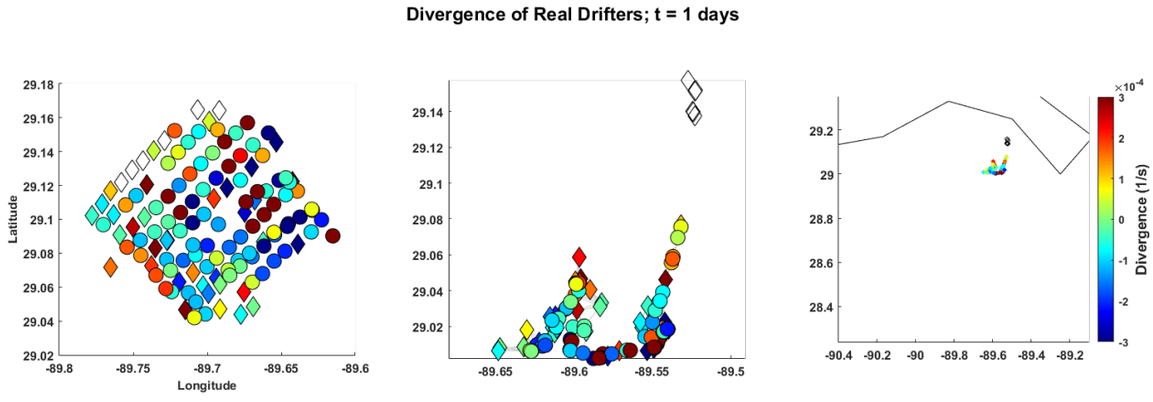

Figure 2-18: Same as Figure 2-16 except for $t = 1$ days.

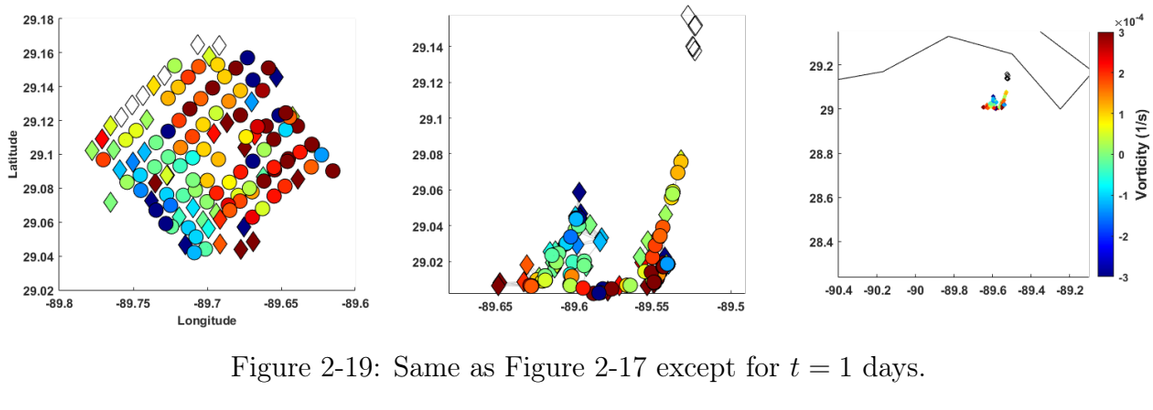

Figure 2-19: Same as Figure 2-17 except for $t = 1$ days.

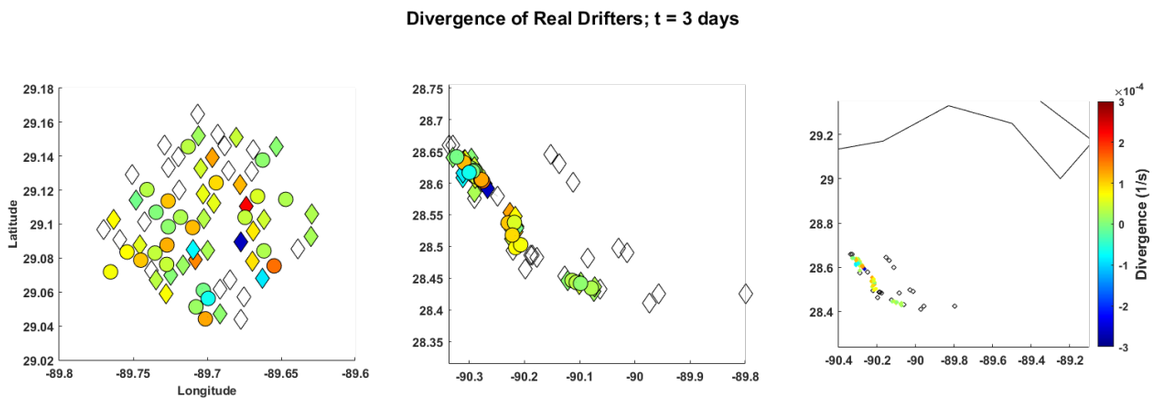

Figure 2-20: Same as Figure 2-16 except for $t = 3$ days.

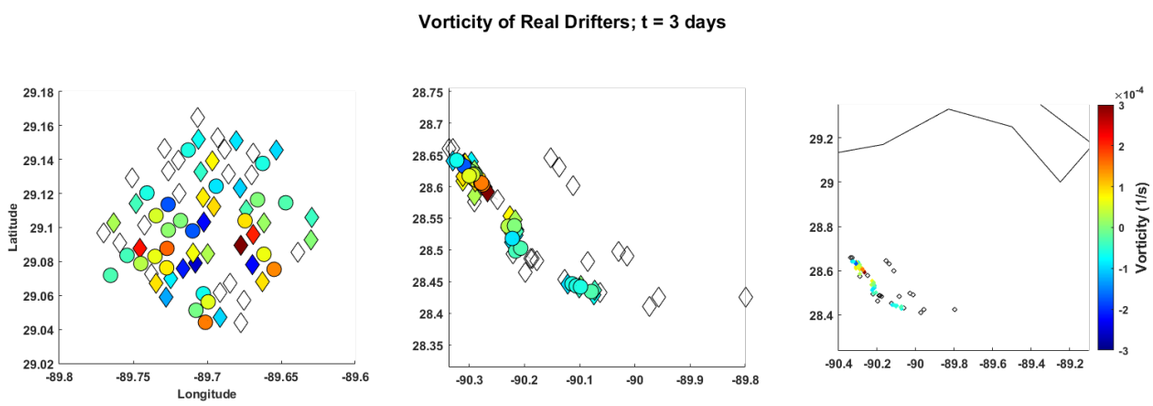

Figure 2-21: Same as Figure 2-17 except for $t = 3$ days.

2.3.6 Dilation

Dilation estimates for real drifters are shown below for integration times $\tau = 0.5$, 1, and 3 days. Dilation estimates with $\tau = 0.5$ and $\tau = 1$ highlight similar features as FTLEs and encounter number. For instance, in the case with $\tau = 0.5$, the region of slight convergence in the southernmost part of the domain is captured well in the dilation field (see Figure 2-22). For $\tau = 1$, the convergence region between southward and northward-moving drifters is also captured, indicating the separation between these two regimes (Figure 2-23). At longer times, dilation is predominantly negative, which may indicate that drifters throughout much of the domain passed through regions of strong downwelling. The same predominantly negative dilation is also indicative of the drifters converging into tight clusters as seen for $\tau = 3$ days (Figure 2-24).

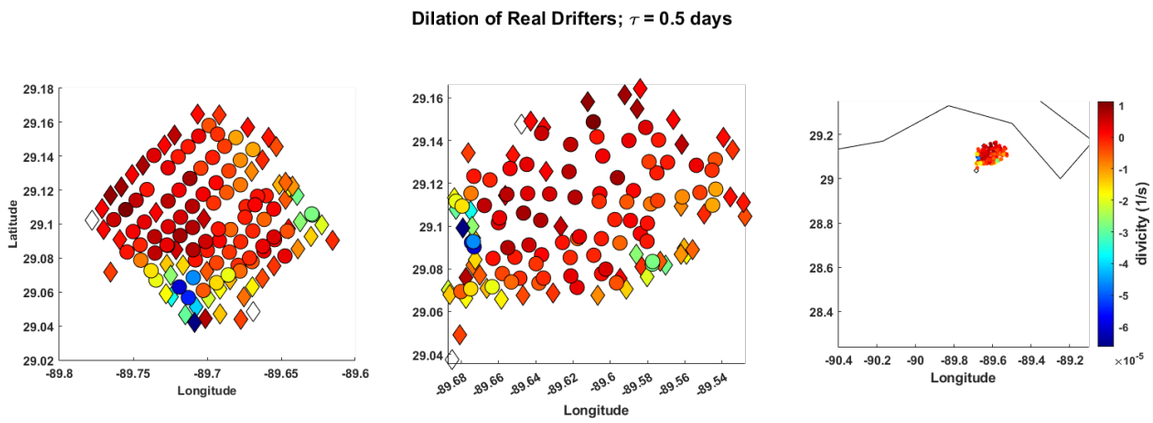

Figure 2-22: Dilation estimates for real drifters with $\tau = 0.5$. The left panel shows estimates as a function of initial position. Results in the middle and right panels are shown as a function of current position at the integration time.

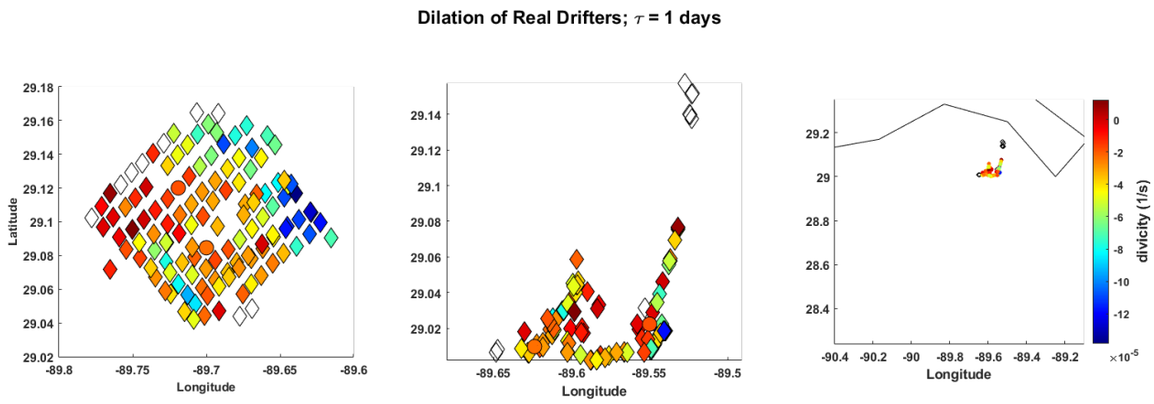

Figure 2-23: Same as Figure 2-22 except for $\tau = 1$ days.

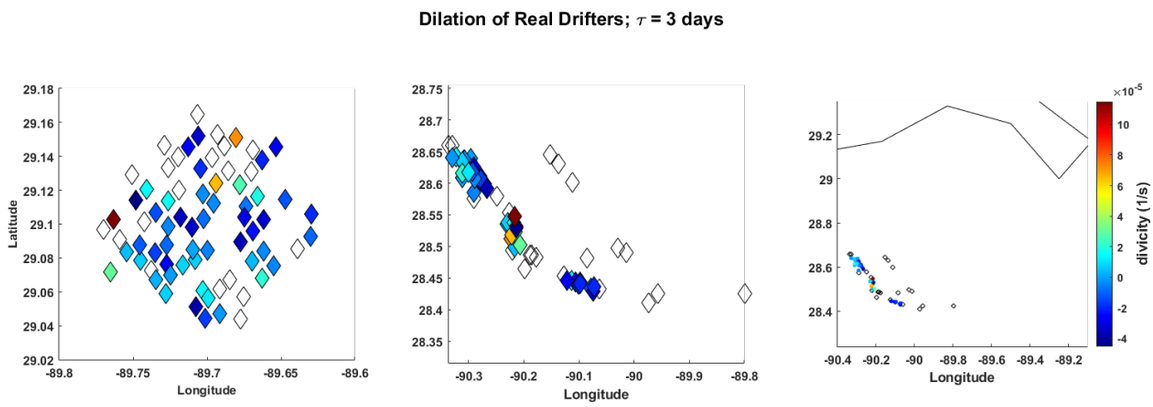

Figure 2-24: Same as Figure 2-22 except for $\tau = 3$ days.

2.3.7 Lagrangian-Averaged Vorticity Deviation

LAVD estimates for real drifters are shown below for integration times $\tau = 0.5$, 1, and 3 days. The estimates indicate drifters from regions which experience different rotation characteristics compared to their surrounding drifters. For instance, LAVD with integration time $\tau = 0.5$ days indicates a region of high LAVD in the southernmost part of the domain. This region is rotating slightly faster (more strongly anticylonically) than the rest of the distribution. This is consistent with the strongly negative vorticity values seen in the eastern

part of the domain in Figure 2-17. As drifters approach the coast, strong cyclonic (counter-clockwise) rotation is seen near the boundary between drifters that headed north or south, which is also consistent with the predominantly positive vorticity values in the easternmost part of the domain in Figure 2-19. For $\tau = 3$ days and beyond, some drifters in the center "cluster" of the final-position domain have large LAVD values, compared to other clusters of drifters, possibly indicating that this cluster experiences more rotation than the two clusters on either side of it. This behavior is not particularly evident in the vorticity snapshot at $t = 3$ days in Figure 2-21, but the corresponding high vorticity values exist at some intermediate times between days 1 and 3.

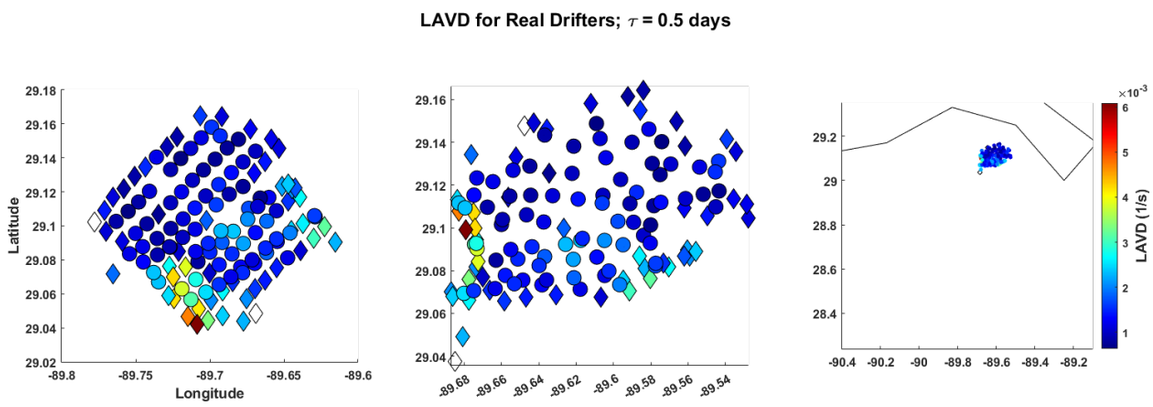

Figure 2-25: LAVD estimates for real drifters with $\tau = 0.5$. The left panel shows estimates as a function of initial position. Results in the middle and right panels are shown as a function of current position at the integration time.

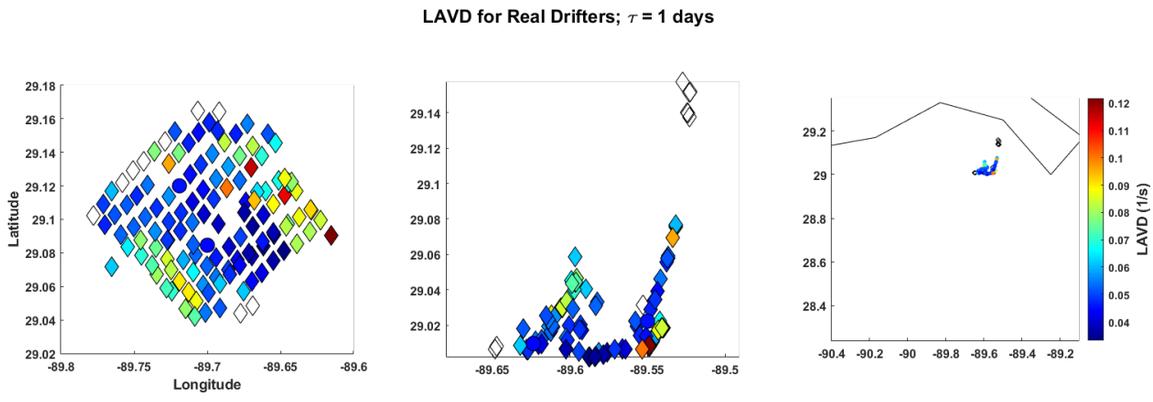

Figure 2-26: Same as Figure 2-25 except for $\tau = 1$ days.

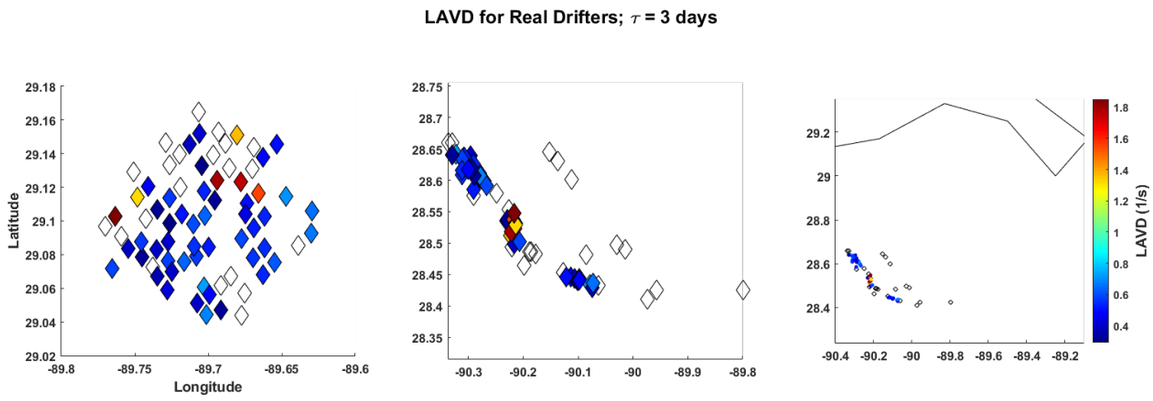

Figure 2-27: Same as Figure 2-25 except for $\tau = 3$ days.

2.3.8 Spectral Clustering of Trajectories

Figures of spectral clustering results for real drifters are shown in Figures 2-28 through 2-30. At short times such as with $\tau = 0.5$ days, results are not particularly meaningful since very little information about trajectory separation or connection is available. For $\tau = 1$ day, trajectories are somewhat organized into drifters that moved northward vs southward as they approached the coast, with the exception that some southward-moving trajectories are included in the perceived northern clusters. For the case of $\tau = 3$ days, clusters visually correspond very well to their perceived groupings.

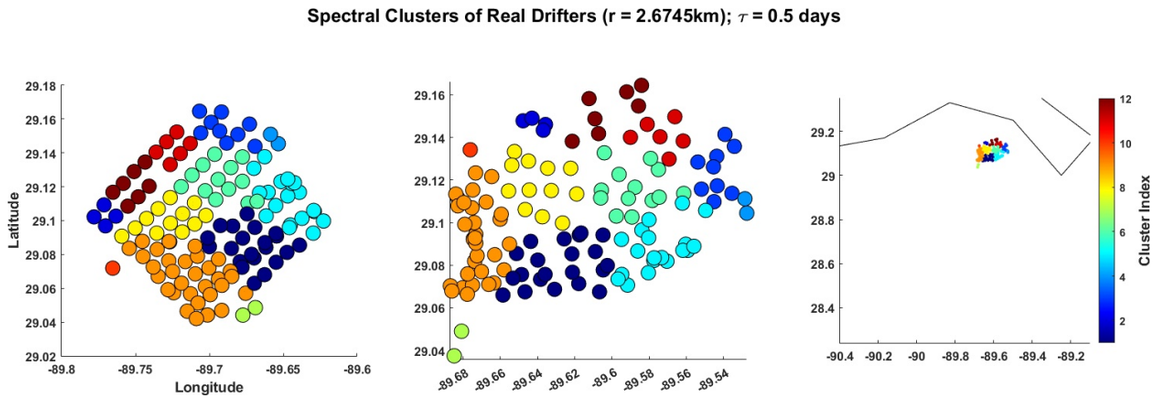

Figure 2-28: Spectral clusters for real drifters with $\tau = 0.5$. The left panel shows estimates as a function of initial position. Results in the middle and right panels are shown as a function of current position at the integration time.

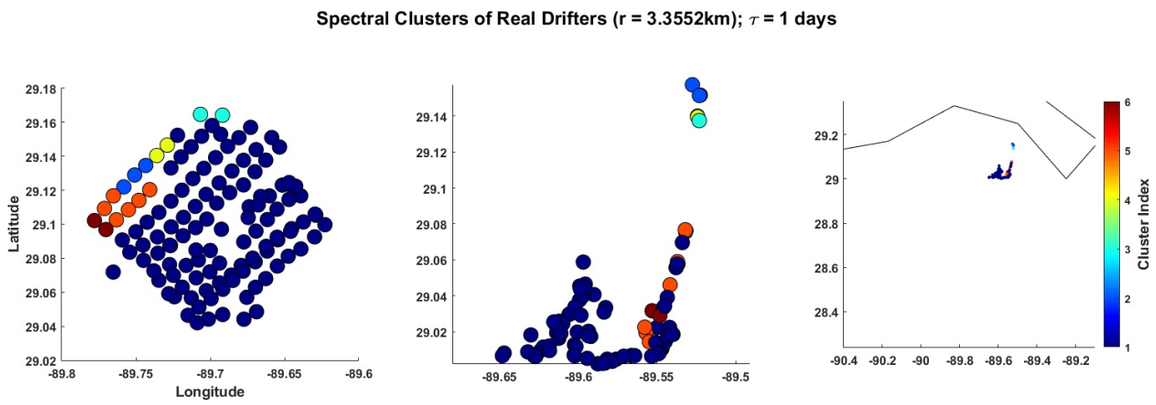

Figure 2-29: Same as Figure 2-28 except for $\tau = 1$ days.

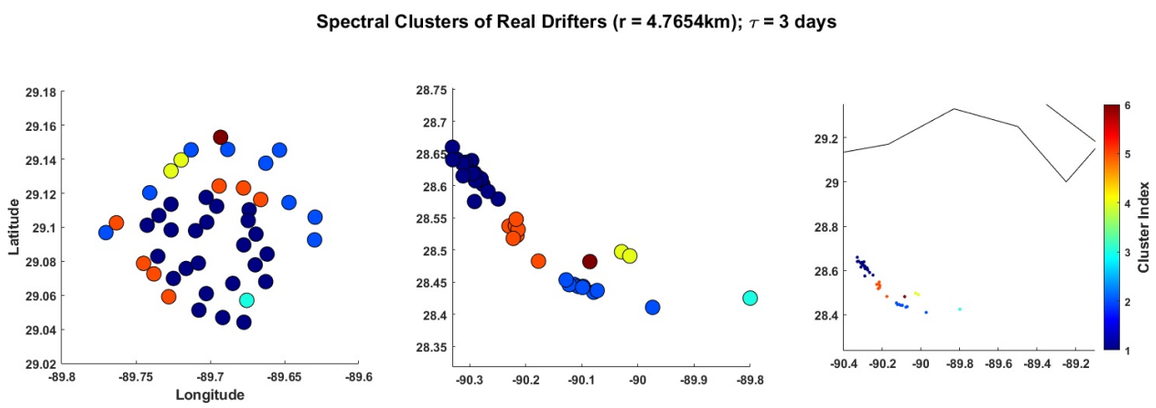

Figure 2-30: Same as Figure 2-28 except for $\tau = 3$ days.

2.4 Analysis of Simulated Drifter Results

In this section, results of FTLEs, arc-length, correlation dimension, encounter number, divergence, vorticity, dilation, LAVD, and spectral clustering are shown for estimates from simulated drifters (top rows in Figures 2-31 through 2-52) and for trajectories with a dense grid of initial positions (bottom rows). Results are shown generally for integration times $\tau = 0.5$, 2, and 4 days. For encounter number, integration time $\tau = 1.5$ is shown rather than $\tau = 2$ to more clearly highlight similar features as other results. The dense grid has spacing of 0.001 degrees, with the exception of the correlation dimension results, for which a spacing of 0.004 degrees was used due to CD being computationally expensive. The domain of each grid extends slightly beyond the boundaries of the shifted diamond, between longitudes -89.64 °E and -89.46 °E, and latitudes 28.95 °N and 29.10 °N. One exception is for LAVD, which uses only trajectories beginning in the diamond-shaped polygon spanned by drifters. This tighter window was used since LAVD involves the instantaneous spatial mean of vorticity, and so the domain over which the mean is computed should be similar for both simulated drifters and gridded trajectories, in order for the two fields to remain comparable. Figures consist of panels of the LCS metrics and their values at the integration time τ as functions of initial position (left columns in Figures 2-31 through 2-52), and final positions (middle and right columns). With the exception of divergence and vorticity, all metrics should be viewed as functions of initial position alone (left columns) for interpreting LCSs, however, including final positions helps the viewer to visually see where trajectories near certain features appear at later times.

2.4.1 Finite-time Lyapunov Exponents

In the computations using a dense grid of trajectories, several FTLE ridges appear at different time scales. The first ridge begins to appear on the west side of the domain at short times and is well-defined at $t = 2$ days (see Figures 2-31 and 2-32). This ridge separates drifters which head north as they reach the coast from those which head south. At longer integration time, this ridge begins to disappear since drifters from both regimes begin to experience the same behavior on average (see Figure 2-33). Another notable ridge traverses the domain in the east/west direction along the bottom quarter of the domain. This ridge separates trajectories which do and do not approach the coast (i.e., trajectories lying on the south side of this ridge head west while all other trajectories head east toward the coast). Another s-shaped ridge appears in the far west of the domain. This ridge separates trajectories which eventually travel much further south than other trajectories.

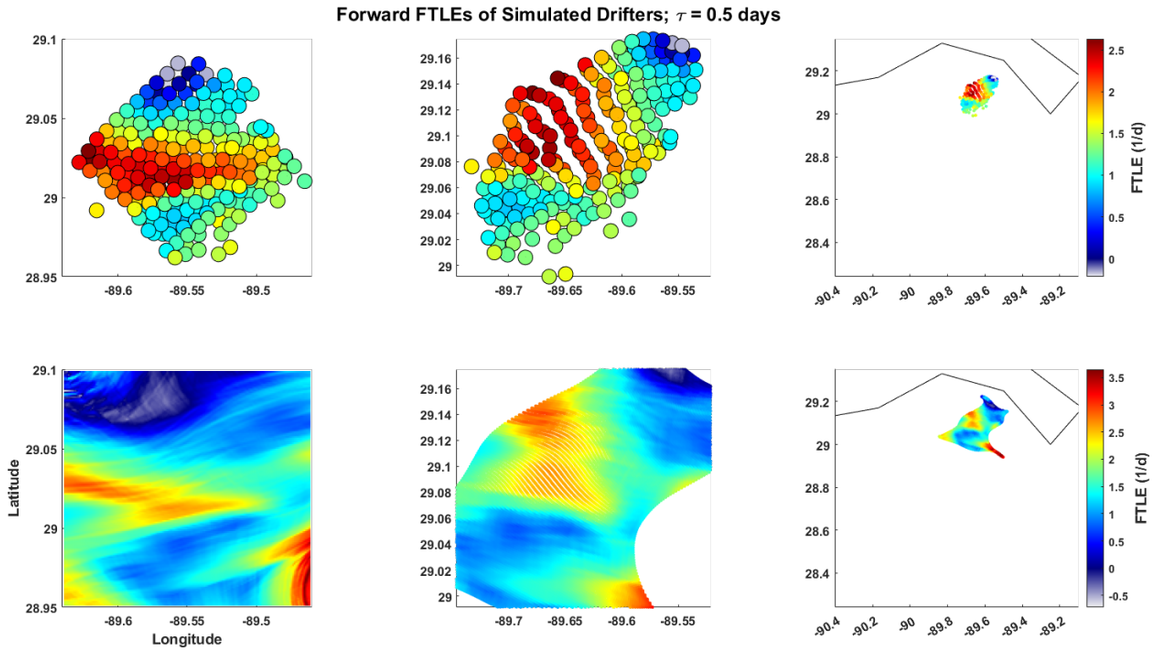

Figure 2-31: FTLE fields for results from simulated drifters (top row) and from a grid with spacing of .001 degrees (bottom row) with integration time $\tau = 0.5$. Results in the left column (top left and bottom left) are shown as a function of initial position. Results in the middle and right columns are shown as a function of current position at the integration time.

FTLEs estimated from simulated drifters capture trajectory behavior nearly as well as the dense grid. At $\tau = 2$ for instance, the ridge separating the drifters which head north/south can be inferred from simulated drifters rather clearly. Other ridges in the domain lie on the edge of the diamond formed by simulated drifters, so they are fuzzy and not distinguishable as distinct lines. Nevertheless, the simulated drifters capture high FTLE values in these regions, and successfully categorize the flow into the same regions of behavior.

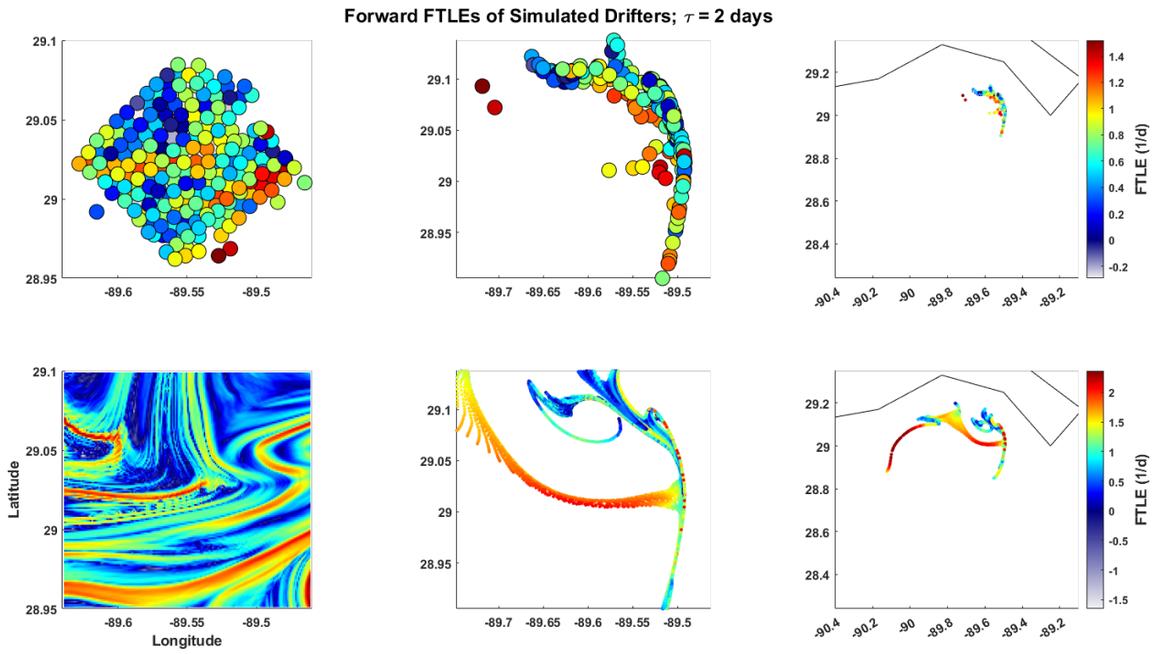

Figure 2-32: Same as Figure 2-31 except for $t = 2$ days.

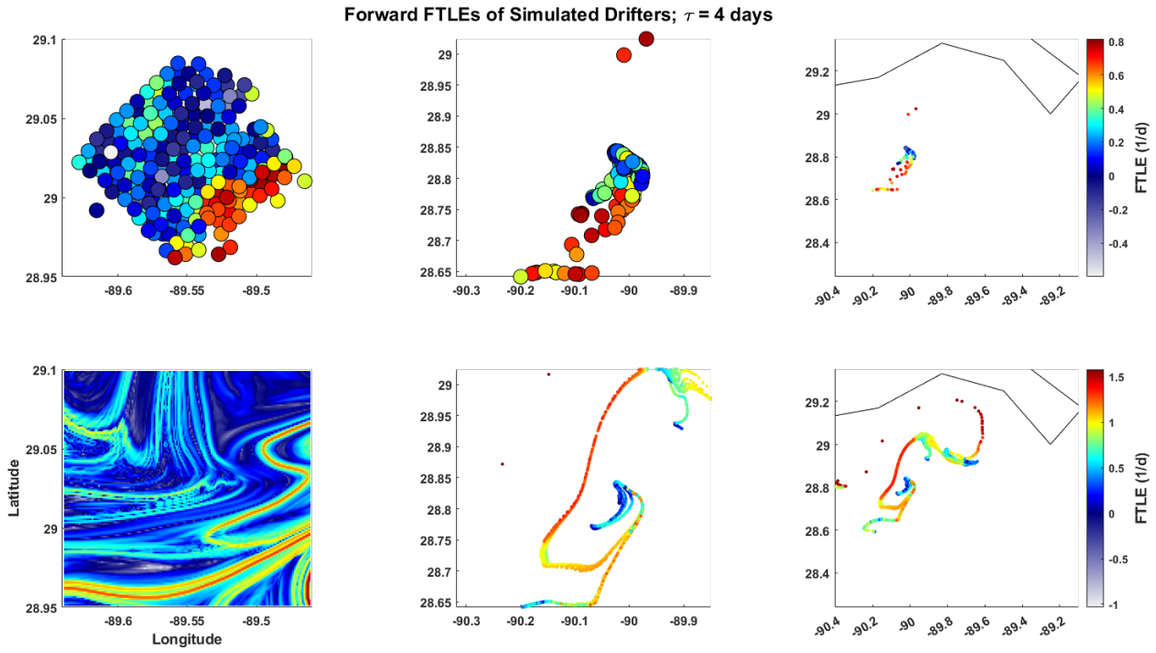

Figure 2-33: Same as Figure 2-31 except for $t = 4$ days.

2.4.2 Trajectory Arc-Length

In the dense grid of initial positions, trajectories which head north or south as they approach the coast can be roughly distinguished in the arc-length field by high values (in the south) and low values (in the north) at $\tau = 0.5$ and $\tau = 2$ days, for both simulated drifters and trajectories from the regularly-spaced grid (see Figures 2-34 and 2-35). This is because trajectories in the north of the domain reached the coast first, moved north slightly, and then remained there with minimal movement for some time while the southern trajectories approach the coast later on.

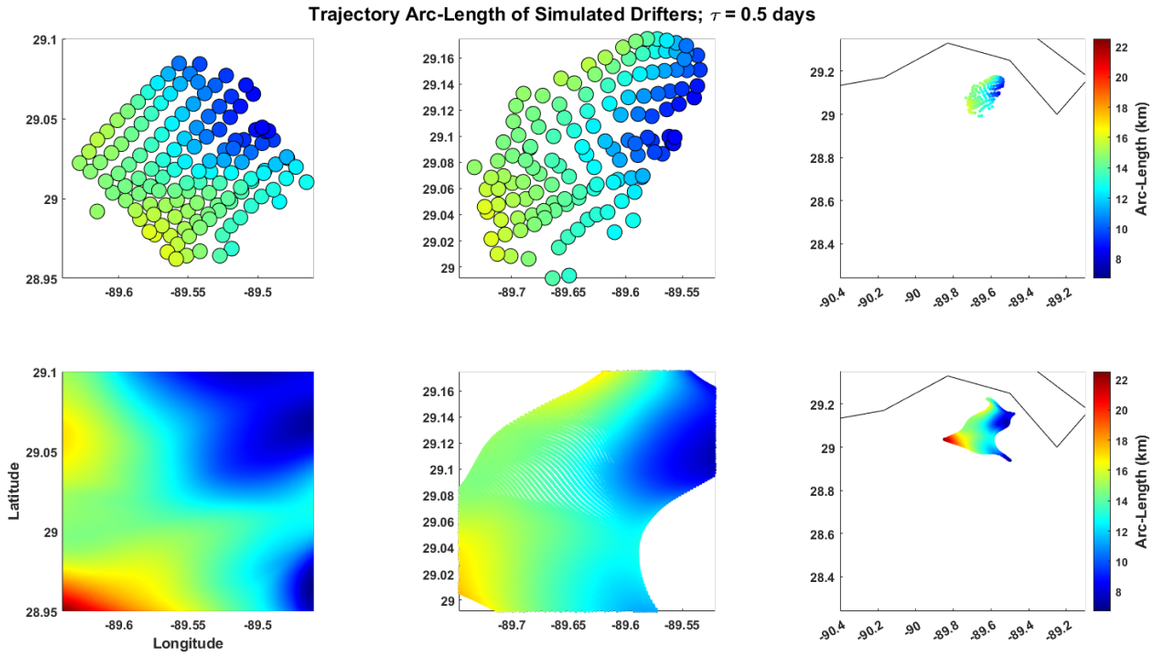

Figure 2-34: Arc-length fields for results from simulated drifters (top row) and from a grid with spacing of .001 degrees (bottom row) with integration time $\tau = 0.5$. Results in the left column (top left and bottom left) are shown as a function of initial position. Results in the middle and right columns are shown as a function of current position at the integration time.

While arc-length values from simulated drifters are identical for gridded trajectories with the same location, fields computed from simulated drifters are relatively hard to interpret visually, since features are analytically associated with gradients in the arc-length field rather than any particular minima or maxima. Large gradients appear as sharp features in the field with a densely populated grid, but these sharp features are difficult to observe when only sparse trajectories are available.

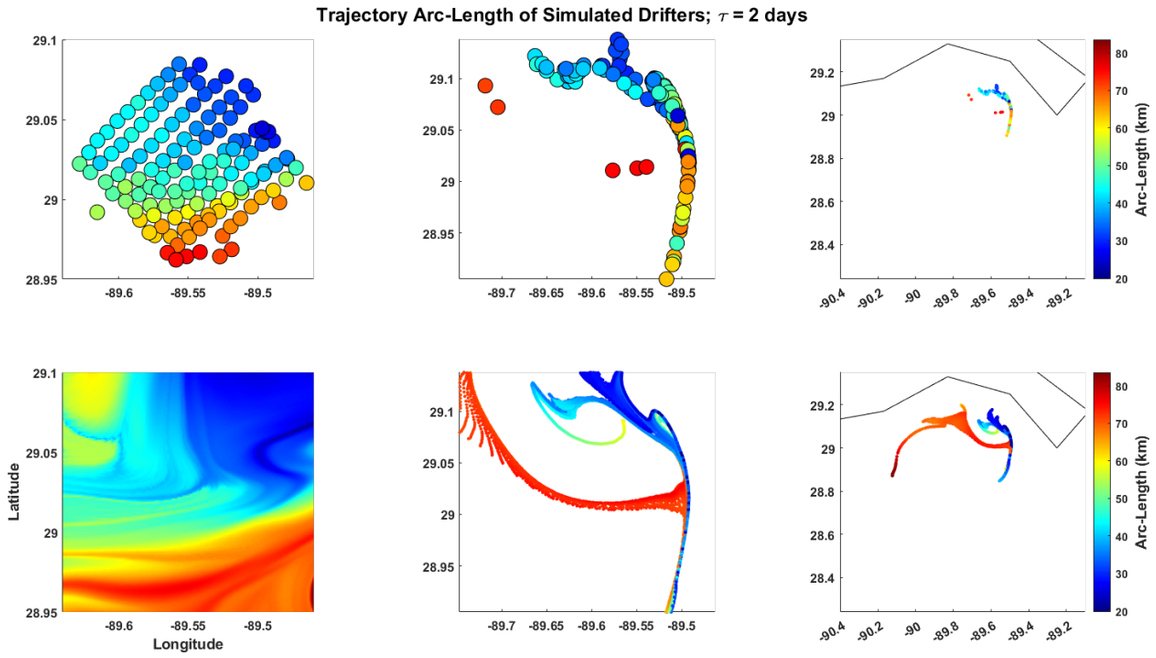

Figure 2-35: Same as Figure 2-34 except for $\tau = 2$ days.

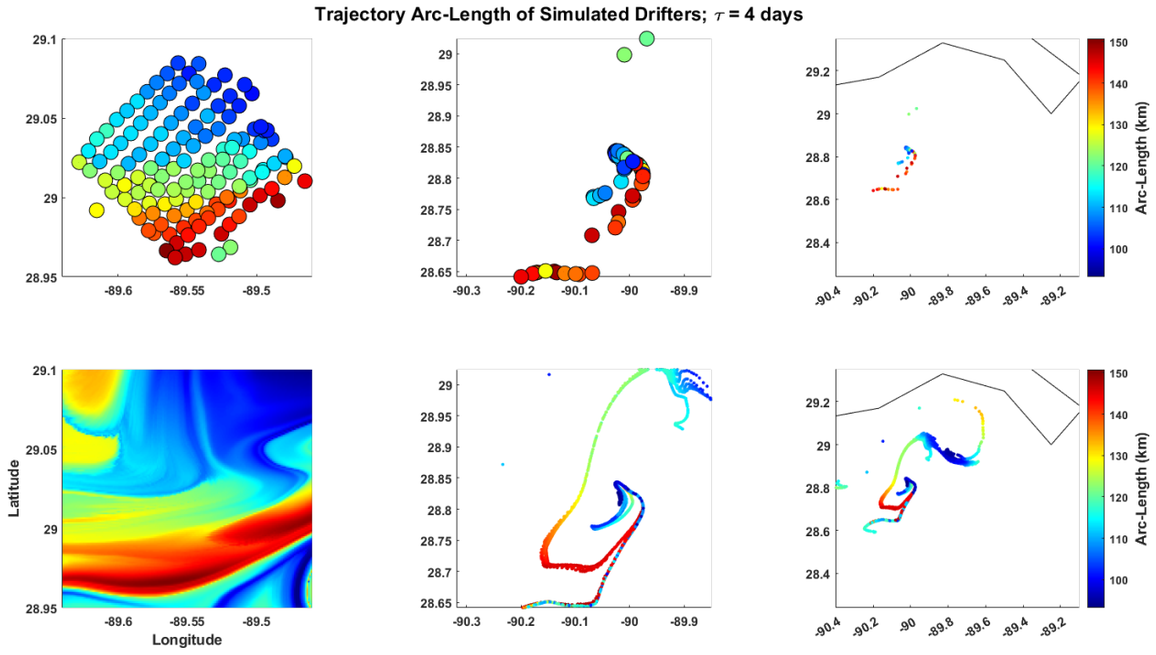

Figure 2-36: Same as Figure 2-34 except for $\tau = 4$ days.

2.4.3 Trajectory Complexity (Correlation Dimension)

Due to correlation dimension being computationally expensive, CD fields were computed for a slightly sparser grid than in other metrics. The CD fields categorize the flow into similar regimes as FTLEs and arc-length. At $\tau = 2$ for instance, the separation between drifters which headed north or south can be seen in CD fields estimated from both simulated drifters and from a dense grid. Drifters which headed north can be seen with relatively low values compared to those with high values which headed south (from the southern part of the domain).

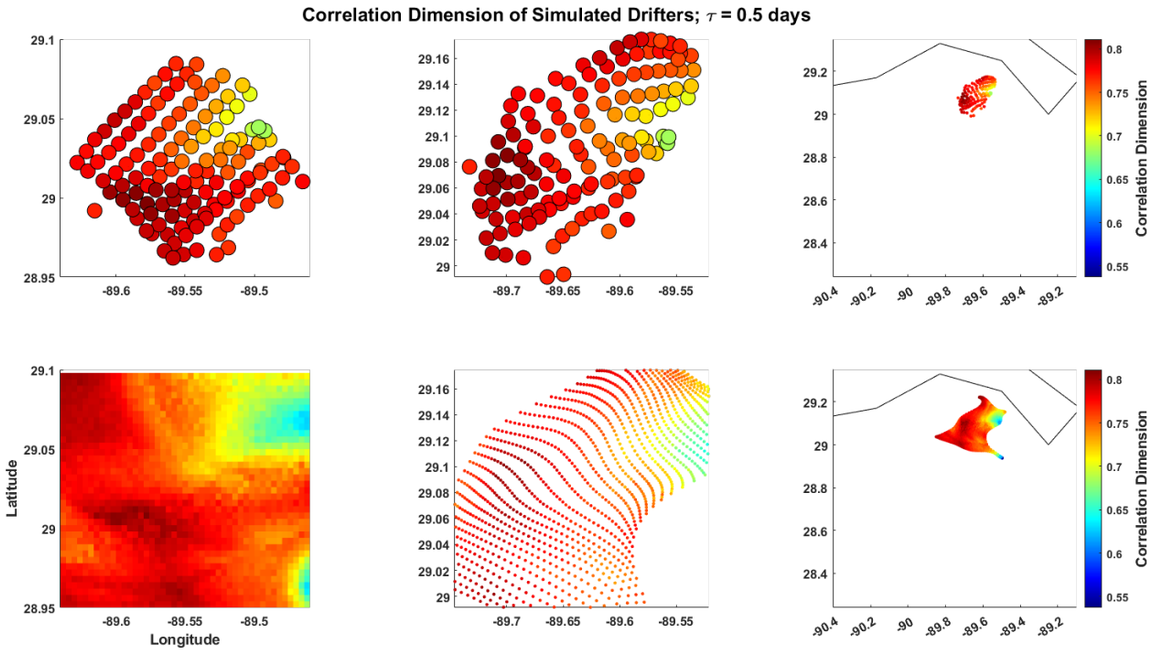

Figure 2-37: Correlation Dimension field for results from simulated drifters (top row) and from a grid with spacing of .004 degrees (bottom row) with integration time $\tau = 0.5$. Results in the left column (top left and bottom left) are shown as a function of initial position. Results in the middle and right columns are shown as a function of current position at the integration time.

The s-shaped ridge in the Eastern part of the domain can also be distinguished at $\tau = 2$ and $\tau = 4$. The long ridge which traverses in the east/west direction can also be distinctly seen as the large arc-length (dark red) ridge in the southern part of the domain for gridded trajectories, but is not seen in the simulated drifter estimates which lie above this ridge.

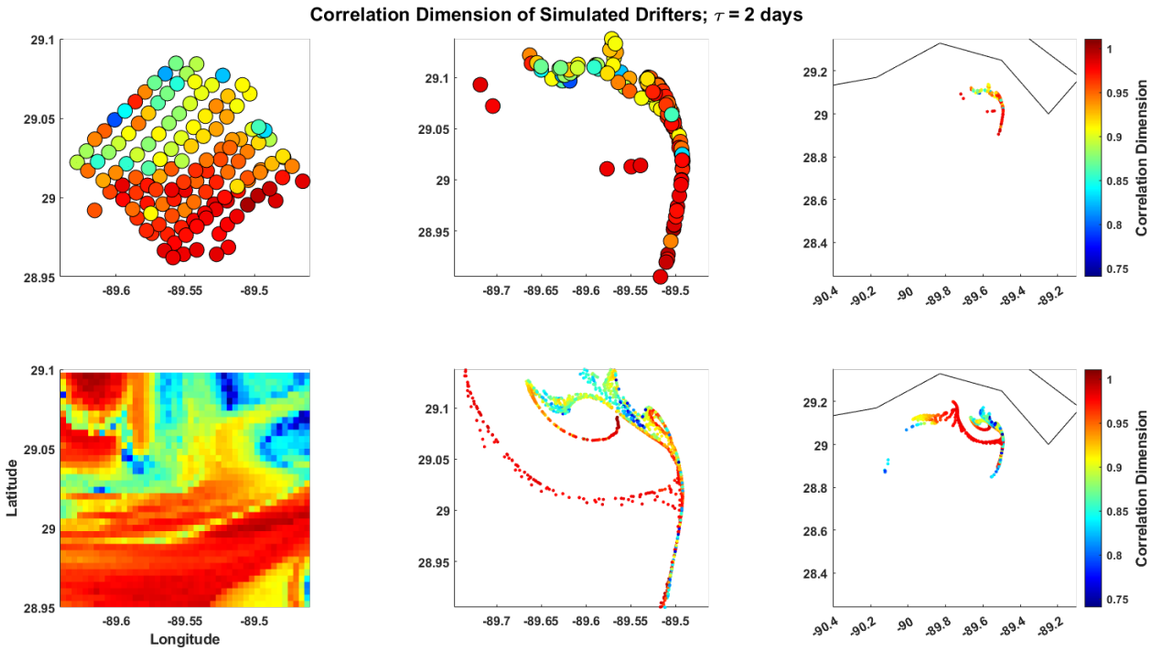

Figure 2-38: Same as Figure 2-37 except for $\tau = 2$ days.

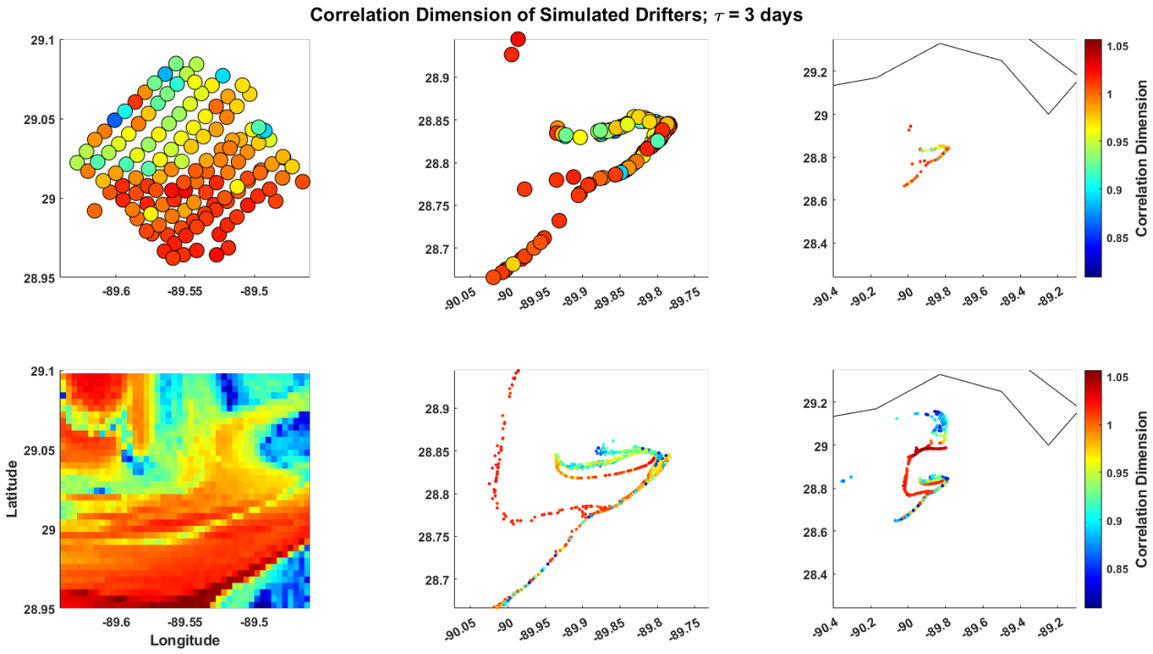

Figure 2-39: Same as Figure 2-37 except for $\tau = 4$ days.

2.4.4 Encounter Number

Encounter number for simulated drifters shows minimal information at short time, since drifters are irregularly spaced initially (so some drifters have more neighbors within $R = 1$km than others at the beginning due to their placement alone). As integration time increases, these difference balance out and become visually similar to results from the dense grid of trajectories. At $\tau = 1.5$, the same ridge seen in FTLEs which separated drifters heading northward/southward can be seen as a ridge of high encounter number (for simulated drifters) and high encounter volume (for the dense grid). Trajectories in this region made contact with parcels on both sides of the domain, causing the high encounter number and encounter volume values. At larger times such as at $t = 4$, the s-shaped ridge becomes visible. The

longer east/west traversing ridge seen in FTLEs does not appear in encounter volume as a maximal ridge, but there is a separation between extremely low encounter volume (on the southern side of the FTLE ridge) and slightly higher encounter volume (on the northern side of the FTLE ridge). For integration times longer than $\tau = 4$, most simulated drifters have interacted with almost every other simulated drifter, so the field becomes flat and can no longer be compared to the dense grid computation.

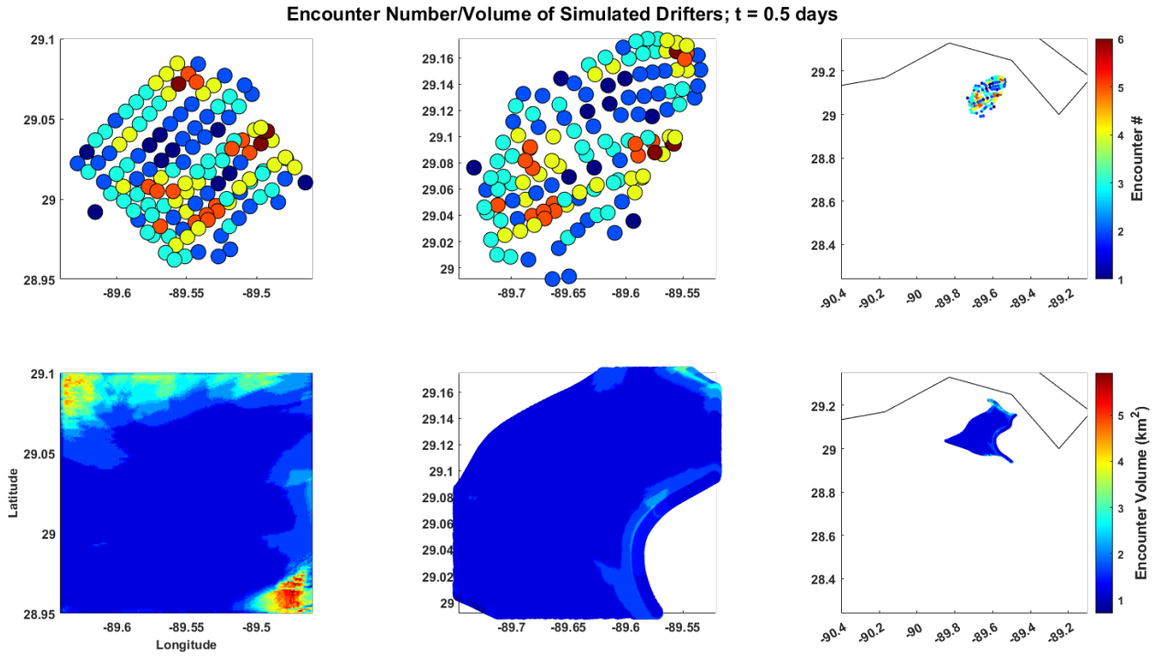

Figure 2-40: Encounter number and volume fields for results from simulated drifters (top row) and from a grid with spacing of .001 degrees (bottom row) with integration time $\tau = 0.5$. Results in the left column (top left and bottom left) are shown as a function of initial position. Results in the middle and right columns are shown as a function of current position at the integration time.

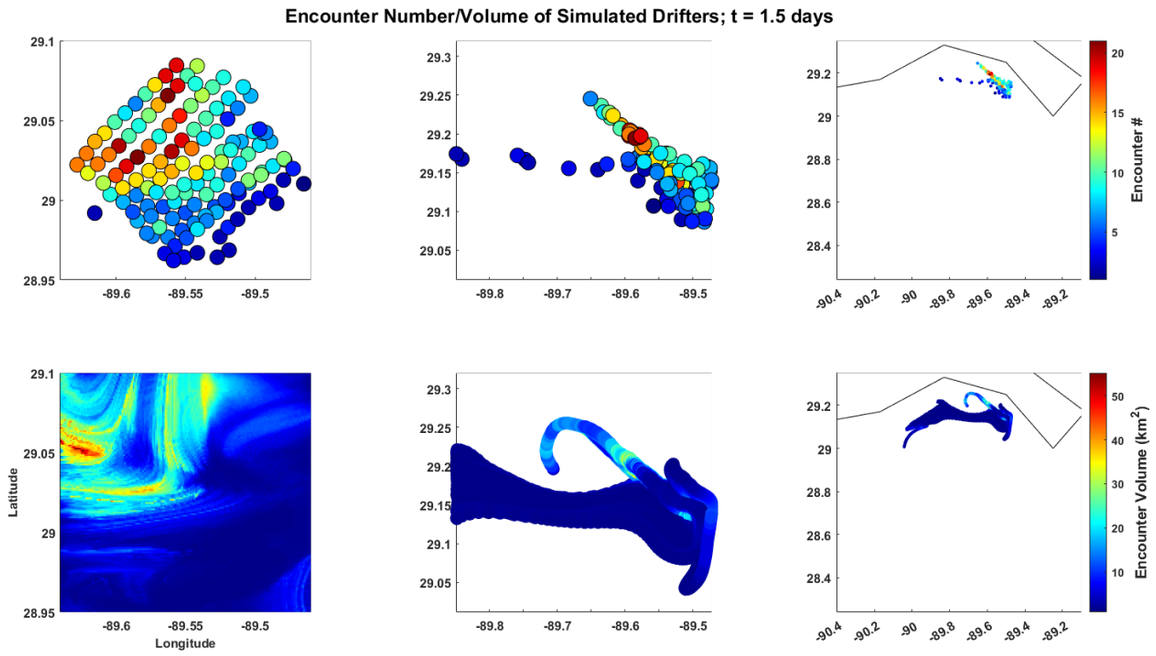

Figure 2-41: Same as Figure 2-40 except for $\tau = 1.5$ days.

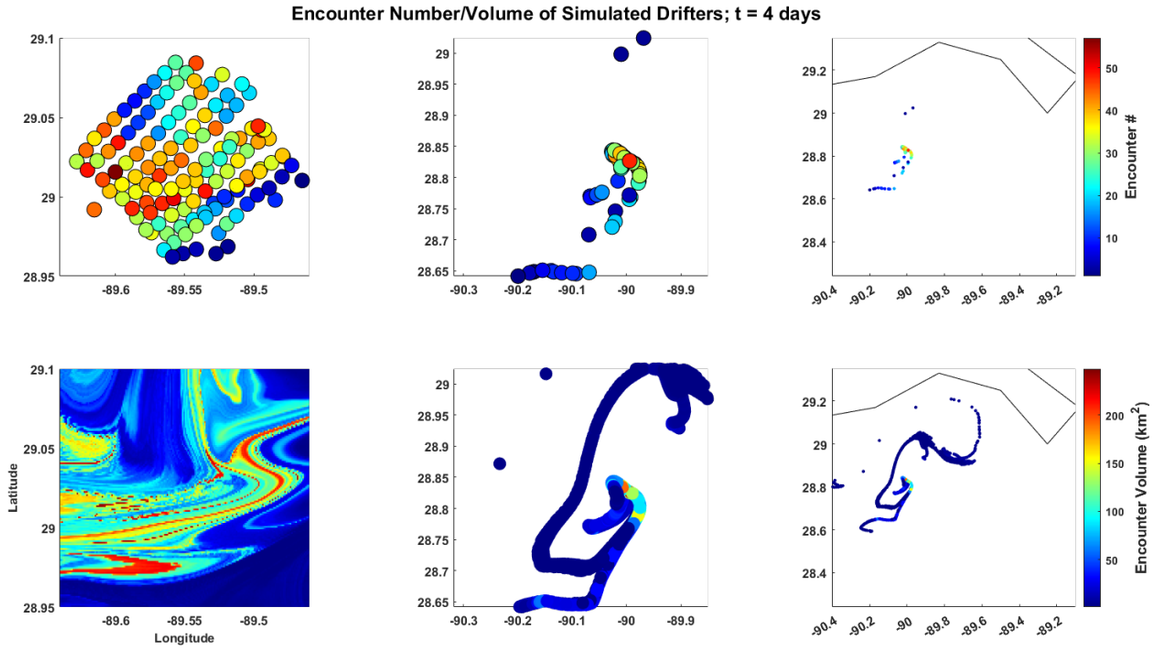

Figure 2-42: Same as Figure 2-40 except for $\tau = 4$ days.

2.4.5 Divergence and Vorticity

Snapshots of divergence and vorticity estimates from simulated drifters are shown below for $t = 0.5$, $t = 2$, and $t = 4$ days. Values are shown with circles, diamonds, or empty diamonds based on the same criteria as real drifters. Values of divergence and vorticity estimated from simulated drifters typically agree quite well with values from the model field at most times. Some estimates (including some even at times when the "good" criteria is met) give poor results, but these appear rarely and instantaneously.

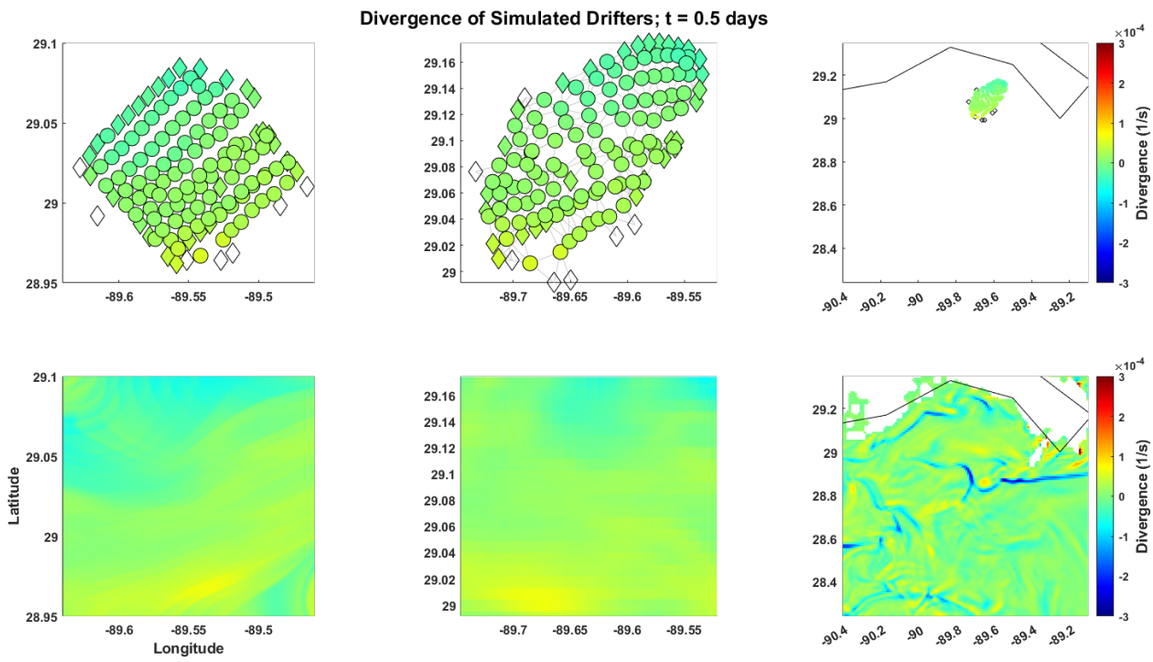

Figure 2-43: Divergence field for results from simulated drifters (top row) and from a grid with spacing of .001 degrees (bottom row) at time $t = 0.5$. Results in the left column (top left and bottom left) are shown as a function of initial position. Results in the middle and right columns are shown as a function of current position at the integration time.

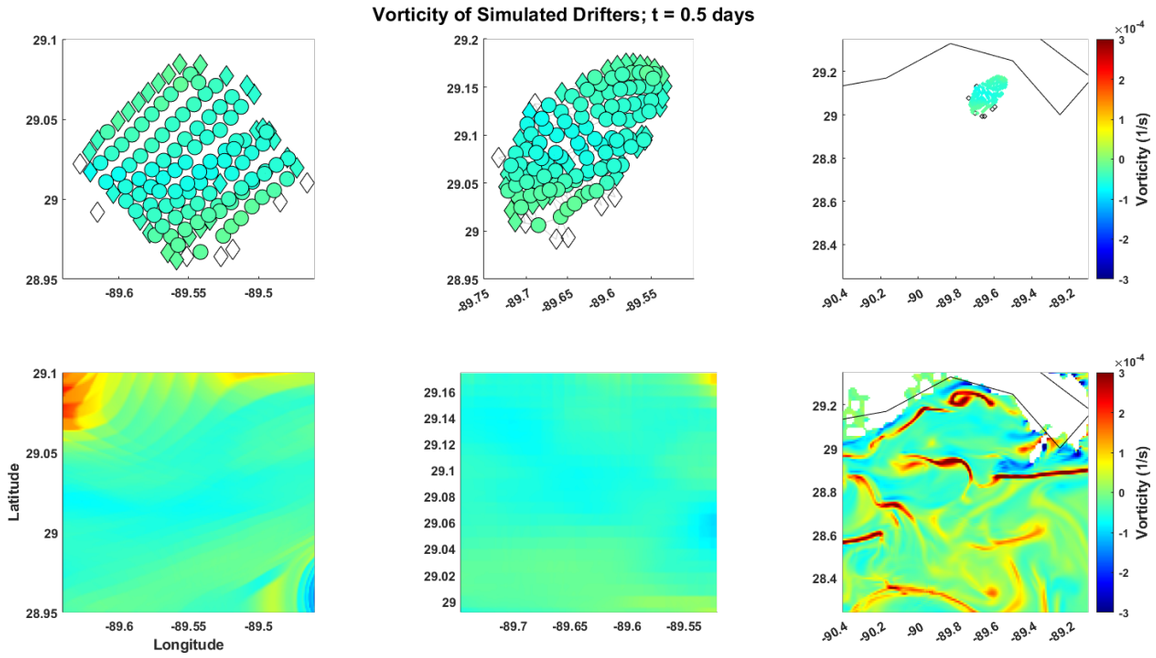

Figure 2-44: Vorticity field for results from simulated drifters (top row) and from a grid with spacing of .001 degrees (bottom row) at time $t = 0.5$. Results in the left column (top left and bottom left) are shown as a function of initial position. Results in the middle and right columns are shown as a function of current position at the integration time.

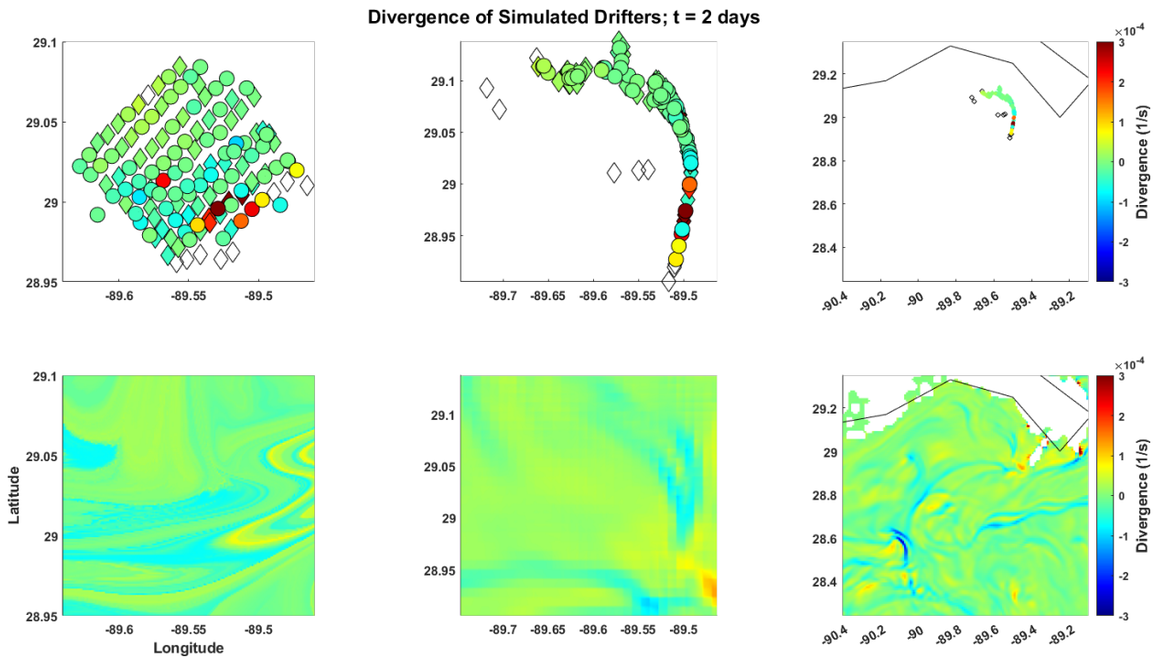

Figure 2-45: Same as Figure 2-43 except for $t = 2$ days.

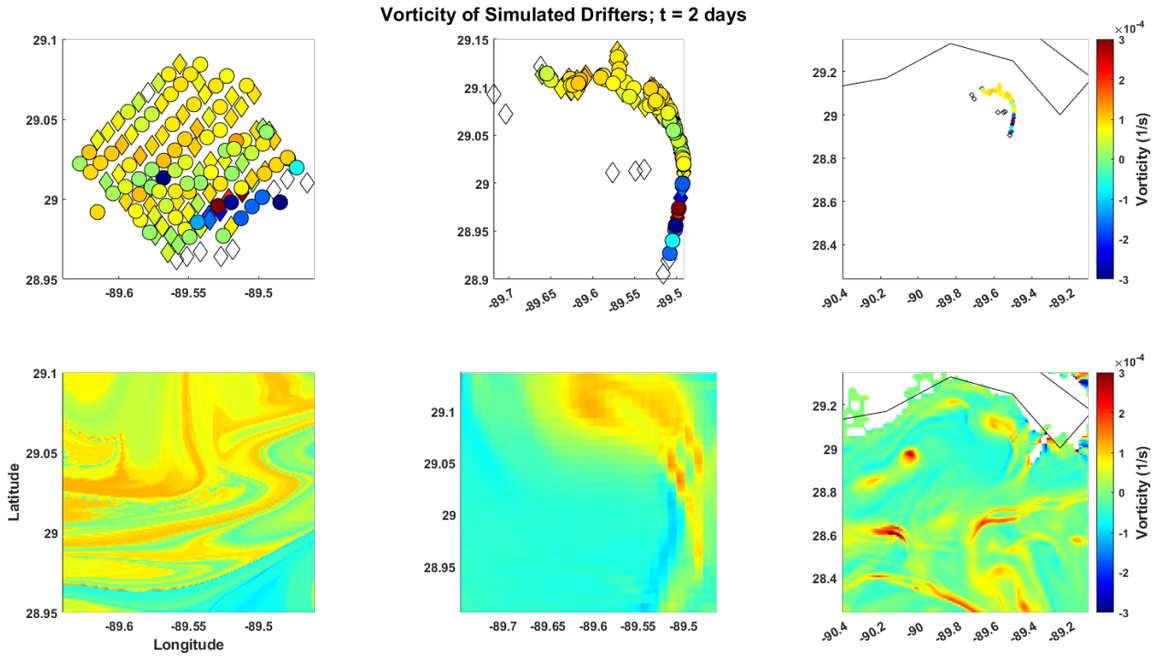

Figure 2-46: Same as Figure 2-44 except for $t = 2$ days.

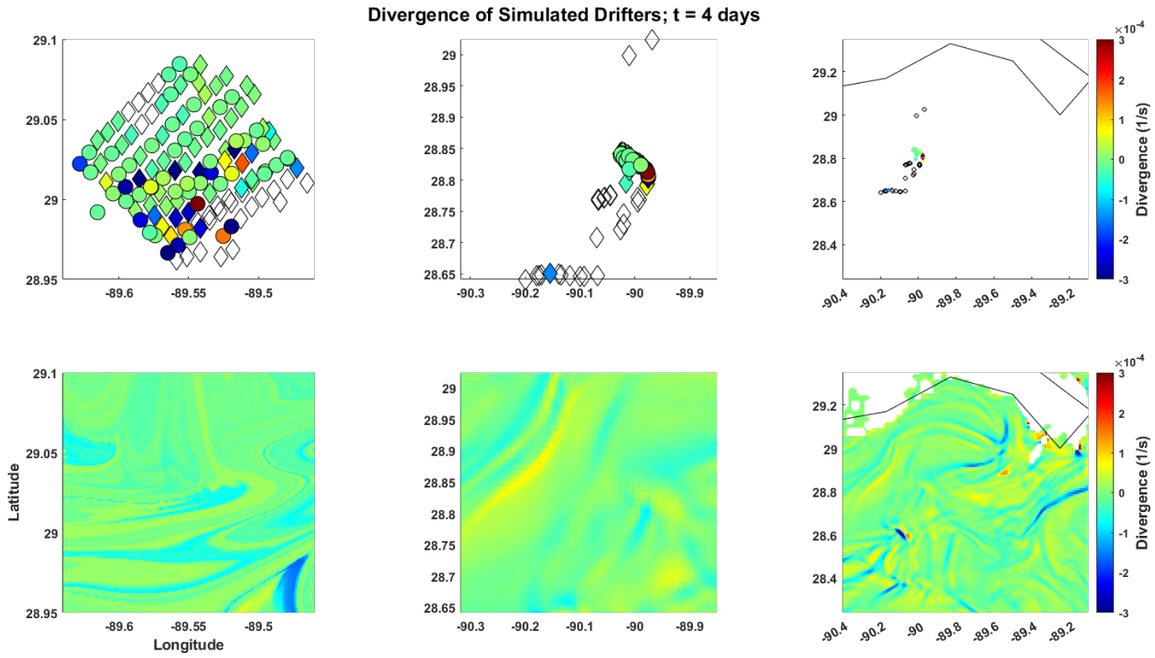

Figure 2-47: Same as Figure 2-43 except for $t = 4$ days.

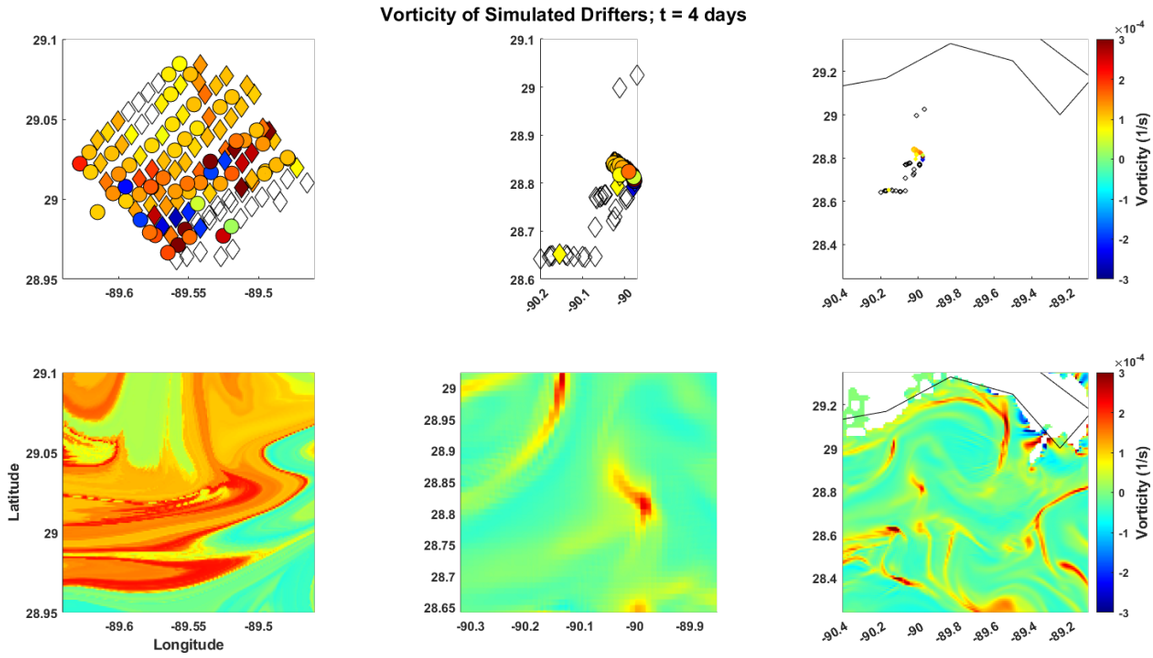

Figure 2-48: Same as Figure 2-44 except for $t = 4$ days.

2.4.6 Dilation

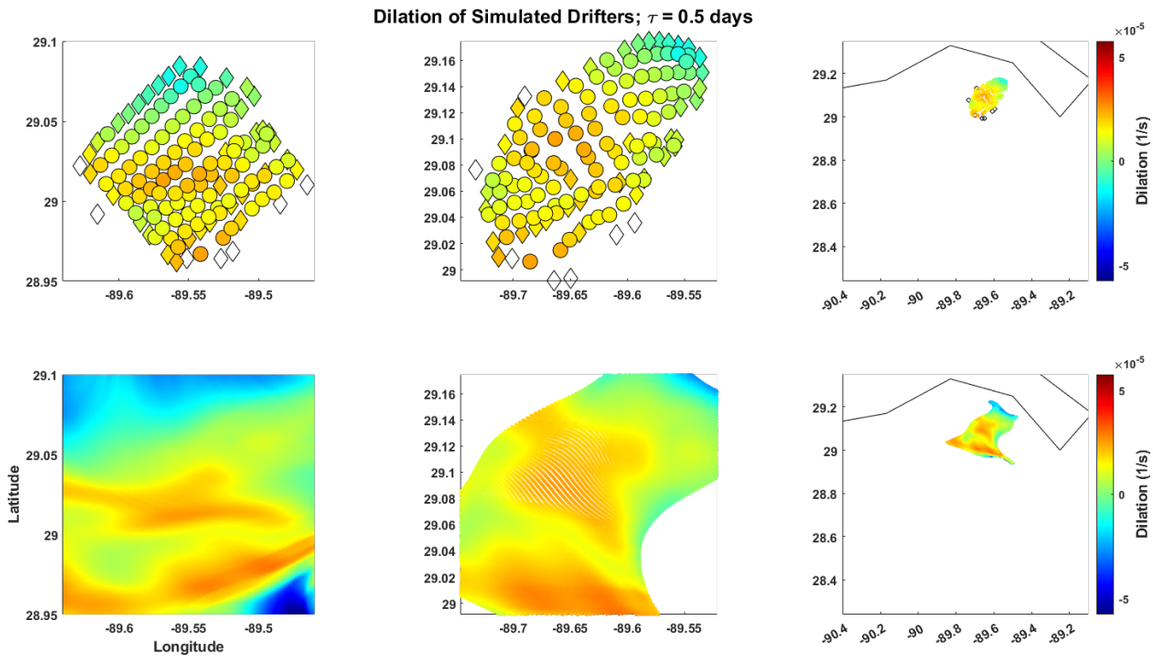

Figure 2-49: Dilation field for results from simulated drifters (top row) and from a grid with spacing of .001 degrees (bottom row) with integration time $\tau = 0.5$. Results in the left column (top left and bottom left) are shown as a function of initial position. Results in the middle and right columns are shown as a function of current position at the integration time.

Dilation reveals similar structure compared to all previously shown metrics. For instance, the separation between drifters which begin heading north at the coast and those which head south can be seen as relatively large positive values at the center of the drifter distribution (as well as the center of the dense grid) at $\tau = 0.5$, as seen in Figure 2-49. At larger times like $\tau = 2$ and 4 days, the initial divergence becomes outweighed by convergence, causing dilation to be overall negative (Figures 2-35 and 2-36). This is consistent with the small and negative FTLE values spanning much of the domain at long integration time such as in

Figure 2-33. There is minimal change in the dilation field between $\tau = 2$ and 4, except that features such as the s-shaped trough become more well-defined. Regimes with very negative dilation values such as those which dominate the domain (and are particularly strong for the s-shaped feature) may indicate that parcels beginning in these areas pass through regions of strong downwelling. There is generally good correspondence between values estimated from simulated drifters and the dense-grid values, but drifter estimates become noisy as the results become "unreliable" (i.e. meet the less strict criteria for divergence computation), as represented by the diamonds in Figure 2-51.

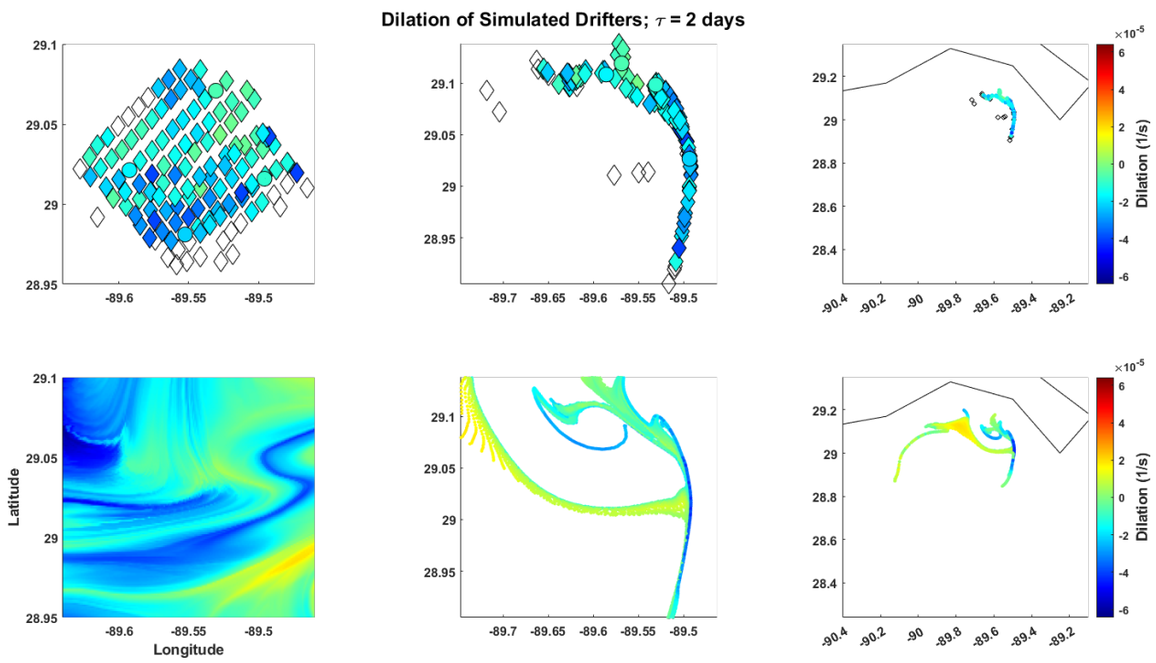

Figure 2-50: Same as Figure 2-49 except for $\tau = 2$ days.

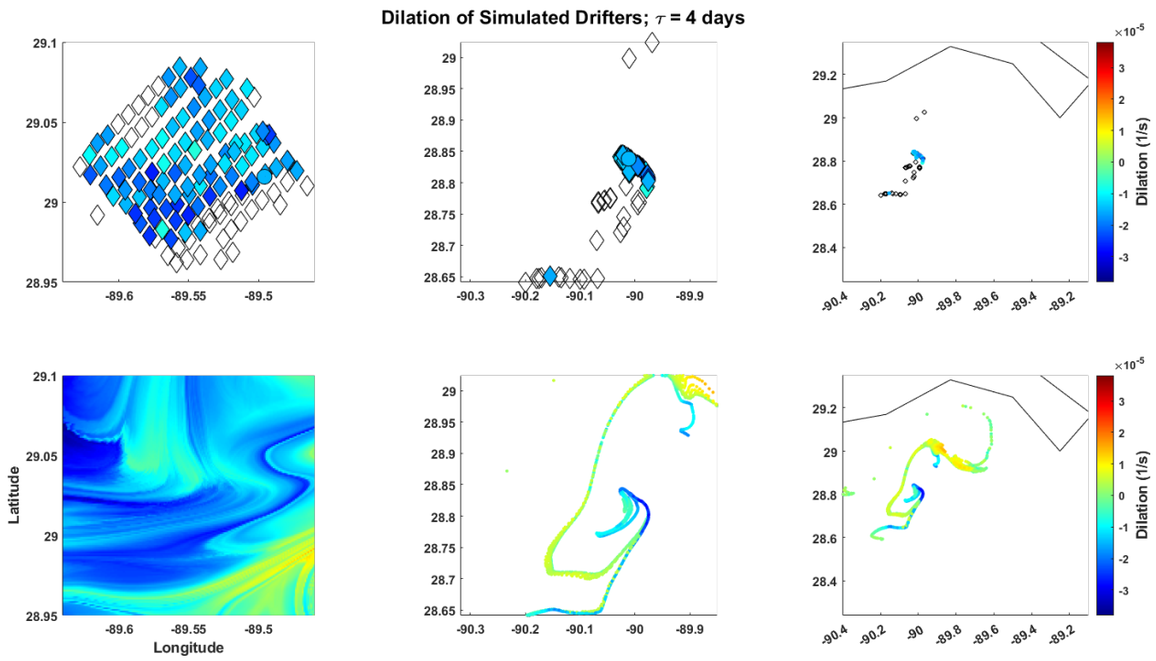

Figure 2-51: Same as Figure 2-49 except for $\tau = 4$ days.

2.4.7 Lagrangian-Averaged Vorticity Deviation

LAVD results in the dense grid of trajectories do not reveal maximal "tubular" features, meaning no Lagrangian eddies were detected in the flow. LAVD estimates from simulated drifters generally agree well with estimates from the dense grid, which is consistent with the analysis of drifter-based vorticity. A curve of high LAVD values can be seen at $\tau = 2$ and 4 days, roughly corresponding to the similar ridge seen at shorter FTLE integration times. The s-shaped feature also appears again as a minimal LAVD surface.

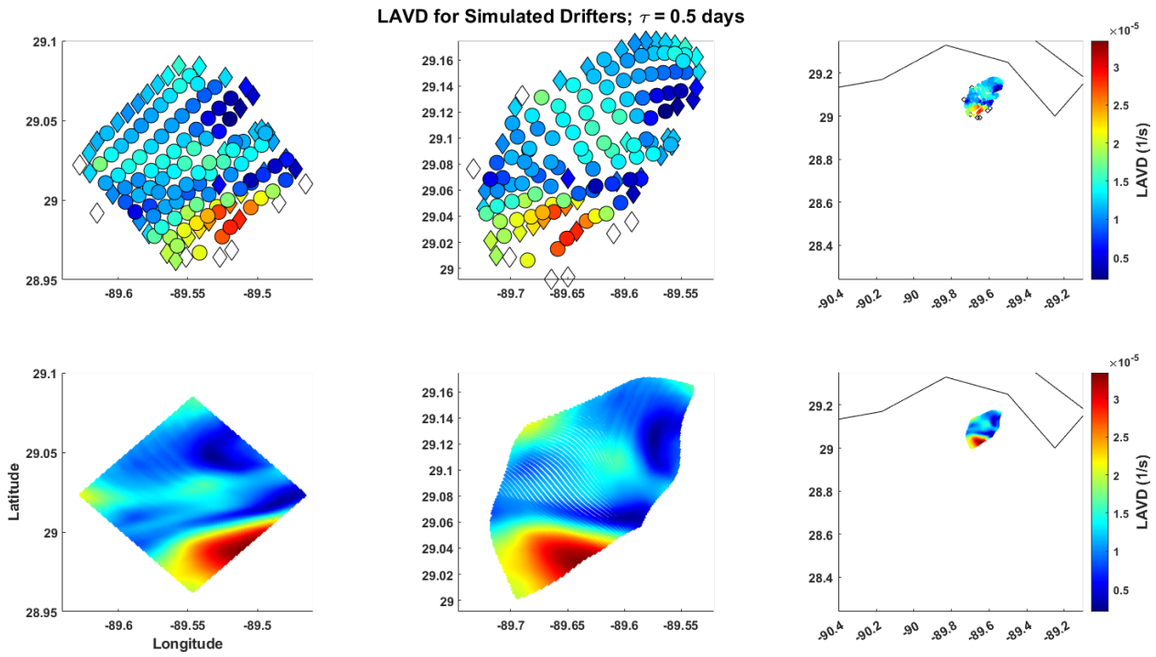

Figure 2-52: LAVD field for results from simulated drifters (top row) and from a grid with spacing of .001 degrees (bottom row) with integration time $\tau = 0.5$. The dense grid has now been confined to a diamond-shape, encompassing the domain formed by simulated drifters. Results in the left column (top left and bottom left) are shown as a function of initial position. Results in the middle and right columns are shown as a function of current position at the integration time.

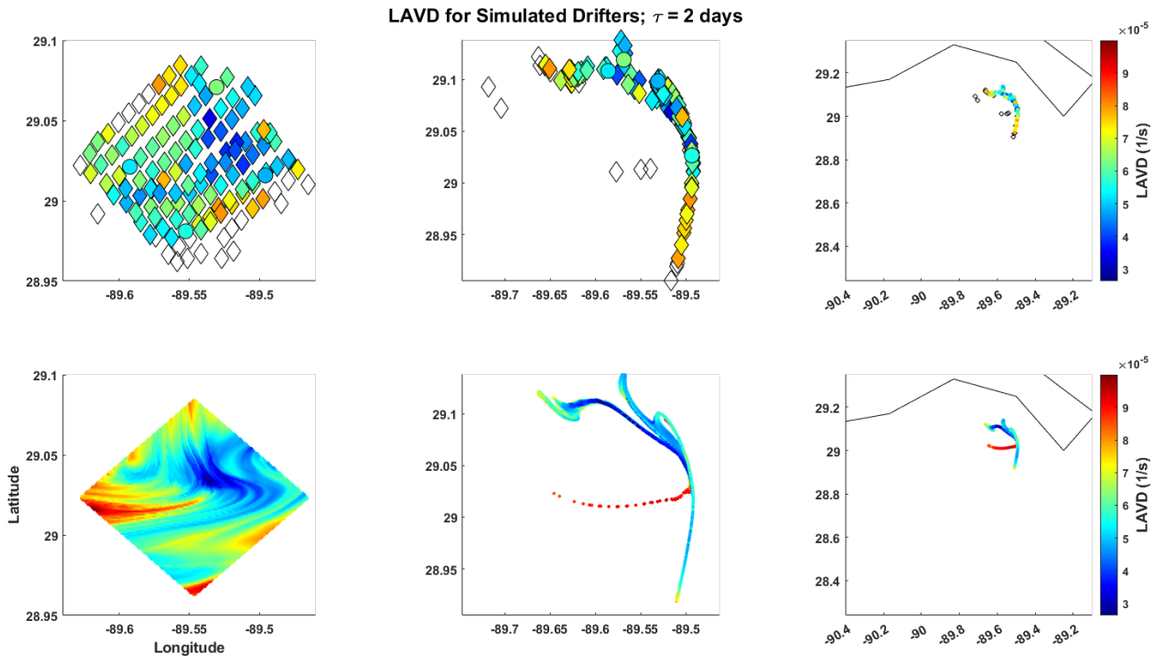

Figure 2-53: Same as Figure 2-52 except for $\tau = 2$ days.

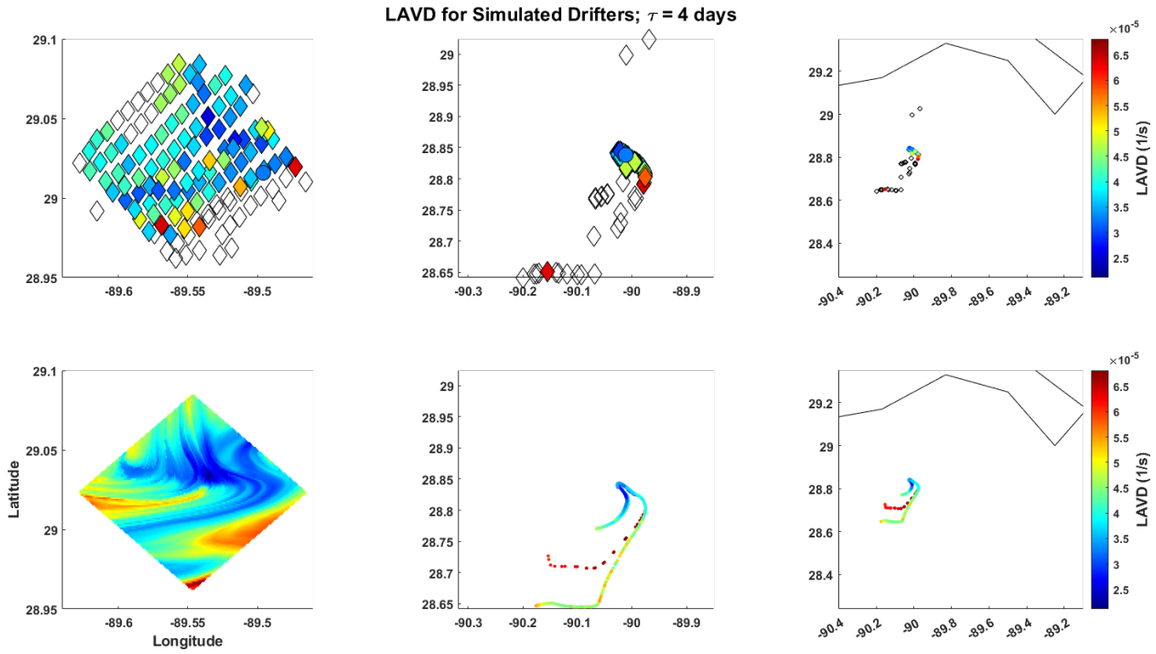

Figure 2-54: Same as Figure 2-52 except for $\tau = 4$ days.

2.4.8 Spectral Clustering of Trajectories

Figures 2-55 through 2-60 show spectral clustering results for simulated drifters. Results are shown for all local maxima in the normalized spectral eigengap distribution. For the case of $\tau = 0.5$ days, only one peak was identified. For $\tau = 2$ days, two peaks were identified, and for $\tau = 4$ days, three peaks were identified.

Much like real drifters, results at short times are not particularly meaningful, since drifters have not experienced much coherent separation. For $\tau = 2$ days, the two r values are relatively close (15.3 km and 18.5 km) and so they produce similar results. Primarily, they both separate drifters which began in the northern/southern parts of the domain (which later head northward or southward as they approach the coast). The larger sparsification radius allows for a few of the isolated drifters to be included in the southern cluster of drifters, whereas the smaller radius identified these drifters as separate clusters. For $\tau = 4$ days, the smallest r separated drifters primarily into a cluster of drifters that has been pushed further south than all other drifters, and set of drifters in the center of the distribution. Three other small clusters were also identified. For slightly larger r of 9.3 km, the southernmost drifters are now split into two clusters, while the center cluster remains. Three isolated trajectories were also determined as separate clusters. For the largest r of 19 km, drifters were separated primarily into two clusters. Interestingly, the clusters are now separated in the initial-positions domain. The boundary separating the two dominant clusters appear to coincide with the FTLE ridges of Figures 2-32. Once again, the two isolated trajectories were determined to be within their own clusters.

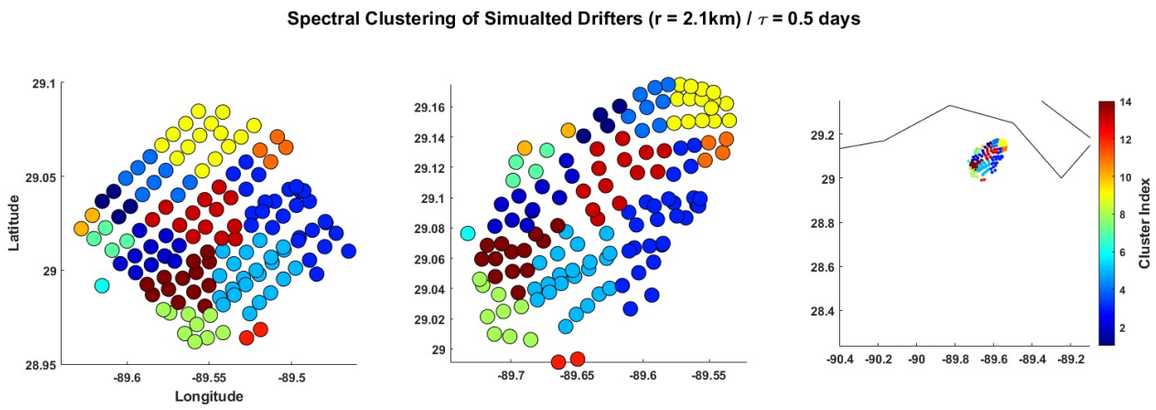

Figure 2-55: Spectral clusters field for results from simulated drifters. Left panel results are shown as a function of initial position. Results in the middle and right panels are shown as a function of current position at the integration time.

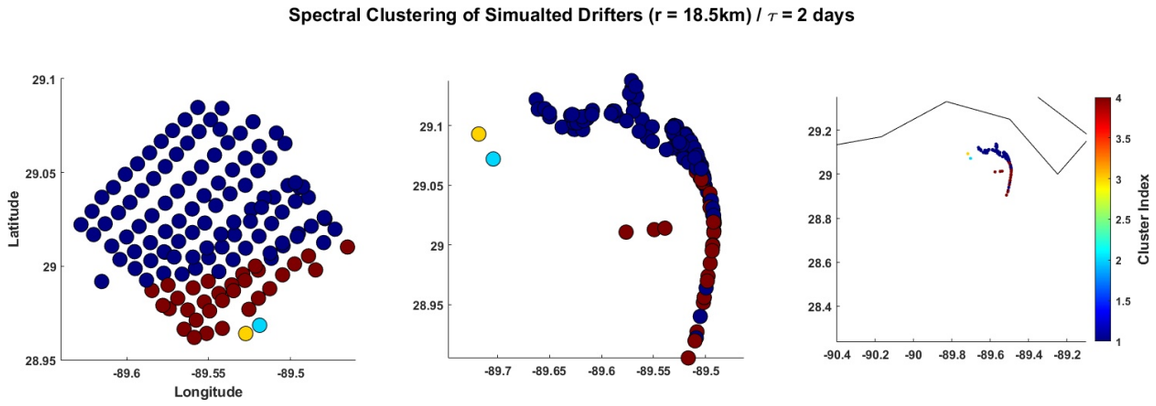

Figure 2-56: Same as Figure 2-55 except for $\tau = 2$ days, with $r = 18.5$ km.

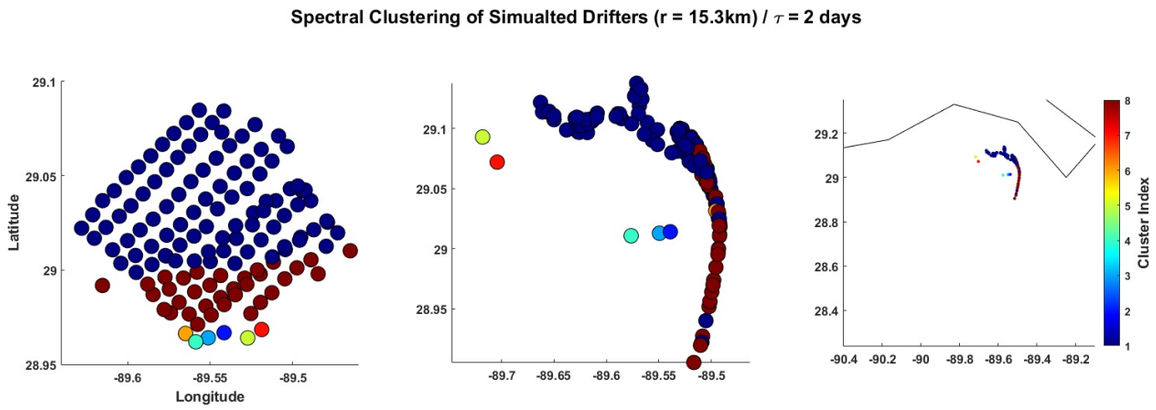

Figure 2-57: Same as Figure 2-55 except for $\tau = 2$ days, with $r = 15.3$ km.

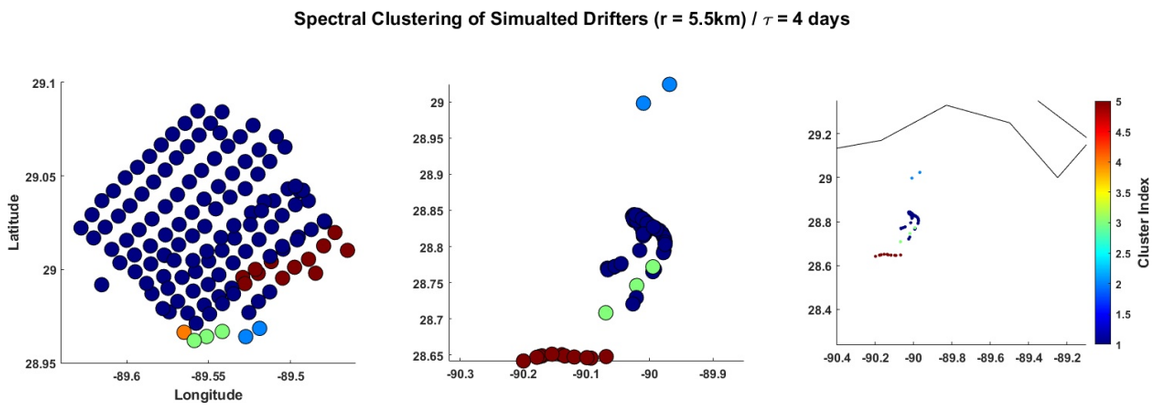

Figure 2-58: Same as Figure 2-55 except for $\tau = 4$ days, with $r = 5.5$ km.

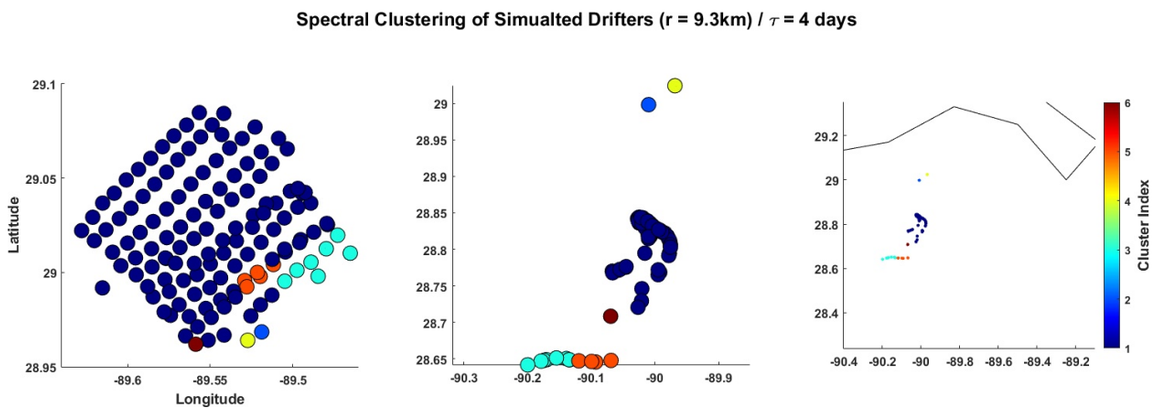

Figure 2-59: Same as Figure 2-55 except for $\tau = 4$ days, with $r = 9.3$ km.

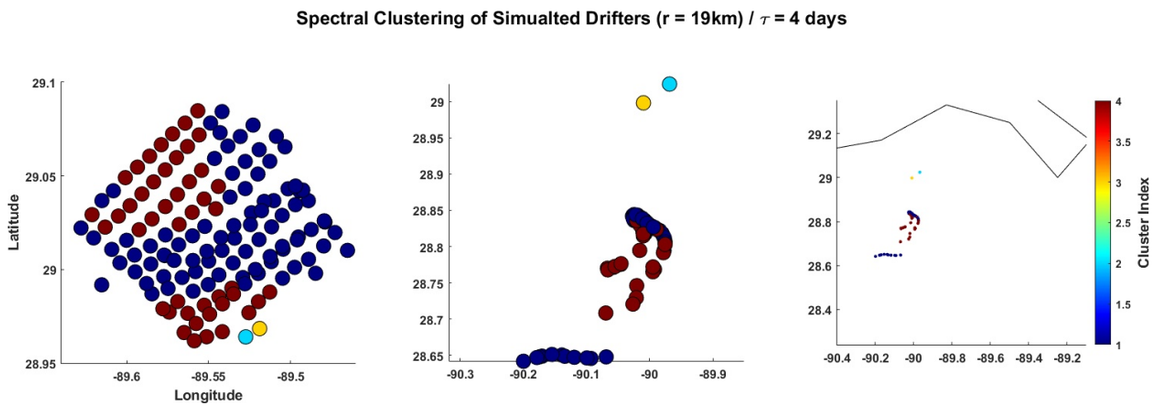

Figure 2-60: Same as Figure 2-55 except for $\tau = 4$ days, with $r = 19$ km.

2.5 Discussion

In this chapter, an array of 135 drifters released in a nearly gridded pattern were used to identify Lagrangian coherent structures using a variety of diagnostics. This study is the first attempt to apply these dynamical systems techniques to an array of real drifters. All methods provided insight into drifter behavior for both real and simulated drifters that were not always obvious by observing trajectories alone.

Similar features of the flow field were often identified throughout multiple diagnostics, such as separation or convergence of trajectories, strong rotational features, and other boundaries between clusters of drifters with distinct behavior. FTLEs, arc-length, correlation dimension, encounter number, and dilation were particularly useful for identifying the separation between drifters that headed northward or southward as they approached the coast, as well as other instances of separation or convergence. LAVD emphasized regions where rotational features were particularly prevalent.

Generally, good agreement existed between the Lagrangian diagnostic fields of simulated drifters in NCOM and gridded trajectories in NCOM for the same release area. Distinct

features such as ridges in the true FTLE and encounter number fields were also revealed in the fields of simulated drifters. These results are promising and reveal that analysis of Lagrangian coherent structures may be feasible in future drifter experiments. While this experiment was constrained to the surface, future experiments might involve drifters drogued at other depths such as in Chapter 1, so that LCSs can be approximated for deeper depths or in three dimensions.

Unlike other diagnostics, FTLEs involve differentiation of initial and final locations of trajectories. This quality allows for FTLEs to be estimated "between" initial positions using the standard method in addition to using the unstructured-grid method at actual drifter locations. This allows for a more densely-filled FTLE field in the domain where drifters were released. In such a field, sharper features can be distinguished compared to the sparser results from other metrics. This makes FTLEs fields potentially more useful for sparse sets of drifter trajectories.

Despite the theoretical connection between arc-length and stable manifolds, distinct features were difficult to detect as distinct curves in the arc-length fields from drifters. While trajectory arc-length visually categorizes trajectories into different regimes, the meaning of the boundaries of these regimes is often difficult to interpret. Correlation dimension, while similar to arc-length, often over-stated the presence of certain categories in the flow field, making results difficult to understand separate. CD was also the most computationally expensive diagnostic among those tested in this Chapter, often requiring lower resolution grids for computation in a reasonable amount of time.

Dilation and LAVD estimations were challenging due to the difficulty of computing divergence and vorticity at drifter locations for long time intervals. As drifters travel throughout the domain, the positions of drifters relative to each other do not always allow for reliable estimation of divergence or vorticity. Further, much of the same information from dilation and LAVD can be inferred from FTLEs or encounter number.

Spectral clustering techniques often led to surprising results that were sometimes, but not always, related to features revealed in other diagnostics. For example, it often grouped trajectories together which are separarted in the initial-positions domain but not the final-positions domain, or vice versa. The similarity among these clusters is not always evident when observing results from other diagnostics, and could be studied further to determine the causes of their similar behavior. In at least one case, the spectral clustering technique was

particularly effective for identifying a stable manifold that was also revealed within FTLEs for simulated drifters.

After experimenting with these diagnostics, the author finds FTLEs to provide the most complete information about the flow at multiple time scales. For instance, FTLEs capture the same convergence and separation among trajectories that are detected in dilation and encounter number. They also generally categorize the flow into the same flow regimes as arc-length and correlation dimension, but with more clarity. Even rotational features revealed by LAVD fields are also related to certain convergence regions in the FTLE field (though this may not be the case for other fields).

Bibliography

Corinne Alberola, Stéphan Rousseau, Claude Millot, Mario Astraldi, Jesus García-Lafuente, Gian-Petro Gasparini, Uwe Send, and Annick Vangriesheim. Tidal currents in the western mediterranean-sea, 1995. URL https://archimer.ifremer.fr/doc/00097/20777/. Number: 2 Pages: 273-284 Type: Article Volume: 18.

Changsheng Chen, Ruixiang Li, Larry Pratt, Richard Limeburner, Robert C. Beardsley, Amy Bower, Houshuo Jiang, Yasser Abualnaja, Qichun Xu, Huichan Lin, Xuehai Liu, Jian Lan, and Taewan Kim. Process modeling studies of physical mechanisms of the formation of an anticyclonic eddy in the central Red Sea. *Journal of Geophysical Research: Oceans*, 119(2):1445–1464, February 2014. ISSN 21699275. doi: 10.1002/2013JC009351. URL http://doi.wiley.com/10.1002/2013JC009351.

Eric A. D'Asaro, Daniel F. Carlson, Marcelo Chamecki, Ramsey R. Harcourt, Brian K. Haus, Baylor Fox-Kemper, M. Jeroen Molemaker, Andrew C. Poje, and Di Yang. Advances in observing and understanding small-scale open ocean circulation during the gulf of mexico research initiative era. *Frontiers in Marine Science*, 7:349, 2020. ISSN 2296-7745. doi: 10.3389/fmars.2020.00349. URL https://www.frontiersin.org/article/10.3389/fmars.2020.00349.

John A. Dutton. *The ceaseless wind: An introduction to the theory of atmospheric motion*. Courier Corporation, 2002.

James B. Edson, Venkata Jampana, Robert A. Weller, Sebastien P. Bigorre, Albert J. Plueddemann, Christopher W. Fairall, Scott D. Miller, Larry Mahrt, Dean Vickers, and Hans Hersbach. On the exchange of momentum over the open ocean. *Journal of Physical Oceanography*, 43(8):1589 – 1610, 2013. doi: 10.1175/JPO-D-12-0173.1. URL https://journals.ametsoc.org/view/journals/phoc/43/8/jpo-d-12-0173.1.xml. Publisher: American Meteorological Society tex.address: Boston MA, USA.

B. Efron. Bootstrap methods: Another look at the jackknife. *The Annals of Statistics*, 7(1):1 – 26, 1979. doi: 10.1214/aos/1176344552. URL https://doi.org/10.1214/aos/1176344552. Publisher: Institute of Mathematical Statistics.

Sebastian Essink. Lagrangian Dispersion and Deformation in Submesoscale Flows. page 124, 2019.

Margaux Filippi, Irina I. Rypina, Alireza Hadjighasem, and Thomas Peacock. An optimized-parameter spectral clustering approach to coherent structure detection in geophysical flows. *Fluids*, 6(1), 2021. ISSN 2311-5521. doi: 10.3390/fluids6010039. URL https://www.mdpi.com/2311-5521/6/1/39. tex.article-number: 39.

Gary Froyland and Kathrin Padberg-Gehle. A rough-and-ready cluster-based approach for extracting finite-time coherent sets from sparse and incomplete trajectory data. *Chaos: An Interdisciplinary Journal of Nonlinear Science*, 25(8):087406, 2015. doi: 10.1063/1.4926372. URL https://doi.org/10.1063/1.4926372. tex.eprint: https://doi.org/10.1063/1.4926372.

Máximo Garcia-Jove, Baptiste Mourre, Pierre Lermusiaux, Nikolaos Zarokanellos, Alex Santana, Jaime Hernandez-Lahseras, Patrick Haley Jr., Chris Mirabito, Eugenio Cutolo, John Allen, and Joaquin Tintoré. Scale-dependency of vertical velocities in the Alboran Sea through high-resolution simulations and glider observations., 2020.

Alireza Hadjighasem, Daniel Karrasch, Hiroshi Teramoto, and George Haller. Spectral-clustering approach to Lagrangian vortex detection. *Physical Review E*, 93(6):063107, June 2016. doi: 10.1103/PhysRevE.93.063107. URL https://link.aps.org/doi/10.1103/PhysRevE.93.063107. Number of pages: 17 Publisher: American Physical Society.

George Haller. Lagrangian coherent structures from approximate velocity data. *Physics of Fluids*, 14(6):1851–1861, 2002. doi: 10.1063/1.1477449. URL https://doi.org/10.1063/1.1477449. tex.eprint: https://doi.org/10.1063/1.1477449.

George Haller. Lagrangian coherent structures. *Annual Review of Fluid Mechanics*, 47(1):137–162, 2015. doi: 10.1146/annurev-fluid-010313-141322. URL https://doi.org/10.1146/annurev-fluid-010313-141322. tex.eprint: https://doi.org/10.1146/annurev-fluid-010313-141322.

George Haller, Alireza Hadjighasem, Mohammad Farazmand, and Florian Huhn. Defining coherent vortices objectively from the vorticity. *Journal of Fluid Mechanics*, 795:136–173, 2016. doi: 10.1017/jfm.2016.151. Publisher: Cambridge University Press.

Angelique C. Haza, Tamay M. Özgökmen, Annalisa Griffa, Andrew C. Poje, and M.-Pascale Lelong. How Does Drifter Position Uncertainty Affect Ocean Dispersion Estimates? *Journal of Atmospheric and Oceanic Technology*, 31(12):2809–2828, December 2014. ISSN 0739-0572, 1520-0426. doi: 10.1175/JTECH-D-14-00107.1. URL http://journals.ametsoc.org/doi/10.1175/JTECH-D-14-00107.1.

Jaime Hernandez-Lasheras and Baptiste Mourre. Dense CTD survey versus glider fleet sampling: comparing data assimilation performance in a regional ocean model west of Sardinia. *Ocean Science*, 14(5):1069–1084, 2018. doi: 10.5194/os-14-1069-2018. URL https://os.copernicus.org/articles/14/1069/2018/.

James R. Holton and Gregory J. Hakim. *An introduction to dynamic meteorology*. Academic Press, Amsterdam, fifth edition edition, 2013. ISBN 978-0-12-384866-6.

Brian J. Hoskins. The mathematical theory of frontogenesis. *Annual Review of Fluid Mechanics*, 14(1):131–151, 1982. doi: 10.1146/annurev.fl.14.010182.001023. URL https://doi.org/10.1146/annurev.fl.14.010182.001023. tex.eprint: https://doi.org/10.1146/annurev.fl.14.010182.001023.

Helga S. Huntley, B. L. Lipphardt, Gregg Jacobs, and A. D. Kirwan. Clusters, deformation, and dilation: Diagnostics for material accumulation regions. *Journal of Geophysical Research: Oceans*, 120(10):6622–6636, October 2015. ISSN 2169-9275, 2169-9291. doi: 10.1002/2015JC011036. URL https://onlinelibrary.wiley.com/doi/10.1002/2015JC011036.

Melanie Juzà, Baptiste Mourre, Lionel Renault, S. Gómara, Kristian Sebastián, Sebastian Lora, Joan Pau Beltrán, B Frontera, B. Garau, C. Troupin, M. Torner, E. Heslop, B. Casas, Romain Escudier, G. Vizoso, and Joaquín Tintoré. SOCIB operational ocean forecasting system and multi-platform validation in the Western Mediterranean Sea. *Journal of Operational Oceanography*, 9(sup1):s155–s166, 2016. doi: 10.1080/1755876X.2015.1117764. URL https://doi.org/10.1080/1755876X.2015.1117764. Publisher: Taylor & Francis tex.eprint: https://doi.org/10.1080/1755876X.2015.1117764.

Igor Kamenkovich, Irina I. Rypina, and Pavel Berloff. Properties and origins of the anisotropic eddy-induced transport in the north atlantic. *Journal of Physical Oceanography*, 45(3):778 – 791, 2015. doi: 10.1175/JPO-D-14-0164.1. URL https://journals.ametsoc.org/view/journals/phoc/45/3/jpo-d-14-0164.1.xml. Publisher: American Meteorological Society tex.address: Boston MA, USA.

Albert D. Kirwan and M-S. Chang. Effect of sampling rate and random position error on analysis of drifter data. *Journal of Physical Oceanography*, 9(2):382 – 387, 1979. doi: 10.1175/1520-0485(1979)009¡0382:EOSRAR¿2.0.CO;2. Publisher: American Meteorological Society tex.address: Boston MA, USA.

Francois Lekien and Shane D. Ross. The computation of finite-time Lyapunov exponents on unstructured meshes and for non-Euclidean manifolds. *Chaos: An Interdisciplinary Journal of Nonlinear Science*, 20(1):017505, 2010. doi: 10.1063/1.3278516. URL https://doi.org/10.1063/1.3278516. tex.eprint: https://doi.org/10.1063/1.3278516.

Carlos Lopesino, Francisco Balibrea-Iniesta, Víctor J. García-Garrido, Stephen Wiggins, and Ana M. Mancho. A theoretical framework for lagrangian descriptors. *International Journal of Bifurcation and Chaos*, 27(01):1730001, 2017. doi: 10.1142/S0218127417300014. URL https://doi.org/10.1142/S0218127417300014. tex.eprint: https://doi.org/10.1142/S0218127417300014.

Ana M. Mancho, Stephen Wiggins, Jezabel Curbelo, and Carolina Mendoza. Lagrangian descriptors: A method for revealing phase space structures of general time dependent dynamical systems. *Communications in Nonlinear Science and Numerical Simulation*, 18 (12):3530–3557, 2013. ISSN 1007-5704. doi: https://doi.org/10.1016/j.cnsns.2013.05.002. URL https://www.sciencedirect.com/science/article/pii/S1007570413002037.

Carolina Mendoza and Ana M. Mancho. Hidden geometry of ocean flows. *Physical Review Letters*, 105(3):038501, July 2010. doi: 10.1103/PhysRevLett.105.038501. URL https://link.aps.org/doi/10.1103/PhysRevLett.105.038501. Number of pages: 4 Publisher: American Physical Society.

Robert L. Molinari and Albert D. Kirwan. Calculations of differential kinematic properties from lagrangian observations in the western caribbean sea. *Journal of Physical Oceanography*, 5(3):483 – 491, 1975. doi: 10.1175/1520-0485(1975)005¡0483:CODKPF¿2.0.CO;2. Publisher: American Meteorological Society tex.address: Boston MA, USA.

Baptiste Mourre, Eva Aguiar, Mélanie Juza, Jaime Hernandez-Lasheras, Emma Reyes, Emma Heslop, Romain Escudier, Eugenio Cutolo, Simon Ruiz, Evan Mason, Ananda Pascual, and Joaquin Tintoré. Assessment of High-Resolution Regional Ocean Prediction Systems Using Multi-Platform Observations: Illustrations in the Western Mediterranean Sea. In Eric P. Chassignet, Ananda Pascual, Joaquin Tintoré, and Jacques Verron, editors, *New Frontiers in Operational Oceanography*. GODAE OceanView, August 2018. ISBN 978-1-72054-997-0. doi: 10.17125/gov2018.ch24. URL http://purl.flvc.org/fsu/fd/FSU$_l ibsubv1_s cholarship_s ubmission_1536246976_5338033b$.

J. Carter Ohlmann, Peter F. White, Andrew L. Sybrandy, and P. Peter Niiler. GPS Cellular drifter technology for coastal ocean observing systems. *Journal of Atmospheric and Oceanic Technology*, 22(9):1381 – 1388, 2005. doi: 10.1175/JTECH1786.1. URL https://journals.ametsoc.org/view/journals/atot/22/9/jtech1786.xml. Publisher: American Meteorological Society tex.address: Boston MA, USA.

Joseph Pedlosky. *Geophysical Fluid Dynamics*, volume 710. Springer, New York, 1987.

Irina I. Rypina and Lawrence J. Pratt. Trajectory encounter volume as a diagnostic of mixing potential in fluid flows. *Nonlinear Processes in Geophysics*, 24(2):189–202, 2017. doi: 10.5194/npg-24-189-2017. URL https://npg.copernicus.org/articles/24/189/2017/.

Irina I. Rypina, S. E. Scott, Lawrence J. Pratt, and Michael G. Brown. Investigating the connection between complexity of isolated trajectories and Lagrangian coherent structures. *Nonlinear Processes in Geophysics*, 18(6):977–987, 2011. doi: 10.5194/npg-18-977-2011. URL https://npg.copernicus.org/articles/18/977/2011/.

Irina I. Rypina, Igor Kamenkovich, Pavel Berloff, and Lawrence J. Pratt. Eddy-induced particle dispersion in the near-surface north atlantic. *Journal of Physical Oceanography*, 42(12):2206 – 2228, 2012. doi: 10.1175/JPO-D-11-0191.1. URL https://journals.ametsoc.org/view/journals/phoc/42/12/jpo-d-11-0191.1.xml. Publisher: American Meteorological Society tex.address: Boston MA, USA.

Irina I. Rypina, A. R. Kirincich, R. Limeburner, and I. A. Udovydchenkov. Eulerian and lagrangian correspondence of high-frequency radar and surface drifter data: Effects of radar resolution and flow components. *Journal of Atmospheric and*

Oceanic Technology, 31(4):945 – 966, 2014. doi: 10.1175/JTECH-D-13-00146.1. URL https://journals.ametsoc.org/view/journals/atot/31/4/jtech-d-13-00146.xml. Publisher: American Meteorological Society tex.address: Boston MA, USA.

Irina I. Rypina, Anthony R Kirincich, Steven J. Lentz, and Miles A. Sundermeyer. Investigating the eddy diffusivity concept in the coastal ocean. *Journal of Physical Oceanography*, 46(7):2201 – 2218, 2016. doi: 10.1175/JPO-D-16-0020.1. URL https://journals.ametsoc.org/view/journals/phoc/46/7/jpo-d-16-0020.1.xml. Publisher: American Meteorological Society tex.address: Boston MA, USA.

Irina I. Rypina, S. G. Llewellyn Smith, and Lawrence J. Pratt. Connection between encounter volume and diffusivity in geophysical flows. *Nonlinear Processes in Geophysics*, 25(2):267–278, 2018. doi: 10.5194/npg-25-267-2018. URL https://npg.copernicus.org/articles/25/267/2018/.

Shawn C. Shadden, Francois Lekien, and Jerrold E. Marsden. Definition and properties of Lagrangian coherent structures from finite-time Lyapunov exponents in two-dimensional aperiodic flows. *Physica D: Nonlinear Phenomena*, 212(3):271–304, 2005. ISSN 0167-2789. doi: https://doi.org/10.1016/j.physd.2005.10.007. URL https://www.sciencedirect.com/science/article/pii/S0167278905004446.

Jianbo Shi and Jitendra Malik. Normalized cuts and image segmentation. *IEEE Transactions on Pattern Analysis and Machine Intelligence*, 22(8):888–905, 2000. doi: 10.1109/34.868688.

Matthew S. Spydell, Falk Feddersen, and Jamie Macmahan. The effect of drifter GPS errors on estimates of submesoscale vorticity. *Journal of Atmospheric and Oceanic Technology*, 36(11):2101 – 2119, 2019. doi: 10.1175/JTECH-D-19-0108.1. URL https://journals.ametsoc.org/view/journals/atot/36/11/jtech-d-19-0108.1.xml. Publisher: American Meteorological Society tex.address: Boston MA, USA.

Mohamed H.M. Sulman, Helga S. Huntley, B.L. Lipphardt, and lbert D. Kirwan. Leaving flatland: Diagnostics for Lagrangian coherent structures in three-dimensional flows. *Physica D: Nonlinear Phenomena*, 258:77–92, 2013. ISSN 0167-2789. doi: https://doi.org/10.1016/j.physd.2013.05.005. URL https://www.sciencedirect.com/science/article/pii/S0167278913001450.

Daniel R. Tarry, Sebastian Essink, Ananda Pascual, Simón Ruiz, Pierre-Marie Poulain, Tamay Özgökmen, Luca R. Centurioni, J. Thomas Farrar, Andrey Shcherbina, Amala Mahadevan, and Eric D'Asaro. Frontal convergence and vertical velocity measured by drifters in the alboran sea. *Journal of Geophysical Research: Oceans*, 126(4):e2020JC016614, 2021. doi: https://doi.org/10.1029/2020JC016614. URL https://agupubs.onlinelibrary.wiley.com/doi/abs/10.1029/2020JC016614. tex.eprint: https://agupubs.onlinelibrary.wiley.com/doi/pdf/10.1029/2020JC016614.

Joaquín Tintoré, Guillermo Vizoso, Benjamín Casas, Emma Heslop, Ananda Pascual, Alejandro Orfila, Simón Ruiz, Miguel Martínez-Ledesma, Marc Torner, Simó Cusí, Amy Diedrich, Pau Balaguer, Lluís Gómez-Pujol, Amaya Avarez-Ellacuria, Sonia Gómara, Kristian Sebastian, Sebastián Lora, Joan Pau Beltrán, Lionel Renault, Melanie Juzà, Diego Luna Álvarez, David March, Bartomeu Garau, Carlos Castilla, Tomeu Cañellas, David Roque, Irene Lizarán, Saul Pitarch, Maria Antonia Carrasco, Aránzazu Lana, Evan Mason, Romain Escudier, Daniel Conti, Juan Manuel Sayol, Bàrbara Barceló, Francisco Alemany, Patricia Reglero, Enric Massuti, Pedro Vélez-Belchí, Javier Ruiz, Temel Oguz, Marta Gómez, Enrique Alvarez, Luís Ansorena, and Mario Manriquez. SOCIB: The balearic islands coastal ocean observing and forecasting system responding to science, technology and society needs. *Marine Technology Society Journal*, 47:101–113, 2013.

Guilherme S. Vieira and Michael R. Allshouse. Internal wave boluses as coherent structures in a continuously stratified fluid. *Journal of Fluid Mechanics*, 885:A35, 2020. doi: 10.1017/jfm.2019.993. Publisher: Cambridge University Press.

Ulrike von Luxburg. A tutorial on spectral clustering. *Statistics and Computing*, 17 (4):395–416, December 2007. ISSN 1573-1375. doi: 10.1007/s11222-007-9033-z. URL https://doi.org/10.1007/s11222-007-9033-z.

Stephen Wiggins. The Dynamical Systems Approach to Lagrangian Transport in Oceanic Flows. *Annual Review of Fluid Mechanics*, 37(1): 295–328, 2005. doi: 10.1146/annurev.fluid.37.061903.175815. URL https://doi.org/10.1146/annurev.fluid.37.061903.175815. tex.eprint: https://doi.org/10.1146/annurev.fluid.37.061903.175815.